AN ABSTRACT OF THE DISSERTATION OF

Paul F. Newhouse for the degree of Doctor of Philosophy in Chemistry presented on September 26, 2008.

Title: Growth and Characterization of Wide–Gap Semiconducting Oxide and Chalcogenide Thin Films by Pulsed Laser Deposition.

Abstract approved:_____

Janet Tate

We present our results on the preparation and characterization of oxide and chalcogenide thin films by pulsed laser deposition. Also, we discuss the method of pulsed laser deposition in terms of several key aspects including background gas pressure, laser wavelength, and particulate generation. Polycrystalline films of In_2O_3:W exhibiting electron mobility > 110 cm^2/Vs at room temperature have been prepared on vitreous SiO_2 substrates at ~450 °C. For the chalcogenides, we present the facile preparation of *c*-axis aligned BiCuOSe thin films *in-situ* which exhibit a hole mobility up to 4 cm^2/Vs. Also, we describe the preparation of wide–gap (E_g >2.3 eV) Cu_3TaCh_4 (Ch = S, Se) p-type thin films, consisting of pulsed laser deposition of ceramic targets followed by *ex-situ* annealing in chalcogenide vapor. The films show strong [100]-directed growth on vitreous and crystalline substrates, with a hole mobility of 0.8 cm^2/Vs, hole concentration of 2.86 x 10^{20} cm^{-3}, and resistivity of 27 mOhm cm following direct heating in air. Finally, a description of the preparation of the p-type oxide $BaBiO_3$:K is presented in which both polycrystalline and (00*l*)-oriented films were grown.

Growth and Characterization of Wide–Gap Semiconducting Oxide and Chalcogenide Thin Films by Pulsed Laser Deposition

by
Paul F. Newhouse

A DISSERTATION

submitted to

Oregon State University

in partial fulfillment of
the requirements for the
degree of

Doctor of Philosophy

Presented September 26, 2008
Commencement June 2009

Doctor of Philosophy dissertation of Paul F. Newhouse
presented on September 26, 2008.

APPROVED:

Major Professor, representing Chemistry

Chair of the Department of Chemistry

Dean of the Graduate School

I understand that my dissertation will become part of the permanent collection of Oregon State University libraries. My signature below authorizes release of my dissertation to any reader upon request.

Paul F. Newhouse, Author

ACKNOWLEDGMENTS

It is with the utmost gratitude and appreciation that I acknowledge my research advisor, Professor Janet Tate, for many years of training, guidance, patience, and friendship. Janet never presumes, and is always guided by the evidence. She's been a model for integrity and high quality science, and combines these traits with an advisement style of engagement, respect, openness, and affability. It has been my distinct privilege to work with Janet these past years.

I gratefully acknowledge the many contributions of Ted Hinke, the best machinist I know, MVP of physical science research at Oregon State, and master of the "slick solution". Discussing ideas is easy and enjoyable with Ted, and the finished product is always of the highest craftsmanship, down to the burs.

Over the years I've been fortunate to work with many members of the Tate Lab, including Hiroshi Yanagi, Robert Kykyneshi, Matt Price, James Osborne, Ben Nielsen, Dara Easley, Levi Kilcher, Tim Murrell, "Mr. Dave" Mack, Alden Jurling, Andriy Zakutayev, Annette Richard, and Josh Russell. They've all been my teacher at one point or another and I thank you all.

With pleasure I also acknowledge many past and present members of the Keszler Group including Pete Hersh, Jason Stowers, Cheol-Hee Park, Steve Meyers, Jeremy Anderson, Heather "Swings" Platt, Kai Jiang, Joa-Young Jeong, Chris Knutson, and Sharon Betterton for their help and support. It has been my privilege to work closely with many of you, and being appointed (self appointed, nonetheless) with the title of honorary Keszler group member has been a special touch. Thanks also to David McIntyre for many discussions and assistance with optics, Hiroshi

Mizoguchi, Peter Nyholm and Hewlett-Packard, Joe Magner, David Hong, and Brady Gibbons.

I wish also to acknowledge the Departments of Chemistry and Physics, in particular Joey Carson, Linda Adams, Verna Paullin-Babcock, and Paula Rhodaback, who've all been crucial in facilitating my many on goings in Weniger and Gilbert.

I gratefully acknowledge the NSF IGERT program (DGE 0549503) which has provided generous funding and opportunity for development and collaboration in my last two years. A special thanks also to Chemistry Chair Kevin Gable, who worked closely with me in my efforts to present my research to my professional society in Europe, something I now consider as a defining moment in my professional development as a scientist. Thanks also to my committee members Joseph Nibler, Doug Keszler, John Wager, and especially Kerry McPhail and Bill Warren, who both took up the reins in service when called upon.

I've been fortunate to have many remarkable friends over the years who have helped make my life here one of joy and happiness—Brent, Pam, Jason, Avie, Pete, Kelly, Bo, Kristin, and Eva thank you for your support, companionship, laughter, and epic bike rides. And to my fantastic sisters, who never stopped cheering me on.

I dedicate this Dissertation to my parents, Ric and Mary Newhouse, who helped teach me in the most important ways.

Each heartbeat creates a miracle...

TABLE OF CONTENTS

Page

TABLE OF CONTENTS (Continued)

Page

TABLE OF CONTENTS (Continued)

Page

TABLE OF CONTENTS (Continued)

Page

LIST OF FIGURES

LIST OF FIGURES (Continued)

LIST OF FIGURES (Continued)

LIST OF TABLES

LIST OF APPENDIX FIGURES

CHAPTER 1

Introduction

In this dissertation we present our findings on thin films of several inorganic compounds prepared by pulsed laser deposition as part of the overall research theme, materials for transparent electronics. Our goal is to grow and characterize thin films of materials which exhibit high transmittance of light with wavelengths spanning 400–2500 nm and, concurrent with the property of high transmission, films of these materials (or the doped material) should exhibit the property of electrical conductivity of order 1 S/cm or more. We can thus specify the theme of this research as the development of n-type and p-type transparent semiconductors using the thin film growth method of pulsed laser deposition (the topic of chapter 2). There are many notable examples of transparent semiconductors: Sn-doped In_2O_3 (ITO), Al-doped ZnO, F-doped SnO_2, and $CuAlO_2$ (1-3). These materials form a sort of "hall of fame" of transparent conducting oxides, with the first three n-type materials having a long tradition of scientific interest and industrial applications and the last material forming a new paradigm (now just over a decade old) for p-type transparent conductors. These materials may find application anywhere a transparent electrode is required, such as a top contact in a photovoltaic cell, source and drain contacts to a transparent thin film transistor, and numerous display applications. As a result these materials are in quite large demand, especially for solar and display technologies, and have a significant economic impact. However, even though many of the long-standing archetypical n-type materials have fulfilled their purpose in many applications, new research aims to improve upon their properties, and, perhaps most importantly, develop complementary p-type materials with similar conduction properties. As it stands however, the conductivity of present-day p-type conductors like $CuAlO_2$,

LaCuOSe:Mg, and BaCuTeF are some 1-3 orders of magnitude lower than the n-type materials (1, 4, 5). As a result, the performance of transparent complementary devices are limited by the p-type layer. Nonetheless, transparent p-n junctions have been prepared (6). In the p-type oxides the carrier mobility is often very small (~0.1-1 cm^2/Vs) which is attributed to the high electronegativity of oxygen attracting positive holes. This has lead to the idea of using less electronegative anions like S, Se, and Te which would be less inclined to trap holes. We explore several chalcogenide containing compounds in chapters 4 and 5.

In chapter 2, we present a summary of the pulsed laser deposition thin film growth technique. This method was used to prepare all of the samples for this research. The key concepts, advantages, and limitations are discussed.

In chapter 3, the results of our work on In_2O_3:W are presented. We have found that this material exhibits significantly enhanced carrier mobility compared to In_2O_3:Sn and as a result transmits infrared light more effectively. Additionally, we summarize the calculated mechanism leading to the highly mobile carriers. Chapter 4 highlights our results on thin film BiCuOSe. This material is not transparent in the visible range (although it does show infrared transparency) but was of interest to our group because it is closely related to BaCuSF and LaCuOSe transparent conductors, being of the same crystal structure. The findings include a facile *in-situ* thin film preparation and a discussion of the electronic structure of BiCuOSe compared to LaCuOSe transparent conductor. Our results on Cu_3TaQ_4 (Q = S, Se, Te) thin films are presented in Chapter 5. Notably, the work here is the first ever reported thin film preparation of these compounds despite a long history of powder and crystal preparation. We discuss these

materials as possible transparent conductors and present some their favorable optoelectronic properties including a cubic (isotropic) crystal structure, p-type conductivity, wide band gap energy >2.3 eV, and intense visible photoluminescence. Chapter 6 is the final material development chapter in which we discuss our results on $BaBiO_3$. Our interest on this system began from reports on the valence band electronic structure which indicated that $BaBiO_3$ might have a high mobility hole conduction path. In the films this was found not to be the case as the hole mobility could not be measured due to the high resistivity of the films. However, this chapter does report our work on the preparation of high quality films and their associated properties.

In the appendix, we highlight our work on the design, implementation, and development of the pulsed laser deposition technique in the Tate Laboratory at Oregon State University. Many components used with the systems had to be designed and fabricated including shadow masks, laser beam apertures, substrate and target mounting systems, and scattered light safety enclosures. We also describe both systems in detail and discuss their functionality.

References

(1) Kawazoe, H.; Yasukawa, M.; Hyodo, H.; Kurita, M.; Yanagi, H.; Hosono, H. *Nature*. **1997**, *389*, 939.

(2) Hamberg, I.; Granqvist, C. G. *J. Appl. Phys.* **1986**, *60*, R123.

(3) Minami, T. *Thin Solid Films*. **2008**, *516*, 5822.

(4) Kykyneshi, R.; McIntyre, D.; Tate, J.; Park, C.; Keszler, D. *Solid State Sci*. **2008**, *10*, 921.

(5) Hiramatsu, H.; Ueda, K.; Ohta, H.; Hirano, M.; Kikuchi, M.; Yanagi, H.; Kamiya, T.; Hosono, H. *Appl. Phys. Lett.* **2007**, *91*, 012104.

(6) Hosono, H.; Ohta, H.; Hayashi, K.; Orita, M.; Hirano, M. *J. Cryst. Growth*. **2002**, *237-239*, 496.

CHAPTER 2

Summary of Pulsed Laser Deposition Thin Film Preparation Method

P. F. Newhouse[a] and J. Tate[a,b]

[a]Department of Chemistry, Oregon State University, 153 Gilbert Hall, Corvallis, Oregon USA 97331-4003

[b]Department of Physics, Oregon State University, 301 Weniger Hall, Corvallis, Oregon USA 97331-6507

Abstract

A summary of the key aspects the pulsed laser deposition (PLD) thin film growth technique are discussed. The merit of PLD lies in its ability to faithfully transfer the target stoichiometry to the film, provide energetic ablated particles with high adatom mobility, simplicity and flexibility of implementation, and versatility for materials exploration. Its disadvantages include the generation of micron-sized particles and a non-uniform thickness distribution over large area. We discuss some of the key PLD processing parameters including the role of a background deposition gas, laser wavelength, and particulate generation. PLD is a valuable research tool capable of growing high quality films with complex structure and chemical makeup.

Introduction

In this chapter, we discuss many of the basic concepts of PLD which will be relevant to subsequent chapters of this dissertation. In fact, in all succeeding chapters PLD was used to prepare the samples for this research. Below we give a brief history of the method, describe its key parameters, and discuss its advantages and disadvantages. As a supplement to this chapter, in Appendix A we describe the OSU PLD facilities and our role in their design, implementation, and development. In particular we show the results of hardware development and post-installation improvements necessary for film deposition and system reliability, including shadow masks, target holders, beam apertures, and others.

Background

The success of pulsed laser deposition as a thin film growth technique was demonstrated during the 1980s with the growth of the oxide superconductor $YBa_2Cu_3O_{7-\delta}$ (YBCO) where it was found that PLD was the only thin film growth method which accurately reproduced the target stoichiometry in the film (1). In YBCO, the superconducting transition temperature T_c and the critical current density J_c depend strongly on the relative stoichiometry of the films. Deviations from the proper film chemistry result in samples with reduced and broadened T_c and lower J_c. With PLD, high quality films of YBCO with sharp transition temperatures could be prepared (1). With other methods like sputtering and thermal evaporation such results could not be obtained due to the variable stoichiometry of the films caused by differing sputter and evaporation rates of the individual elements. On the other hand,

PLD has excelled at congruent evaporation of complex materials of widely varying evaporation rates. In the years following, PLD established itself as a method for the growth of chemically and structurally complex materials with high crystal quality. In the following sections, we discuss some of the key aspects of this technique.

Pulsed Laser Deposition

A schematic of the PLD process is shown in Fig. 1. A laser beam of wavelength λ and pulse width τ is directed into a vacuum chamber and focused onto the target surface. For sufficiently high beam energies, a plasma of target material is ejected from the surface and deposited onto the substrate opposite the target. If the laser beam energy is too low, below the threshold for ablation, the laser radiation will serve only to heat the target and cause thermal evaporation. The substrate and target are often rotated to enhance deposition and ablation uniformity, and a background gas may be used to enhance gas phase chemistry or thermalize the high energies of ablated species. Thus PLD is conceptually quite simple but affords many key advantages including stoichiometric cationic transfer of the target material, highly energetic ablated species with high adatom mobility (kinetic energies up to hundreds of eV), and sub-monolayer growth control (1, 2). Additionally, widely versatile material explorations are possible with PLD since almost any material can be ablated with sufficiently high power densities now easily achievable with nanosecond UV lasers. Also, since the power source is totally decoupled from the vacuum chamber, one laser may be shared among multiple chambers, providing cost effectiveness. Some of the

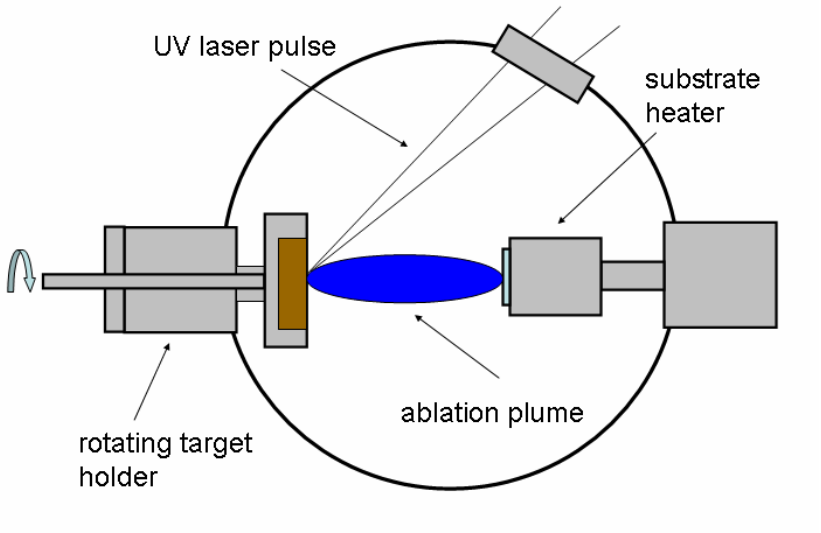

Fig. 1 Simple schematic of the PLD process. A UV laser pulse traverses a UV-grade silica entrance port and is focused onto a rotating target surface. An ablation plume of energetic species is created and collected onto a heated substrate surface some distance away, typically 1-5 cm. The decoupling of power source and vacuum chamber affords flexibility and simplicity.

drawbacks include a highly forward-directed plume with narrow angular distribution of ablated species and the generation of micron-sized particulates on the film surface.

Background Gas Pressure.

During PLD, a large dynamic range of background gas pressure ranging from UHV to 1 torr may be introduced into the chamber having a number of effects on the film properties and deposition process. Relative to deposition in UHV, the gas will scatter, attenuate, and thermalize the energy of ablated species, thus altering key aspects of film growth including deposition rate, plume spatial distribution, and film morphology and microstructure (1). The role of the gas may be to enhance gas phase

chemistry—for example, deposition of YBCO in an oxygen ambient promotes the formation of YO in the gas phase, facilitating O transport into the growing film. This is important since fully oxygenated films are desired for the highest T_c. Naturally, the use of O_2 is a common background gas used during PLD of oxides. Oxygen is often the most volatile component of the material being deposited and may be lost in the hot plume, where plasma temperatures in the range of 5000-15000 K have been estimated from optical emission spectroscopy (1). An analogous situation would be the use of H_2S gas for the deposition of ZnS. In other cases, the role of the deposition gas is a reactive element, as in the case of the deposition of metal oxide films from pure metal targets. In such cases, ambient oxygen is the sole source of the film anions. The reactive mode of PLD can be quite efficient, with high reactive cross sections for metal ions in oxygen gas (2). Additionally, if purity is a concern, metals are often available in ultra high purity. Furthermore, the reactive mode is the preferred choice for PLD of very wide gap materials like MgO, which are difficult to prepare from the ceramic due to it's low optical absorbance in most of the UV. In vacuum, the energy of ablated particles can range from 1-100 eV. A background gas pressure can drastically reduce these energies to well below 1 eV (1, 2). This energy thermalization can be beneficial, since the very high energy particles ablated in vacuum can cause defects and re-sputtering in the growing film (3).

Laser Wavelength

Ideally, the target material has high optical absorption at the laser wavelength, leading to reduced penetration depths and decreased ablation thresholds. In YBCO

thin films, the choice of laser wavelength was shown to have a drastic impact on the film morphology, with the lowest particle density films being prepared from the UV output from a Nd:YAG compared to films prepared from the visible and IR wavelengths. This has been ascribed to much higher UV absorption, leading to reduced penetration depths and smaller radiation-induced surface modifications, which are exfoliated from the target during plume generation. To evaluate the effects of laser power, let us consider a beam of electromagnetic radiation with peak power □ (in W/cm^2) absorbed into a material with refractive index *n*. The corresponding electric field will be given by

$$E = \left(\frac{2\Phi}{c\varepsilon_0 n} \right)^{1/2} \qquad [1]$$

where *c* is the velocity of light and ε_0 the permittivity of vacuum. For a material with $n = 1.5$ and a laser pulse with $\Phi = 5 \times 10^8$ W/cm^2 the electric field generated inside the material would be 5×10^5 V/cm, which is high enough to cause dielectric breakdown in most materials (1). Indeed, PLD experienced an era of significant growth with the advent of reliable Q-switched Nd:YAG lasers which offered high peak power, nanosecond pulse widths, and reliable UV output from 2^{nd} and 3^{rd} harmonic generation. At present, commercially available UV gas lasers are the preferred choice of researchers because they offer high power output directly into the UV. Also, many materials exhibit higher absorption coefficients in the UV region. In Table 1, some common lasers used for PLD are listed with their output wavelength, with excimer and Nd:YAG lasers being the most prevalent, although picosecond and femtosecond PLD

Table 1 Common lasers used for PLD and their output wavelength. The subscript on the Nd:YAG entries refers to their fundamental, frequency doubled, and frequency quadrupled output.

	Laser	Output Wavelength (nm)
Gas	F_2	157
	ArF	193
	KrCl	222
	KrF	248
	XeCl	308
	XeF	351
Solid State	Nd:YAG_f	1064
	Nd:YAG_2	532
	Nd:YAG_4	266

is becoming commonplace (4,5). For ceramic materials, a laser output energy of 0.5-5 J/cm^2 (= 0.2-2 x 10^8 W/cm^2 for 25 ns pulse) is usually sufficient for efficient plume generation, while for metals higher power is used, generally in the 5-15 J/cm^2 range due to their stronger cohesive forces and high thermal conductivities. In general, a laser pulse width of order nanoseconds is used, since shorter pulses help to keep the thermal diffusion length and ablated volume small (1). This favors congruent evaporation and reduced particulate generation. New research has recently been undertaken on PLD using femtosecond lasers, which offer very high peak power (5, 6).

Particle Generation

One of the key disadvantages of PLD is the generation of micron-sized particulates on the film surface. In Fig. 2, dark field and bright field optical micrographs of an as-deposited Cu_3TaS_4 film (see chapter 2) are shown, revealing a high density of 1-5 micron particles. Particles of this size can have a detrimental

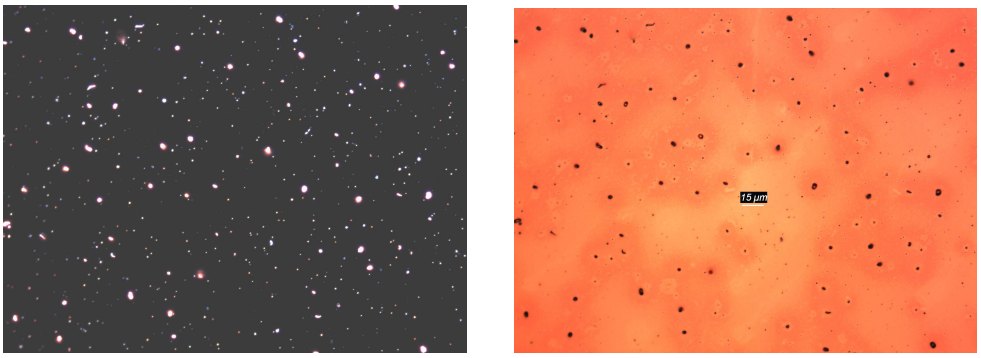

Fig. 2 Optical micrographs of as-deposited films of Cu_3TaS_4 in dark field (left) and bright field (right). Particles of ~1-5 mm are observed from in both images. The specs of light in the dark field image are due to light scattering from the particles. The scale bar is 15 microns.

effect on film properties including reductions in device mobility, defect and scattering center formation, and downgrade of optical damage threshold of optical coatings. The presence of these particles and their induced defects have been the one of the main drawbacks in widespread use of the PLD, the other begin the difficulty to prepare uniform, large area coating due to the highly forward-directed plume. Normalizing the film thickness distribution has some very clever engineering solutions, and large scale coating with PLD has been demonstrated (7). However, the particle or droplet formation is a more intrinsic problem. Several different mechanisms of the droplet formation have been proposed. Sub-surface boiling can occur if the time required to transfer laser energy into heat is shorter than that needed to evaporate a thin comparable to the skin depth. Under this condition, superheating of the subsurface occurs before the surface layer has reached the vapor phase, expelling molten droplets on the film (1). Another mechanism of particle generation originates from the surface modification of the target surface induced after repeated laser pulses. Laser induced needle-like microstructures form and can be dislodged by thermal and mechanical shock from the laser pulse. In general, high target density and smooth surfaces are desired to reduce the droplet density. If the absorption coefficient of the material is large enough, a single crystal target may be used (8) and usually imparts a large decrease in the ejected particle density. Engineering solutions to the particle problem include mechanical high pass velocity filters which work on the premise that the plume atomic species travel much faster than the heavy particles (9). The faster, lighter species are passed to the substrate and the much heavier particulates are deflected. This method can be effective but reduces the film deposition rate

considerably. Other approaches include the use of a second UV laser beam which intersects the plume. The second beam causes further fragmentation of the particulates in the plume (1).

Conclusion

In summary, we have presented the key concepts of PLD which include stoichiometric cationic transfer of the target material, highly energetic ablated species with high adatom mobility, sub-monolayer growth control, and high flexibility of materials exploration. PLD excels at growing high quality films of structurally and chemically complex materials, proving to be an invaluable research tool. The key parameters of PLD growth of thin films—background gas pressure, laser wavelength, and particulate generation have been discussed. In particular, the ambient gas pressure thermalizes the plume energy and enhances gas phase chemistry, high optical absorption at the laser wavelength is preferred, and the production of micron-sized particulates is an intrinsic process during PLD, which can be mitigated by the used of high density targets and crossed-beam PLD geometries.

References

(1) Chrisey, D. B.; Hubler, G. K. *Pulsed Laser Deposition of Thin Films*; 1st ed.; Wiley-Interscience, 1994.

(2) Eason, R. *Pulsed Laser Deposition of Thin Films: Applications-Led Growth of Functional Materials*; Wiley-Interscience, 2006.

(3) Norton, D. P.; Park, C.; Budai, J. D.; Pennycook, S. J.; Prouteau, C. *Appl. Phys. Lett.* **1999**, *74*, 2134.

(4) Reilly, A.; Allmond, C.; Watson, S.; Gammon, J.; Kim, J. G. *J. Appl. Phys.* **2003**, *93*, 3098.

(5) Zhang, Y.; Russo, R. E.; Mao, S. S. *Appl. Phys. Lett.* **2005**, *87*, 133115.

(6) Garrelie, F.; Loir, A. S.; Donnet, C.; Rogemond, F.; Le Harzic, R.; Belin, M.; Audouard, E.; Laporte, P. *Surf. Coat. Technol*. **2003**, *163-164*, 306.

(7) Greer, J. A.; Tabat, M. D. *J. Vac. Sci. Technol. A.* **1995**, *13*, 1175.

(8) Li, Y.; Yao, X.; Tanabe, K. *Physica C*. **1998**, *304*, 239.

(9) Pechen, E. V.; Varlashkin, A. V.; Krasnosvobodtsev, S. I.; Brunner, B.; Renk, K. F. *Appl. Phys. Lett.* **1995**, *66*, 2292.

CHAPTER 3

High Electron Mobility W-doped In_2O_3 Thin Films by Pulsed Laser Deposition

P. F. Newhouse[a], C-H. Park[a], P. S. Nyholm[c], D. A. Keszler[a,b], and J. Tate[b,a]

[a]Department of Chemistry, Oregon State University, 153 Gilbert Hall, Corvallis, Oregon USA 97331-4003

[b]Department of Physics, Oregon State University, 301 Weniger Hall, Corvallis, Oregon USA 97331-6507

[c]Hewlett-Packard Company, 1000 NE Circle Boulevard, Corvallis, Oregon USA 97330-4239

Modified versions of this work appear as

P. F. Newhouse, C-H. Park, P. S. Nyholm, D. A. Keszler, J. Tate, *Appl. Phys. Lett.* **87** *112108* (2005).
&
P. F. Newhouse, C-H. Park, P. S. Nyholm, D. A. Keszler, J. Tate, *Mater. Res. Soc. Symp. Proc*. 905E, **Materials for Transparent Electronics**, 0905-DD01-02 (2006).

Abstract

Thin films of transparent conductor $In_{2-x}W_xO_3$ exhibiting electron mobility >110 cm^2/Vs, carrier density of 1-3 x 10^{20} cm^{-3}, and resistivity as low as 3.37 x 10^{-4} Ohm cm at room temperature have been prepared on vitreous SiO_2 substrates using pulsed laser deposition of ceramic In_2O_3:WO_3 targets. The highest mobility and conductivity was measured from films with a W concentration of $x \sim 0.03$ (= 1.5 cation atomic %). Films deposited onto SiO_2 substrates are polycrystalline, while films prepared on single crystal YSZ substrates exhibit [100]-directed growth. $In_{2-x}W_xO_3$ films show high visible transmittance of ~80% due to large band gap energies of 3.8-3.9 eV. Slight widening of the band gap with increasing free carrier density (Moss-Burstein effect) was observed, from which the electron effective mass was determined to be $0.3m_e$. Due to low free carrier density and high mobility $In_{2-x}W_xO_3$ films show extended near infrared transmission compared to In_2O_3:Sn films. Low temperature Hall effect measurements on high mobility $In_{2-x}W_xO_3$ films indicate that the electron mobility is constrained by phonon scattering and ionized impurity scattering. The mechanism for the observed high mobility is explained on the basis of transition metal magnetic exchange interactions, which impart spin distinguishability to the W_{In} charge generating scattering centers, resulting in an effective two-fold reduction in the their concentration. XPS measurements reveal that W in high mobility IWO films exists in as W^{6+} or W^{5+}.

Introduction

Indium oxide-based transparent conductors, especially In_2O_3:Sn (ITO), have been in use for half a century due to their key attributes of simultaneous high electrical conductivity and visible transparency, low crystallization temperature, isotropic cubic structure, high manufacturing amenability, air insensitivity, and chemical and mechanical robustness (1). Additionally, In_2O_3 has shown the ability to accommodate many different cationic dopants aside from Sn including Ge, Si, and Zn (2, 3). Each of these dopants increased the electrical conductivity (σ) while maintaining the optical transparency, with no distinct advantage for a particular dopant compared to Sn. Recently, however, a breakthrough in In_2O_3-based transparent conductors has been discovered in which the incorporation of Mo, Zr, Ti, and W refractory metal dopants imparts a 3-4 fold increase in the electron mobility (μ) compared to In_2O_3:Sn (4-8). In particular, evaporated thin films of In_2O_3:Mo (IMO) on glass substrates exhibit $\mu = 130$ cm^2/Vs with $\sigma = 5900$ S/cm, while sputtered and laser ablated IMO films have demonstrated best-case mobilities of 83 cm^2/Vs on glass and >95 cm^2/Vs on yttria-stabilized zirconia (YSZ), respectively (4, 6, 9). These mobility values are factors of two to three greater than those measured in polycrystalline ITO films prepared by PLD ($\rho = 3.60 \times 10^{-4}$ Ohm cm, $n = 4.5 \times 10^{20}$ cm^{-3}, $\mu = 38$ cm^2/Vs) and single crystal ITO thin films ($\rho = 7.7 \times 10^{-5}$ Ohm cm, $n = 1.9 \times 10^{21}$ cm^{-3}, $\mu = 42$ cm^2/Vs.) (10, 11). Undoped, pulsed laser deposited In_2O_3 films exhibit a mobility of 30-35 cm^2/Vs (7). The development of a high mobility transparent conducting oxide (TCO) is significant because increasing the carrier mobility, rather than simply increasing the carrier

density, is the best route to optimizing the electrical conductivity. In this manner, transparency losses from free carrier absorption in the near-infrared (NIR) are minimized (12). The improved NIR optical properties which result from the high mobility carriers and lower carrier density may be beneficial for TCO top contacts in solar cells, which would transmit more solar irradiance to the absorber layer.

In this chapter we present the results of transport, optical, structural and compositional measurements of $In_{2-x}W_xO_3$ (IWO) thin films prepared by PLD from a series of low density and high density targets. We show that W is an effective dopant for realizing a high mobility TCO. Significantly, these high mobilities are measured from polycrystalline films prepared at moderate temperatures on amorphous substrates. Initial work on the IWO system was conducted with low density PLD targets prepared in-house, and following our auspicious mobility results higher density targets were obtained which permitted the use of much higher laser power. The use of high laser power and high density targets allowed films to be prepared with predictable W concentration and smoother surface morphology. This made it possible to prepare IWO films with the optimum W concentration for high mobility. In particular, using high density targets we have prepared polycrystalline IWO thin films on glass substrates which exhibit $\mu = 112$ cm^2/Vs, $n = 1.67 \times 10^{20}$ cm^{-3}, and $\rho = 3.37 \times 10^{-4}$ Ohm cm at room temperature. Transport measurements at low temperature were also performed which reveal heightened mobilities characteristic of decreased phonon scattering and carrier concentrations which are not thermally activated down to 77 K. We also present results from quantitative elemental analysis of IWO films from which we determined the optimal W concentration for high

mobility and showed that W is evaporated incongruently from the low density targets when using low laser fluence of ~0.5 J/cm^2. In Figs. 4 and 5, we present our thin film structural characterizations using fixed incidence and θ–2θ x-ray diffraction. These measurements show that IWO films prepared on amorphous SiO_2 (a-SiO_2) exhibit statistical crystallite orientation, while films prepared on yttria-stabilized zirconia (YSZ) show (00*l*) preferential orientation. In Figs. 6 and 7, the UV–vis–NIR optical properties of IWO films are presented. The band gaps of IWO films are generally greater than 3.8 eV, which imparts high visible transparency exceeding 80%. A slight widening of the band gap with increasing carrier concentration has been ascribed to the Moss-Burstein (MB) effect (13, 14), and the electron effective mass calculated on MB framework is 0.3m_e, in good agreement with closely related systems (9). In the NIR, the combination of high mobility and low carrier density imparts IWO films with increased transmission and reduced free carrier absorption compared to a conventional mobility TCO like ITO with μ ~35 cm^2/Vs (1, 12). Also, in Fig. 8, high resolution x-ray photoelectron (XPS) measurements of high mobility IWO films are presented which show that W in high mobility films exist in a high valent state such as W^{6+} or W^{5+} and not a lower valent state. This result provides insight into the possible carrier generating defects in IWO. Finally, a summary of the theoretical framework elucidating the mechanism for high mobility in Mo-doped In_2O_3 is presented (15). The theory applies to IWO as well (15). We shall use defect notation i.e. $W_{In}^{\bullet\bullet\bullet}$ is interpreted as W^{6+} substitution onto an In^{3+} site, which is triply positive since the valency difference is three. Each ($^{\bullet}$) denotes a single positive charge. Oxygen interstitials are denoted O_i and carry a doubly negative charge ($''$).

Experiment

Thin films of $In_{2-x}W_xO_3$ were deposited onto heated GE 124 a-SiO_2 and single crystal YSZ (001) substrates using pulsed laser ablation of ceramic In_2O_3:W pellets in a UHV chamber with a base pressure of 2 x 10^{-9} torr. For target preparation, stoichiometric proportions of In_2O_3 (99.99%, Cerac) and WO_3 (99.99 %, Cerac) were thoroughly mixed, and then pressed into 1″ diameter pellets at 4.4 tons. The W content was x_{target} = 0, 0.025, 0.0375, 0.05, 0.625, and 0.075, which corresponds to a cation atomic ratio of 0-3.75%. The pellets were sintered in air at 1500 °C for 4 h with a heating rate of 300 °C/h and a cooling rate of 500 °C/h. The sintered pellets were approximately 60% of theoretical density. The targets, polished prior to each use, were ablated in pure O_2(g) (99.997%) ambient by pulsed radiation from a Lambda Physik Compex 201 KrF excimer laser (λ = 248 nm, τ = 25 ns) operating at 10 Hz. The laser fluence (Φ) was constrained to ~0.5 J/cm^2 by the low target density as serve pitting of the target surface resulted at higher laser energies. Ambient O_2 gas pressure in the chamber during deposition was varied, and it was typically a few millitorr. The target was positioned 45 mm from the substrate, which was maintained at a constant temperature between 400 °C and 600 °C throughout the deposition. Deposition rates for the 300-500 nm thick films varied between 0.06 and 0.1 nm/pulse. Both the target and substrate were rotated during the deposition to enhance ablation and deposition uniformity, respectively. After deposition, the films cooled in the oxygen atmosphere present during deposition until they reached a temperature below about 70 °C (about 30 minutes for a substrate temperature of 400 °C). For each deposition, a custom-made inconel shadow mask was used to pattern the films into a cross shape that

facilitated subsequent transport measurements. Additional work was carried out with commercially prepared, higher density IWO targets with x_{target} = 0, 0.02, 0.05. The targets had densities of 68, 88, and 74%, respectively, and permitted the use of higher laser fluence of 2-3 J/cm^2 without target surface pitting. Similar oxygen pressure and substrate temperatures were used to prepare these series of films, but a different, lower vacuum chamber was used (base pressure = 1 x 10^{-7} torr), and films were quenched in N_2 rather than allowed to cool in the oxygen deposition ambient. Again, a-SiO_2 and YSZ (001) substrates were used. IWO films were prepared from single targets or multiple targets using IWO/In_2O_3 multilayer processing, which permitted adjustment of the film W concentration. For multilayer processing, a simple program was used to raster each target into the path of the beam for a set number of pulses to create multilayer stacks, with pulse counts and repeat units chosen on the basis of approximate deposition rates and desired film stoichiometry. Based on the thickness of the individual multilayers (<10 nm) and substrate temperatures (400-500 °C) uniform film composition was assumed. Additional multilayer films were prepared from IWO targets and a high density $In_{1.81}Sn_{0.19}O_3$ target to investigate the potential union of the high mobility properties of IWO and the efficient carrier generation and high conductivity of ITO.

Films were characterized by fixed incidence and θ–2θ x-ray diffraction (XRD), electrical conductivity, variable field Hall effect transport measurements, electron probe microanalysis (EPMA), and by UV–vis–NIR transmission and reflection. Fixed incident angle XRD spectra (Cu K_α) were measured with a Rigaku Rapid R-axis diffractometer while a Rigaku Miniflex tabletop diffractometer was used to acquire

θ–2θ XRD patterns. For measurements using the Rapid R-axis diffractometer a two-dimensional area detection screen allowed reflections from a range of 2θ and χ angles to be acquired simultaneously. Electrical conductivity and Hall mobility were measured in the van der Pauw configuration on a Lakeshore 7504 Hall measurement system at fields of 5-20 kG and 4-7 kG at room temperature and 77 K, respectively. EPMA was performed using a Cameca SX50 electron microprobe with beam energies of 10, 15, and 20 kV. Optical transmission and reflection spectra in the UV–visible range were measured using a double grating spectrometer with a Xe lamp source and a Si diode detector. NIR transmittance and reflectance spectra were acquired using a Nicolet Nic-Plan microscope accessory fitted to a Magna 750 Fourier transform infrared spectrometer. Spectra are the average of 256 Fourier transformed interferograms over 11700-2100 cm^{-1} with 4 cm^{-1} resolution. Air and a Au mirror were used for transmission and reflection background calibration. XPS photoelectron spectra were measured using a Physical Electronics Quantera scanning ESCA using monochrome Al x-rays with energy 1486.7 eV and spot diameter 200 μm. An Ar+ ion beam was used to sputter clean the sample surface prior to analysis (0.5 min at 4.4 nm/min relative to SiO_2). Chemical quantification calculations were made using established sensitivity factors (16).

Results and Discussion

Electronic Properties from Low Density Targets

Fig. 1 shows the results of room temperature (solid diamonds) and 77 K (open diamonds) Hall effect transport measurements as a function of film doping for a series of IWO films deposited from low density targets onto a-SiO_2 substrates. The films were prepared under the same deposition conditions of 1 mtorr O_2, 400 °C, and 0.5 J/cm^2). As can be seen from the figures, optimized room temperature transport properties of μ = 66 cm^2/Vs, σ = 3.08 x 10^3 S/cm, n = 2.90 x 10^{20} cm^{-3} were found when x_{film} ~0.03. Increasing the substrate temperature to 525 °C while holding other deposition parameters constant (triangle) resulted in a film with significantly improved room temperature mobility and conductivity (μ = 104 cm^2/Vs, σ = 3.34 x 10^3 S/cm, n = 2.00 x 10^{20} cm^{-3}), and the equivalent film on a YSZ (001) single crystal substrate (cross) showed μ = 112 cm^2/Vs and σ = 4.50 x 10^3 S/cm, and n = 2.51 x 10^{20} cm^{-3} representing the best-case room temperature transport results from films prepared using low density targets. These high mobility results for IWO films prepared at moderate substrate temperatures are two to three times greater than commercial grade or high quality ITO films and are comparable with earlier results from the IMO system (4, 9, 10).

Transport measurements at 77 K on all films in the diamond series showed the same general trends as the room temperature measurements (Fig. 1). The mobility and conductivity increase up to x ~ 0.03 followed by a steady decrease at higher dopant

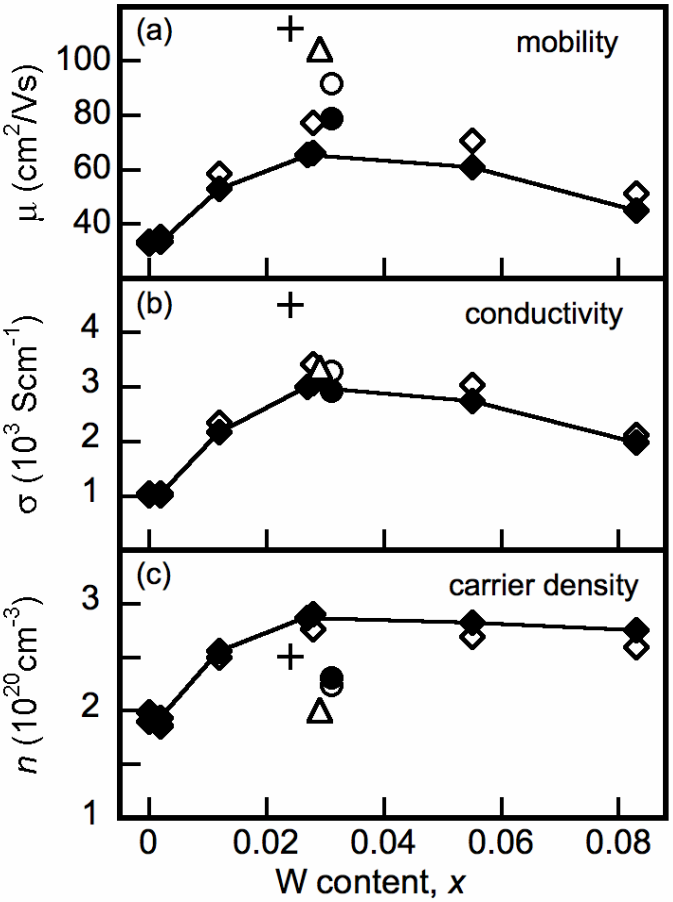

Fig. 1 Room temperature and 77 K Hall mobility (a), conductivity (b), and carrier density (c) for several IWO films prepared on fused SiO_2 and single crystal YSZ (001) substrates. The triangle and the cross refer to the best-case room temperature results for films on fused SiO_2 and YSZ, respectively. The lines are a guide to the eye. Other symbols are explained in the text

concentration. The elevated mobility at low temperature is consistent with decreased phonon scattering. However, for films of high dopant concentration, scattering by W ionized impurities is also significant as evidenced by the fall-off in mobility at both low and high temperatures when $x > 0.3$. Fig. 1 shows that the carrier density for the diamond series of films remains essentially constant when $x_{film} \geq 0.03$, following an initial increase in the carrier density when $x_{film} < 0.03$ due to increased incorporation of W into the host lattice. At low temperature the carrier density for all IWO films decreases only slightly, indicating that the carriers are not thermally activated over the temperature range probed. In principle, W^{6+} substitution on In^{3+} sites in In_2O_3 could generate as many as three electron carriers per W, viz. $W_{In}^{\bullet\bullet\bullet}$. However, this level of doping efficiency has not been observed in this or closely related systems like IMO (4, 9). For the highest carrier concentration IWO films with x_{film} ~0.03, the doping efficiency is 0.75-1 electron/W indicating that the $W_{In}^{\bullet\bullet\bullet}$ is probably charge compensated by interstitial oxygen, O_i, forming a singly charged complex, $[W_{In}^{\bullet\bullet\bullet} O_i'']^{\bullet}$. Indeed, LAPW calculations show that the O_i compensated species have very favorable formation energies (15) and the experimental results clearly indicate that the mobility is strongly dependent on the oxygen partial pressure during deposition. In ultra-high quality ITO films, each substitution of In^{3+} ion by Sn^{4+} ion accounts for one electronic carrier, leading to a doping efficiency of 100% or greater (17).

The effect of oxygen pressure on IWO films was briefly investigated. Under otherwise identical preparation conditions as the diamond series, depositions at 4 mtorr O_2 (solid circle) and 7 mtorr O_2 (not plotted) resulted in films exhibiting

improved room temperature mobilities (79 and 78 cm^2/Vs, respectively) beyond those measured in the series of films prepared under 1 mtorr O_2. The film deposited under 4 mtorr O_2 showed μ = 92 cm^2/Vs when cooled to 77 K (open circle). These mobilities are significantly higher than the values near 33 cm^2/Vs for undoped In_2O_3 films deposited on glass under 1 mtorr O_2. The development of high mobility TCO materials like IWO could be significant for applications which require increased IR transparency, since the magnitude of the IR absorbance is reduced due to high carrier mobility, and the intrinsically low carrier concentration pushes the onset of IR reflectance to longer wavelength (12).

Electronic Properties from High Density Targets

We next present the results of films deposited from higher-density targets, ranging in density from 68-88%. These targets did not pit under repetitive laser radiation and allowed the laser fluence to be increased to 2-3 J/cm^2 where congruent transfer from target to film occurs. For these films, we rely solely on target composition to determine the film W concentration. Fig. 2 shows transport results as a function of oxygen pressure during deposition for the (non-optimal) dopant concentration x = 0.02 (open circles). The mobility of an IWO film deposited at 465 °C on a-SiO_2 is 89 cm^2/Vs at the optimal pressure of 4 mtorr, and remains above 75 cm^2/Vs at higher oxygen pressures. A film with optimal dopant concentration of x ~0.033 deposited under the same conditions on a-SiO_2 (solid diamond) exhibits μ = 112 cm^2/Vs, which is equal to our previous high value on YSZ using low density

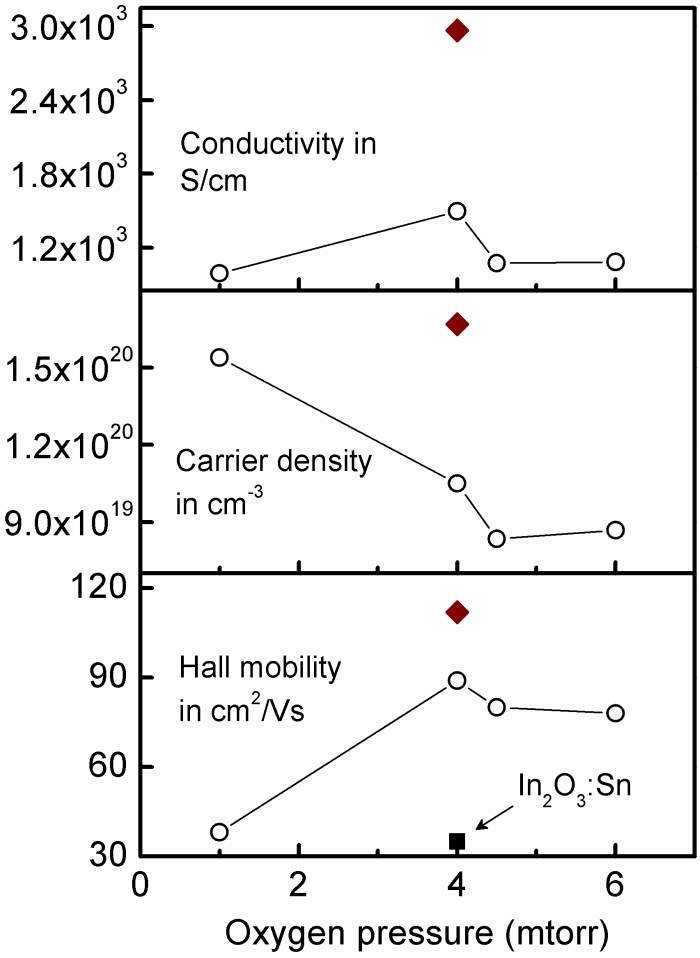

Fig. 2 Transport properties of IWO films prepared from $x = 0.02$ targets as a function of deposition oxygen pressure (open circles). The mobility has a strong oxygen pressure dependence, with the highest mobility films prepared at 4 mtorr. The filled diamond represents an IWO/In_2O_3 multilayer film deposited on a-SiO_2 with $x \sim 0.33$, exhibiting the highest mobility measured in this work.

targets. The carrier density of this film is 1.67 x 10^{20} cm^{-3} and the resistivity is 3.37 x 10^{-4} Ohm cm (= 2966 S/cm). A mobility of this magnitude on a vitreous substrate is a significant result. To prepare the film with optimal W concentration, 1:1 multilayer processing from high density $x = 0$ and $x = 0.05$ targets was used to create an IWO film with a W content of $x_{average}$ ~0.025. However, XPS chemical analysis revealed that this film has x ~0.033, indicating that the ablation rates of the targets differ slightly.

W, Sn co-doped In_2O_3 Thin Films

Although IWO and other refractory-metal-doped indium oxides yield films with higher mobility carrier than ITO, the conductivity of ITO remains consistently higher because of the larger carrier density. We attempted to co-dope In_2O_3 with W and Sn by depositing multilayers of $In_{1.98}W_{0.02}O_3$ and $In_{1.81}Sn_{0.19}O_3$. In the most optimistic scenario, some form of modulation doping might have been achieved where ITO efficiently produced large numbers of carriers that were transported in the high-mobility IWO layers. Fig. 3 shows the results of a series of depositions under identical conditions where the relative amount of IWO and ITO was steadily varied. The results indicate that introduction of ITO into IWO quickly reduced the mobility to levels approaching that of ITO, and while the carrier concentration increased, there was no co-doped film that produced a conductivity higher than that of pure ITO. It is likely that the deposition conditions produced a mixing of the W and Sn dopants, which served mainly to increase the scattering.

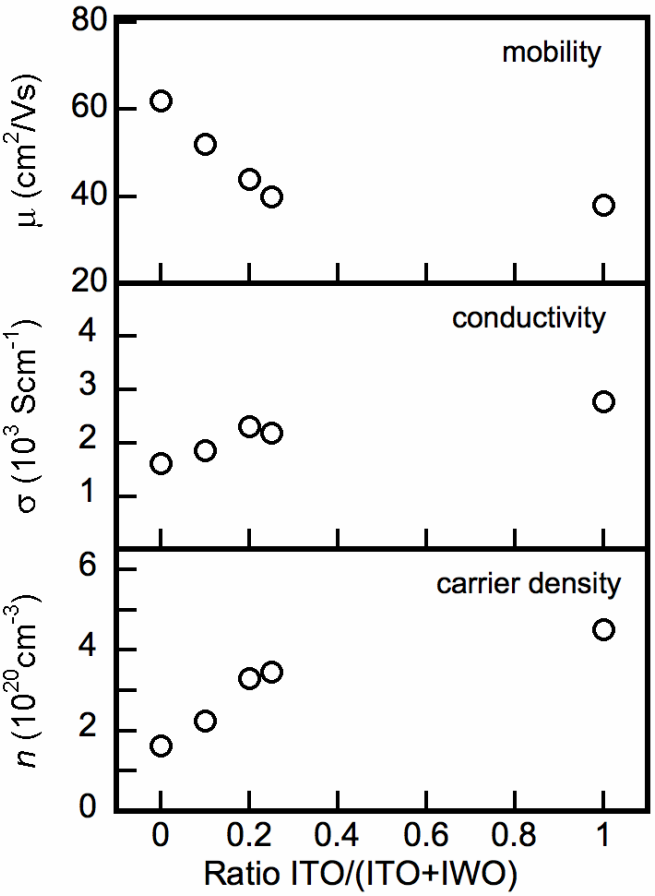

Fig. 3 Transport properties of In_2O_3 films co-doped with W and Sn, prepared by multilayer deposition of IWO and ITO high density targets.

W Concentration in IWO Thin Films

Determination of the W content of the IWO films is of crucial importance. EPMA provides a reliable quantitative measure of film stoichiometry provided careful attention is paid to eliminating substrate interference and to the variation of excitation volume with incident beam energy. In this study, EPMA was performed on various films of different W doping level (i.e. x in $In_{2-x}W_xO_3$). Compositional analyses were obtained on a Cameca SX50 electron microprobe equipped with four tunable wavelength dispersive spectrometers. The electron beam energies were 15, 20, and 25 kV, and data were acquired at five different film locations (typically several microns apart) for each beam energy. Background corrections for each element were carefully applied to avoid interference from any overlapping or satellite lines. The detection limit for W was at worst 0.15 wt %, which corresponds to $x = 0.002$. The averaged *k*-ratio data corrected for dead time, background, and drift were refined in Stratagem a thin film composition software program that performs a correction to account for sample geometry and substrate.

The EPMA results are summarized in Table 1. The W concentration of the film deviates significantly from that of the target, especially for low doping levels. The high mobility IWO films prepared from targets of W doping level $x_{target} = 0.05$ using 0.5 J/cm^2 have a dopant concentration of $x_{film} = 0.028$. This result was reproducible for many different films prepared from the same target, irrespective of substrate temperature or background gas pressure. Films prepared from targets with $x_{target} = 0.025$ using 0.5 J/cm^2 showed only trace amounts of W by EPMA and their

Table 1 W content in IWO thin films and the (low density, in-house) target from which the film was deposited. At 0.5 J/cm^2, W is evaporated incongruently from the target, while at 2 J/cm^2 measurable W is transferred to the film (last column) and the film showed high mobility. By contrast, the film prepared from the $x = 0.025$ target at 0.5 J/cm^2 had mobility characteristic of undoped In_2O_3 and W content in the noise range of the spectrometer (italics). The target and film for which the mobility is highest are highlighted.

Φ J/cm^2	0.5	0.5	0.5	0.5	2
x_{target}	*0.025*	0.0375	**0.05**	0.0625	0.025
x_{film}	*0.001*	0.012	**0.028**	0.055	0.016

mobilities were also characteristic of undoped In_2O_3, that is, μ ~30 cm^2/Vs. However, by increasing the incident laser fluence to 2 J/cm^2, high mobility films could be prepared from $x = 0.025$ low density targets. This indicated that some amount of W was transferred to the film in the ablation plume at this higher fluence, and EPMA showed that the W content of these high mobility films was measurable at $x_{film} = 0.016$. Only very thin films could be prepared using $2J/cm^2$, as the target surface degraded quickly from severe surface pitting. Overall, x_{film} determination by EPMA provided a more consistent interpretation of the variation of transport properties with dopant concentration. The observed incongruent transfer of W from the In_2O_3:W targets resulted from the use of low laser energy density, and also to low target density and high porosity, which can further dilute the incident laser fluence by increasing the effective surface area of the irradiated region (18). Of course, the extreme refractory nature of W exacerbated this issue. Our subsequent use of high density IWO targets mitigated these problems.

Structural Characterization of IWO films

Figure 4 shows the XRD patterns for IWO films deposited on a-SiO_2 and YSZ (001) at substrate temperatures of 400 °C and 525 °C, respectively. A calculated XRD pattern for pure In_2O_3 is shown in the lower pane. The film on a-SiO_2 is polycrystalline and indexed completely to In_2O_3, while the film on YSZ exhibits high intensity YSZ (002) and IWO (004) peaks at 35.0° and 35.5° 2θ, respectively. Small peaks at higher angle are ascribed to the substrate (marked by an asterisk) or film

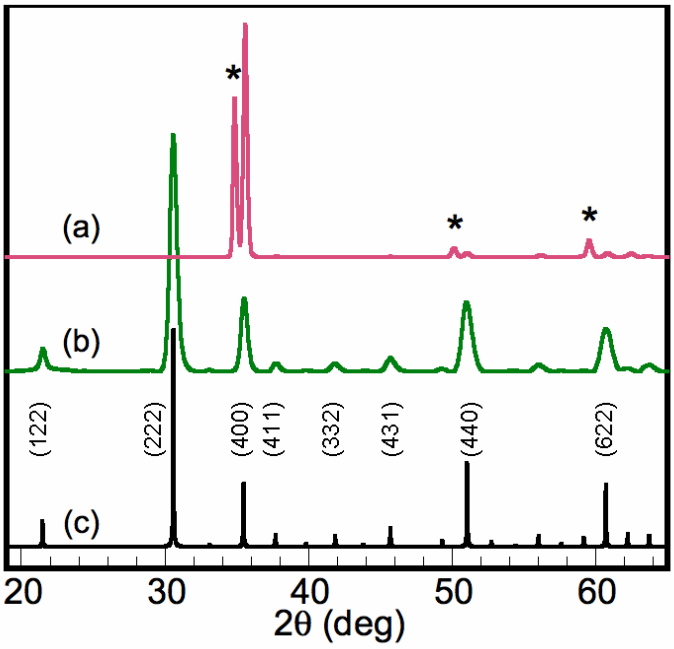

Fig. 4 XRD patterns for textured (a) and polycrystalline (b) IWO films on fused SiO_2 and YSZ (001). A calculated XRD pattern for undoped In_2O_3 is shown in (c).

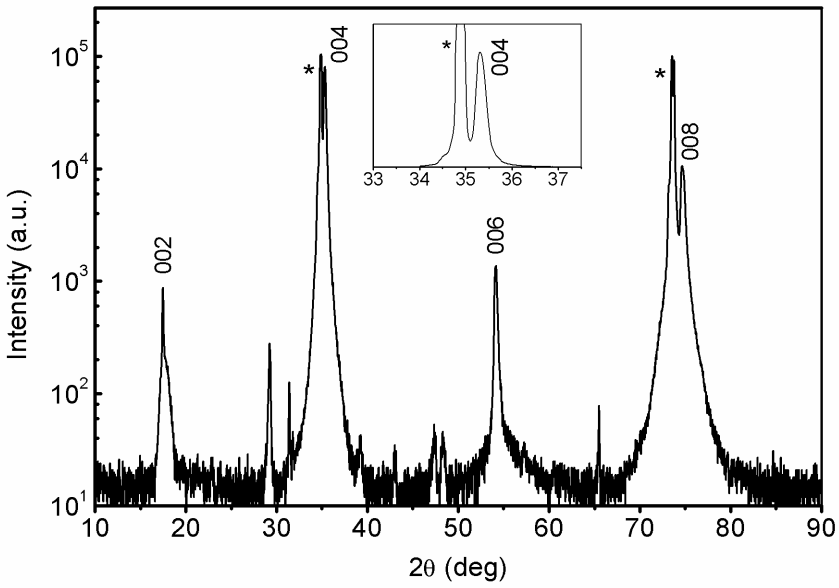

Fig. 5 θ–2θ XRD pattern of an IWO film on a YSZ (001) substrate on a log scale. The film exhibits (00*l*) preferential orientation, as evidenced by the enhancement of peaks of type (00*l*) and suppression of most polycrystalline peaks. The inset shows a zoomed-in view of the film (004) peak on a liner scale. Asterisks denote substrate peaks.

polycrystalline peaks. In general, IWO films prepared on a-SiO_2 exhibit polycrystalline orientation while those on YSZ (001) substrates exhibit (00*l*) preferential orientation with a few polycrystalline peaks. To better observe the (00*l*) preferential orientation from IWO films on YSZ, θ–2θ XRD measurements were performed and plotted on a log scale (Fig. 5). Peaks of type (00*l*) are enhanced relative to the powder, while most peaks of type (*hkl*) are suppressed, indicating that film growth along [100] is preferred. The inset shows a zoomed-in view of the (004) peak, plotted on a linear scale. Asterisks mark the substrate reflections. Unlabeled peaks are correspond to second phase impurities or polycrystalline peaks.

Optical Properties

Shown in Fig. 6 are the UV–visible transmission *T* and reflection *R* spectra for a typical IWO film of thickness 200 nm on a 0.5 mm thick a-SiO_2 substrate. The average raw transparency is about 80%, a value representative of most films produced in this work. The reflection-corrected transmission, $T/(1-R) \approx e^{-\alpha d}$, is also plotted where α is the absorption coefficient and *d* is the film thickness. Thin film interference fringes in the reflectance spectrum were used to extract the film thickness and refractive index by fitting a calculated *R* spectrum to the experimentally obtained spectrum. Calculated thickness values agree within 5% with values obtained via mechanical profilometry, and the refractive index (n = 1.99 at 500 nm) is close to published values for ITO thin films (19). Direct bandgap information was obtained

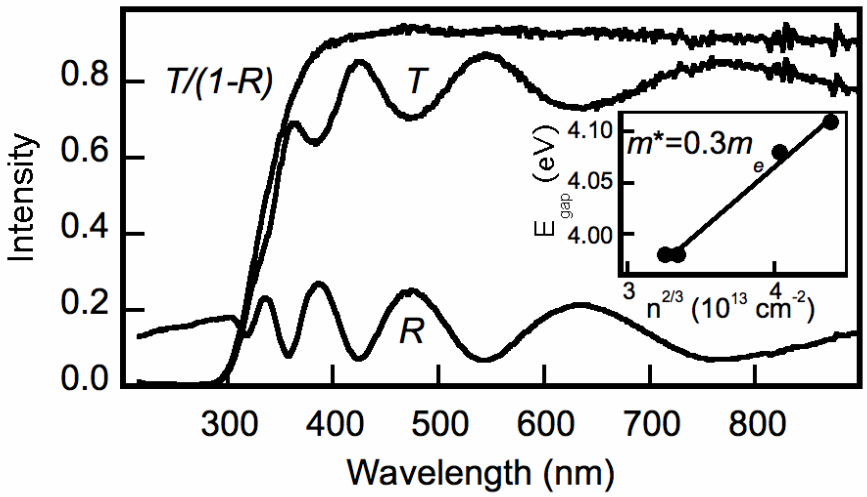

Fig. 6 The optical transmission *T*, reflection *R*, and reflection-corrected transmission *T/(1-R)* for a typical IWO film of thickness ~0.3 μm on a fused SiO_2 substrate. The inset shows the band gap energy of several IWO films vs. $n^{2/3}$ and a fit to Equation 1.

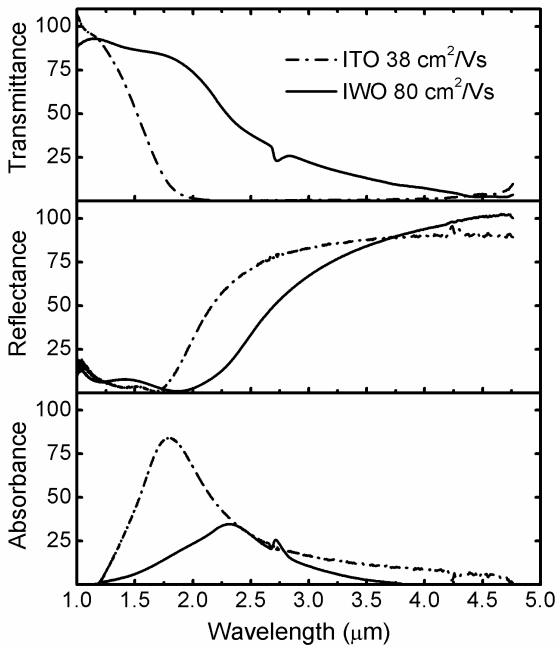

Fig. 7 The NIR optical properties for thin films of high mobility (80 cm^2/Vs) IWO (solid line) and conventional mobility (38 cm^2/Vs) ITO (dash-dot line). The high mobility and low carrier density properties of IWO result in heightened IR transmittance and reduce absorbance relative to ITO.

from plots of $(\alpha E)^2$ vs. E, from which it was found that E_g varied between about 3.80 eV and 3.91 eV for most films.

Widening of the fundamental band gap in heavily doped semiconductors due to displacement of the Fermi level into the conduction band (known as the Burstein-Moss shift) is a well-know effect in In_2O_3-based materials (13, 14, 1). The widening of the bad gap due to the Burstein-Moss shift is given by (1)

$$\Delta E_g = \frac{\hbar^2}{2m^*}(3\pi^2 n)^{\frac{2}{3}} \qquad [1]$$

where n is the free carrier density and m^* is the electron effective mass. From a plot of E_g vs. $n^{2/3}$ (Fig. 6, inset), the electron effective mass may be calculated, and our result of $0.3m_e$ (where m_e is the free electron rest mass) is in good agreement with values for ITO and IMO (9, 1).

The development of high mobility TCO's may increase their potential applications for usage in the IR since the transparency is extended to longer wavelengths. To examine the optical properties of a high mobility TCO we compared the NIR optical properties an IWO film with μ = 80 cm^2/Vs and n = 8.3 x 10^{19} cm^{-3} and an ITO film with μ = 38 cm^2/Vs and n = 4.5 x 10^{20} cm^{-3} (Fig 7). Both samples were deposited onto a-SiO_2 substrates, which are non-absorbing for $\lambda < 2.5$ μm at which point the substrate begins to absorb. The transmittance of the IWO (solid curve) and ITO films (dash-dot curve) are shown in the top pane. For IWO, the transmittance is extended further into the IR, and the drop off in transmittance is less precipitous. The reflectance and absorbance are plotted in the middle and lower panes, respectively. The reflectance turn-on is pushed further into the IR, while the

magnitude of the IR absorbance is reduced and the peak absorption position shifted to longer wavelength. Hence IWO thin films exhibiting high mobility and low carrier density result in enhanced NIR transmissivity and reduced optical absorption compared to ITO films with conventional mobility. These attributes may be beneficial if IWO films were to be used as a transparent electrode in a solar cell or an IR sensor.

X-ray Photoelectron Spectroscopy of High Mobility IWO Thin Films

A high resolution XPS spectrum from an IWO film with $\mu = 112$ cm^2/Vs is shown in Fig. 8 in which the photoelectron count intensity is plotted against the electron binding energy. The 4*f* electrons of W have binding energies (BE) in this range, and the doublet peak in the spectrum (caused by spin-orbit splitting) at 35.2 eV ($4f_{7/2}$) and 37.4 eV ($4f_{5/2}$) correspond to the electron binding energies for a high oxidation state of W, either W^{6+} or W^{5+} (20). The binding energies of these ions are very close ($4f_{7/2}$ of W^{6+} at 35.8 eV, W^{5+} at 35.4 eV) making definitive assignment of the peaks difficult. However, the targets were prepared using WO_3, so we may expect to measure binding energies from W^{6+} ions only. One possible cause of the displacement of the film spectrum to lower BE relative to the literature BE value for W^{6+} ions is sputter-induced reduction (20) as the sample was lightly sputter cleaned prior to analysis using Ar+ ions. Note also that the doublet peak is resolved, and most likely indicates a majority oxidation state, as mixed oxidation states often result in peak convolution and smearing when the binding energies of different ions are very close, as they are in W. Hence, in high mobility IWO films, W exists in a high

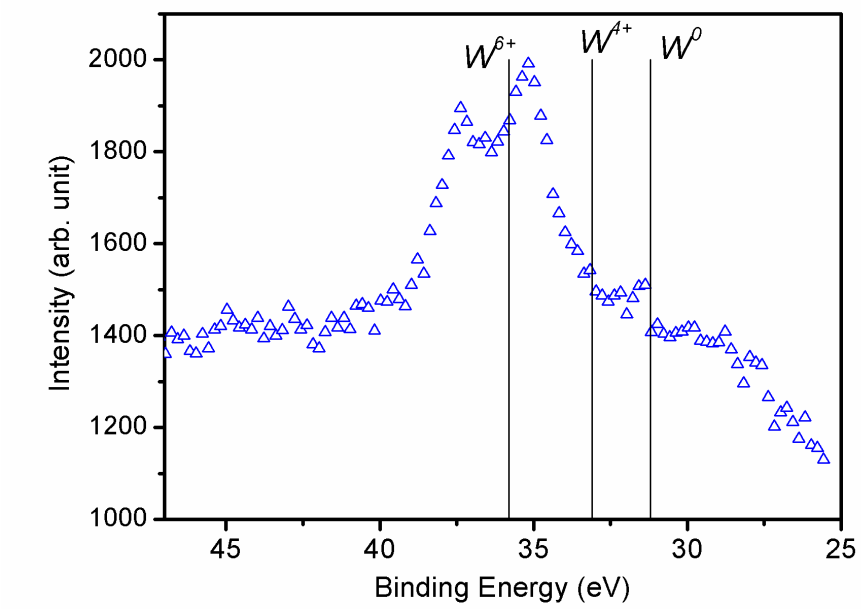

Fig. 8 XPS spectrum of IWO film with μ = 112 cm^2/Vs. The W $4f_{7/2}$ and $4f_{5/2}$ spin orbit doublet is clearly observed. Vertical line show the position for the $4f_{7/2}$ peak for W^{6+}, W^{4+}, and W^0 ions. The film peaks are shifted to lower energy relative to fully oxidized W^{6+}, indicating partial reduction may have occurred in the course of surface ion milling.

oxidation state of W^{6+} or W^{5+}. In principle then, W substitution of In should generate two or three free carriers per W atom (i.e. $W_{In}^{\bullet\bullet}$ or $W_{In}^{\bullet\bullet\bullet}$) providing a much more efficient means of doping in In_2O_3 with only a very small dopant concentration needed to achieve a high free carrier density. However, this is not observed experimentally, and the carrier concentration of high mobility IWO films (1-3 x 10^{20} cm^{-3}) is notably lower than ITO films (0.5-2 x 10^{21} cm^{-3}), in which at most one free electron is generated per Sn substitution. Unit doping efficiency has been observed in single crystal ITO films (17), while in high mobility IWO films the doping efficiency is 0.75-1 electrons/W. Therefore, in IWO the triply or doubly positive $W_{In}^{\bullet\bullet\bullet}$ defect is probably charge compensated by O_i, forming $[W_{In}^{\bullet\bullet\bullet} O_i'']^{\bullet}$. The formation of these complexes has been shown to be energetically favorable in IMO and IWO (15, 21).

Discussion

Electronic structure calculations performed on 6.25% Mo-doped In_2O_3 reveal an unexpected mechanism for the high mobility: transition metal magnetic exchange interactions. The reader is referred to (15, 21) for a complete description. Briefly, even though Mo is non-magnetic in bulk the total calculated energy difference between magnetic and non-magnetic configurations of $Mo_{In}^{\bullet\bullet\bullet}$ defects was shown to be considerable, up to 0.56 eV of energy gain, and Mo atoms posses a large magnetic moment up to 1.85 μ_B. The exchange interactions split the Mo *d*-states near E_F into two spin channels. As a result, the carriers of one spin will be affected by only half of

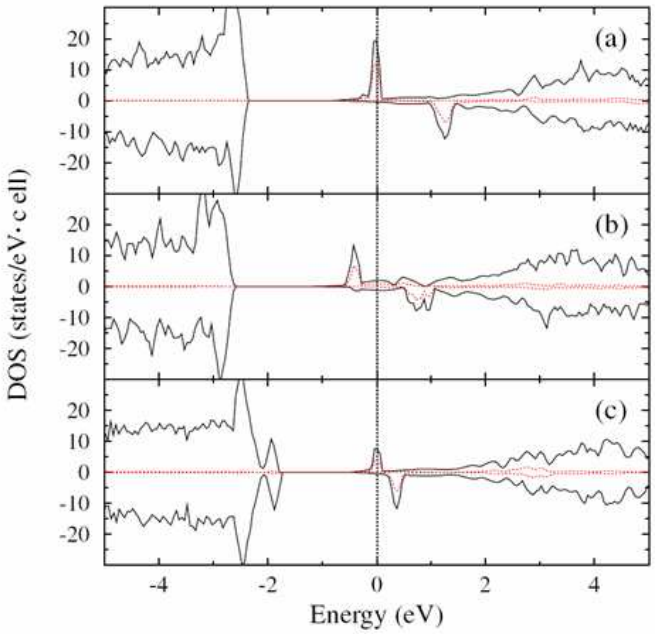

Fig. 9 The Total (black) and Mo *d* state (red) density of states for $Mo_{In}^{\bullet\bullet\bullet}$ defects (9a and 9b, which differ in crystallographic substitutional site) and oxygen compensated $[Mo_{In}^{\bullet\bullet\bullet}O_i'']^{\bullet}$ species (c). Mo magnetic exchange interactions split the Mo *d* states near E_F. The splitting is large in the case of $Mo_{In}^{\bullet\bullet\bullet}$ defects (a and b) in which Mo atoms posses a large magnetic moment of up to 1.85 μ_B, and not as big in the oxygen compensated complex, which attenuates the exchange interactions and the Mo atom magnetic moment. However, the exchange energy is still large enough from $[Mo_{In}^{\bullet\bullet\bullet}O_i'']^{\bullet}$ to create two spin channels such that carriers may only scatter from states of the same spin. Carriers of the opposite spin will not scatter from these states. This effectively reduces the number of scattering centers by half, imparting carriers with high mobility.

the Mo defect scattering centers, those of the same spin. The concentration of Mo scattering centers is then effectively reduced to half of the Mo doping level. This is in a sense similar to the preliminary explanations of high mobility in these systems, which posed that ultra high carrier generation of $Mo_{In}^{\bullet\bullet\bullet}$ defects generate carriers more efficiently than $Sn_{In}^{\bullet}$, resulting in an equivalent carrier concentration with far fewer $Mo_{In}^{\bullet\bullet\bullet}$ scattering centers (6). The splitting of the Mo *d* states near E_F is shown in the DOS plot for the $[Mo_{In}^{\bullet\bullet\bullet}O_i'']^{\bullet}$ complex (Fig. 9c) in which a splitting of ~ 0.4 eV is calculated. O_i suppress the exchange interactions considerably compared to non-oxygen compensated defects like $Mo_{In}^{\bullet\bullet\bullet}$ (Fig. 9a and 9b), but there is still sufficient exchange energy to split the Mo *d* states near E_F. The formation $[Mo_{In}^{\bullet\bullet\bullet}O_i'']^{\bullet}$ complexes has been shown to be very favorable in this system, with an energy gain of ~ 3 eV, and such complexes should be the primary charge generating defects. Unpublished calculations reveal the same effects are calculated from W-doped In_2O_3.

Conclusion

In summary, we have prepared high electron mobility thin films of transparent conductor $In_{2-x}W_xO_3$ on vitreous SiO_2 substrates which exhibit $\mu = 112$ cm^2/V, $n = 1.67 \times 10^{20}$ cm^2/Vs, and $\rho = 3.37 \times 10^{-4}$ Ohm cm at room temperature. Low temperature Hall effect measurements on high mobility IWO films indicate that the electron mobility is constrained by phonon scattering, but ionized impurity scattering is significant for higher doping levels. The films were prepared by pulsed laser deposition from both low density and high density ceramic In_2O_3:WO_3 targets, the main distinction between the two families of targets being the maximal allowable laser

fluence. EPMA revealed that incongruent evaporation of W from the low density targets occurred due to the use of low laser fluence, while films prepared from high density targets with high laser fluence had predictable film W concentration. The highest mobility and conductivity was measured for films with $x \sim 0.03$ (= 1.5 cation %). The mobility values measured from IWO films are 2-4 times greater than the mobility of ITO thin films and offer significant enhancements to the NIR optical properties compared to conventional mobility TCO materials. In particular, the IR transmittance is extended to longer wavelength while the magnitude of the IR absorbance is reduced and the peak absorption position shifted further into the IR. On single crystal YSZ substrates, IWO films grown preferentially along [100] while films grown on a-SiO_2 show statistical crystallite orientation. The band gap of IWO films ranged between 3.80-3.91 eV, and widening of the band gap with increasing carrier concentration was ascribed to the Moss-Burstein effect. Using the MB framework we calculated the electron effective mass to be $0.3m_e$, in close agreement with related systems. The mechanism for high mobility in refractory metal doped In_2O_3 has been elucidated theoretically in which it is shown that Mo magnetic exchange interactions split the Mo *d* states near E_F, creating two spin channels and reducing the number of Mo defect scattering centers to only defects of the same spin.

Acknowledgements

We thank John Donovan of the Center for Advanced Materials Characterization in Oregon (CAMCOR) for assistance with the film composition measurements, Tim Murrell for the low temperature Hall effect measurements, and

Susan Guyler for assistance with the optical measurements. Thanks also to Peter Nyholm and Hewlett Packard, who facilitated and provided funding for the high density commercial targets. William Stickle at Hewlett Packard performed the XPS measurements. This research is based on work supported by the National Science Foundation under Grant No. 0245386 and by the Army Research Office under MURI E-18-667-G3.

References

(1) Hamberg, I.; Granqvist, C. G. *J. Appl. Phys.* **1986**, *60*, R123.

(2) Maruyama, T.; Tago, T. *Appl. Phys. Lett.* **1994**, *64*, 1395.

(3) Tahar, R. B. H.; Ban, T.; Ohya, Y.; Takahashi, Y. *J. Appl. Phys.* **1998**, *83*, 2631.

(4) Warmsingh, C.; Yoshida, Y.; Readey, D. W.; Teplin, C. W.; Perkins, J. D.; Parilla, P. A.; Gedvilas, L. M.; Keyes, B. M.; Ginley, D. S. *J. Appl. Phys.* **2004**, *95*, 3831.

(5) van Hest, M. F. A. M.; Dabney, M. S.; Perkins, J. D.; Ginley, D. S.; Taylor, M. P. *Appl. Phys. Lett.* **2005**, *87*, 032111.

(6) Meng, Y.; Yang, X.; Chen, H.; Shen, J.; Jiang, Y.; Zhang, Z.; Hua, Z. *Thin Solid Films*. **2001**, *394*, 218.

(7) Newhouse, P. F.; Park, C.; Keszler, D. A.; Tate, J.; Nyholm, P. S. *Appl. Phys. Lett.* **2005**, *87*, 112108.

(8) Koida, T.; Kondo, M. *Appl. Phys. Lett.* **2006**, *89*, 082104.

(9) Yoshida, Y.; Wood, D. M.; Gessert, T. A.; Coutts, T. J. *Appl. Phys. Lett.* **2004**, *84*, 2097.

(10) Ohta, H.; Orita, M.; Hirano, M.; Tanji, H.; Kawazoe, H.; Hosono, H. *Appl. Phys. Lett.* **2000**, *76*, 2740.

(11) Newhouse, P. F; Park, C-H.; Keszler, D. A.; Tate, J.; Nyholm, P. S. *Mat. Res. Soc. Symp. Proc.* **2006**, *905E*, 0905-DD01-02.1.

(12) Coutts, T. J.; Young, D. L.; Li, X. *Mat. Res. Soc. Bull.* **2000**, *25*, 58.

(13) Burstein, E. *Phys. Rev.* **1953**, *93*, 632.

(14) Moss, T. S. *Proc. Phys. Soc. London*. **1954**, *B67*, 775.

(15) Medvedeva, J. E. *Phys. Rev. Lett.* **2006**, *97*, 086401.

(16) Moulder, J. F.; Stickle, W. F.; Sobol, P. E.; Bomben, K. D. *Handbook of X Ray Photoelectron Spectroscopy: A Reference Book of Standard Spectra for Identification and Interpretation of XPS Data*; Reissue.; Physical Electronics, 1995.

(17) Ohta, H.; Orita, M.; Hirano, M.; Hosono, H; Kawazoe, H.; Tanji, H. *Mat. Res. Soc. Proc.* **2000**, *623*, 253.

(18) Chrisey, D. B.; Hubler, G. K. *Pulsed Laser Deposition of Thin Films*; 1st ed.; Wiley-Interscience, 1994.

(19) Laux, S.; Kaiser, N.; Zoller, A.; Gutzelmann, R.; Lauth, H.; Bernitzki, H. *Thin Solid Films*. **1998**, *335*, 1.

(20) Wong, H. Y.; Ong, C. W.; Kwok, R. W. M.; Wong, K. W.; Wong, S. P.; Cheung, W. Y. *Thin Solid Films*. **2000**, *376*, 131.

(21) Medvedeva, J. *Appl. Phys. A.* **2007**, *89*, 43.

CHAPTER 4

Thin Film Preparation and Characterization of p-type Semiconductor BiCuOSe

P. F. Newhouse[a,b], P. A. Hersh[b], R. Kykyneshi[b], D. A. Keszler[a,b], and J. Tate[a,b].

[a] Department of Physics, Oregon State University, 301 Weniger Hall, Corvallis, Oregon USA 97331-6507

[b] Department of Chemistry, Oregon State University, 153 Gilbert Hall, Corvallis, Oregon USA 97331-4003

A modified version of this work appears as

J. Tate, P. F. Newhouse, R. Kykyneshi, P. A. Hersh, J. Kinney, D. H. McIntyre, D. A. Keszler, *Thin Solid Films* **516** *5795 (2008).*

Abstract

Strongly *c*-axis oriented thin films of p-type semiconductor BiCuOSe:Ca have been prepared in-situ on MgO (100) and $SrTiO_3$ (100) single crystal substrates at 450 °C by pulsed laser deposition. Undoped, *c*-axis oriented thin films on MgO exhibit a conductivity of 9 S/cm and mobility of 4 cm^2/Vs, while Ca-doped films on $SrTiO_3$ show enhanced conductivity of 176 S/cm and mobility of 1.7 cm^2/Vs. Polycrystalline films prepared on amorphous SiO_2 substrates exhibit a mobility of 2 cm^2/Vs and 9 S/cm. BiCuOSe thin films are dark and reflective over the visible range, with no transmission of light with energy greater than 1.77 eV, at which point the films begin to become non-absorbing. An index of refraction of 4.79 at 1 μm was calculated from a BiCuOSe thin film. Films prepared on $SrTiO_3$ show stronger *c*-axis growth orientation than films prepared on MgO, as show by x-ray rocking curve measurements.

Introduction

The family of Cu(I)-containing chalcogenide-fluorides (BaCuChF, Ch = S, Se, Te) and oxy-chalcogenides (MCuOCh, M = lanthanide or Bi) show several interesting and technologically significant properties including degenerate p-type electrical conductivity, room temperature excitons, and a natural quantum well crystal structure which consists of layers of narrow band gap $(Cu_2Q_2)^{2-}$ and wide band gap $(Ln_2O_2)^{2+}$ stacked alternately along the *c*-axis of a tetragonal unit cell (s.g *P-4mm*) (1-7). The same layered crystal structure has shown the ability to accommodate many different ions including As, Ni and Zn, leading to new materials explorations and widely varying properties such as high temperature superconductivity and ferromagnetism (8-11). Additionally, thin films of LaCuOSe and BaCuTeF exhibit an overall wide optical band gap (>3 eV) and simultaneous electrical conductivity, opening up new possibilities for active devices based on transparent p-type semiconductors. However, high quality thin films of LaCuOCh cannot be prepared *in-situ* by physical vapor deposition techniques, and successful film growth requires a multi-step *in-situ* deposition process followed by *ex-situ* post deposition annealing at high temperatures in specialized environments (12). BiCuOSe shows no visible transparency, but does exhibit high conductivity and hole mobility, indicating that it may find application as an absorber layer in a thin film solar cell. In this chapter, we show that high crystal quality thin films of BiCuOSe:Ca can be prepared *in-situ* at moderate temperature using pulsed laser deposition (PLD). In particular, we have prepared strongly *c*-axis oriented BiCuOSe thin films on MgO (100) and $SrTiO_3$ (100) substrates at 450 °C which exhibit conductivity >175 S/cm and a reasonably high hole mobility ranging

from 1.7 cm^2/Vs for high carrier density Ca-doped films to 4.0 cm^2/Vs for undoped films on MgO. Polycrystalline undoped films on vitreous SiO_2 can be grown at even lower temperature of 400 °C, and exhibit a mobility of 2 cm^2/Vs. In Fig. 5 and 6, the UV–vis–NIR optical properties for a polycrystalline BiCuOSe film are presented. The films are darkly-colored and reflective in the visible range indicating a sub-visible band gap. The films transmit light in the NIR region, and the refractive index at 1000 nm was determined to be 4.79. X-ray rocking curves from BiCuOSe films are shown in Fig. 3 and indicate a stronger *c*-axis growth orientation for films grown on $SrTiO_3$ compared to MgO. Also, the results of LAPW electronic structure calculations are summarized which show that the CBM is formed from low-lying Bi 6*p* states, effecting a much lower band gap energy BiCuOCh compared to LaCuOCh.

Experiment

Thin films of BiCuOSe were deposited onto heated GE 124 amorphous SiO_2 (a-SiO_2) and single crystal MgO (001) and $SrTiO_3$ (001) substrates using pulsed laser ablation of ceramic BiCuOSe targets in a high vacuum chamber. Films were deposited in vacuum or in 1.5-1.7 mtorr of grade 5.0 Ar using Lambda Physik Compex 201 excimer laser (λ = 248 nm, τ = 25 ns) set to 10 Hz and 1.0-1.6 J/cm^2. The target was positioned 50 mm from the substrate, which was heated to 375-450 °C. For target preparation, powders of $Bi_{1-x}Ca_xCuOSe$ were prepared by solid state reaction of Bi_2O_3 (Strem 99.999%), CaO (99.8%), Bi (Strem 99.9%), Cu_2Se (Cerac 99.5%), and Se (cerac 99.6%) in an evacuated silica tube heated to 500 °C for 12 h. Powders with x = 0, 0.1, and 0.15 were then cold pressed into 1″ diameter pellets at 4

tons/in^2 and sintered at 850 °C under 2000 PSI of commercial grade Ar. The resulting targets were black and rather grainy, exhibiting 50-60% density. After deposition the films cooled to near room temperature in the deposition ambient. Films were characterized by fixed incidence and θ–2θ x-ray diffraction (XRD), electrical conductivity (σ), variable field Hall effect transport measurements, and by UV–vis–NIR transmission and reflection. Fixed incident angle XRD spectra (Cu K_α) were measured using a Rigaku Rapid R-axis diffractometer while a Siemens D5000 diffractometer was used to acquire θ–2θ XRD patterns. For measurements using the Rapid R-axis diffractometer a two-dimensional area detection screen allowed reflections from a range of 2θ and χ angles to be acquired simultaneously. Electrical conductivity and Hall mobility (μ) were measured at room temperature in the van der Pauw configuration with a Lakeshore 7504 Hall measurement system at fields of 5-20 kG. NIR transmittance and reflectance spectra were acquired using a Nicolet Nic-Plan microscope accessory fitted to a Magna 750 Fourier transform infrared spectrometer. Spectra are the average of 256 Fourier transformed interferograms over 11700-2100 cm^{-1} with 4 cm^{-1} resolution. Air and a gold mirror were used for transmission and reflection background calibration.

Results and Discussion

Structural Characterization of BiCuOSe Thin Films

The XRD patterns from undoped BiCuOSe powder and a thin film are shown in Fig 1. The film deposited in vacuum on vitreous SiO_2 at 400 °C is pure phase and exhibits statistical orientation, which is easily noted from the close match in peak intensity ratios from the powder and film. The facile crystallization of BiCuOSe thin films is a key point in the potential use of this material, with closely related materials requiring high temperatures and *ex-situ* processing (12). In contrast to BiCuOSe films deposited on vitreous SiO_2 substrates, films prepared on single crystal MgO (100) and $SrTiO_3$ (100) substrates at only ~450 °C show strong *c*-axis growth orientation, such that peaks of type (00*l*) are preferred while polycrystalline (*hkl*) peaks are suppressed (Fig. 2). The diffraction peaks from the film prepared on $SrTiO_3$ are narrower and more intense than those of the film prepared on MgO, indicating a greater degree of *c*-axis orientation. This may be expected as the *a* lattice constant match of BiCuOSe on $SrTiO_3$ (0.4%) is significantly better than on MgO (7.4%). To verify that $SrTiO_3$ provides a better template for *c*-axis growth than MgO, x-ray rocking curves were performed on the BiCuOSe (005) peak. As shown in Fig. 3, the film deposited on MgO (outer peak) has a 3° line width, while the film grown on $SrTiO_3$ (middle peak) shows a line width of about 1°, indicating stronger *c*-axis grain orientation in the film prepared on $SrTiO_3$. The bulk single crystal rocking curve from the $SrTiO_3$ (002) reflection is also shown as a line width reference and the limit of instrumental resolution (inner most peak). The peaks have been vertically displaced slightly.

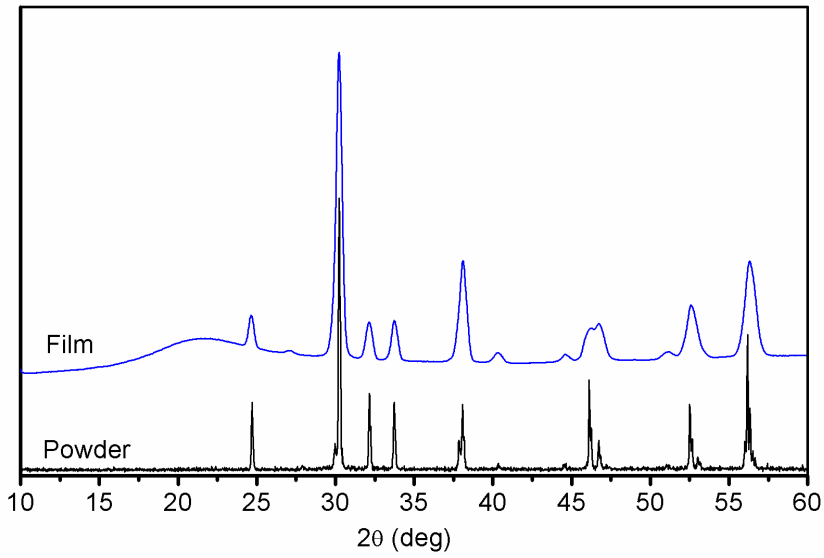

Fig. 1 Polycyrstalline BiCuOSe thin film (upper pane) and powder (lower pane) XRD patterns. The film was deposited in vacuum at 400 C on a-SiO_2.

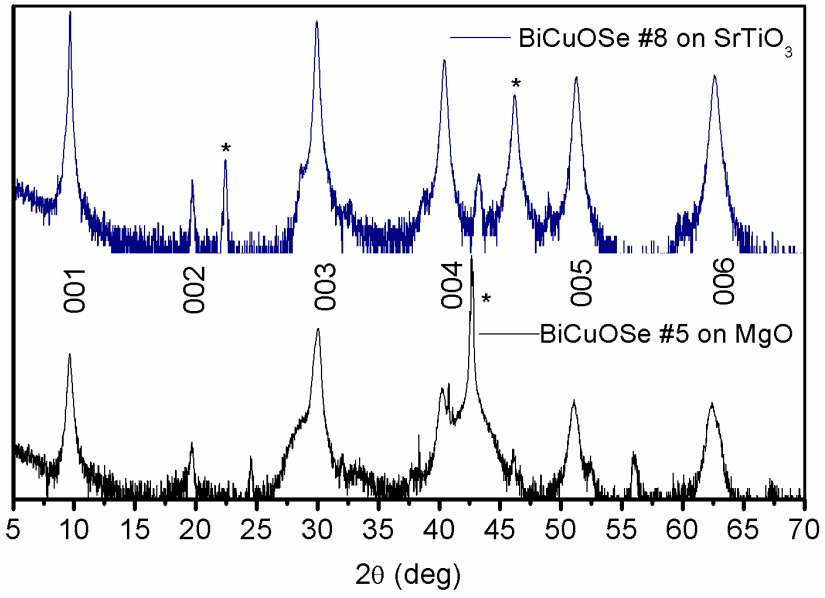

Fig. 2 The θ–2θ XRD patterns from *c*-axis oriented BiCuOSe films prepared on single crystal substrates of $SrTiO_3$ (100) and MgO (100) (plotted on a log scale). The (00*l*) film reflections are labeled and asterisks mark substrate reflections. The diffraction peaks from the film on $SrTiO_3$ are narrower and more intense than those from the film on MgO, indicating a greater degree of preferential orientation.

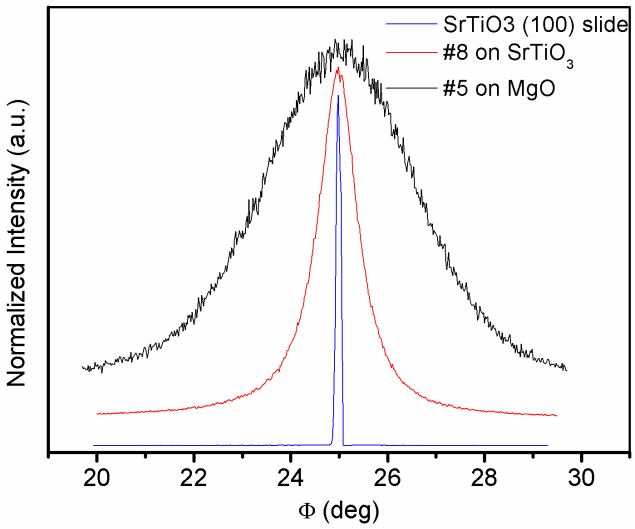

Fig. 3 The (005) x-ray rocking curves from films prepared on single crystal substrates of MgO (outer curve) and SrTiO3 (middle curve). A significant decrease in line width is observed from the film prepared on SrTiO3, indicating a stronger degree of c-axis orientation. The inner-most curve is from the $SrTiO_3$ substrate.

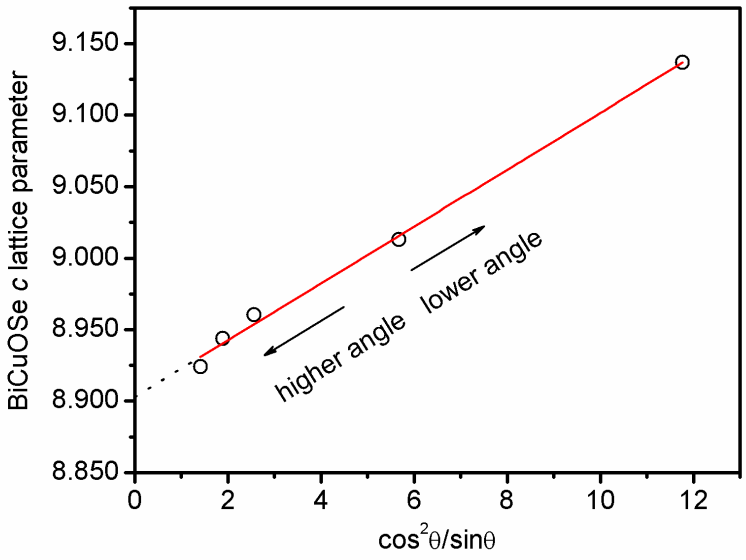

Fig. 4 *d*-spacing of a BiCuOSe film extrapolated against $\cos^2\theta/\sin\theta$ to correct for sample vertical displacement. The extrapolated value is 8.903 Å, while the powder refinement at this doping level is 8.904 Å (x = 0.1). Note that the accuracy improves at higher angle.

Plane spacings in a tetragonal unit cell are given by (13)

$$\frac{1}{d^2} = \frac{h^2 + k^2}{a^2} + \frac{l^2}{c^2} \qquad [1]$$

Hence, the line position of each peak with index (00*l*) depends only on the *c* lattice parameter, while the line position from peaks of type (*hk*0) depend solely on *a*. For the XRD patterns in Fig. 2, multiple thin film (00*l*) peaks are observed, each peak representing a value of *d*. By plotting each value of *d* against the appropriate function of angle, we can remove systematic errors like specimen absorption and displacement from the diffractometer axis, the latter considered to be largest single source of error (13). The error in *d* from this phenomenon is given by

$$\frac{\Delta d}{d} = -\frac{D}{R}\frac{\cos^2\theta}{\sin\theta} \qquad [2]$$

where *D* is the specimen displacement parallel to the reflecting plane normal and *R* is the diffractometer radius. Plotting *d* versus $\cos^2\theta/\sin\theta$ will allow for the most accurate extrapolation of *d*, which for the (00*l*) diffraction peaks is simply the *c*-axis lattice parameter. The results of this procedure for the BiCuOSe film on MgO in Fig. 2 are shown in Fig. 4. Discrete calculations of *d* from each (00*l*) peak are plotted as open circles. A linear fit extrapolated to the y-axis provides the most accurate value of *d*. The extrapolated value of 8.903 Å for the Ca-doped film agrees well with the refined powder value at that doping level 8.904 Å ($x = 0.1$). Note that the accuracy of the calculated *d* value improves when θ is large.

Optical properties

The UV–vis–NIR optical transmission *T* and reflection *R* for a polycrystalline BiCuOSe film prepared on a-SiO_2 are shown in Fig. 5. The film exhibits high reflectance of 30-36% over the visible range, and a weak onset of transmission beginning near 750 nm (=1.65 eV), indicated by an arrow. The transmission onset is broad, which makes assignment of the band gap energy difficult. In the powder, however, a clear absorption edge ascribed to the band gap was measured at much lower energy (0.8 eV), in agreement with the black appearance of the powder and films (14). However, this does not comport with our thin film measurements. Further into the IR, thin film interference fringes dominate the *T* and *R* spectra, as shown in Fig. 6. The high reflectance amplitude is consistent with a large index mismatch at the air-film interface. The wavelength positions of the extrema are used to calculate discrete values of the refractive index (Fig. 6, diamonds) using a simple Bragg relation. These data are then fit to $n \sim 1/\lambda^2$ to generate the continuous dispersion relation in Fig 6. Calculated optical spectra can then be obtained and fit to the experimental spectra. The calculated spectra overlay the experimental spectra in Fig. 6, indicating an acceptable fit, with fit parameters of d = 290 nm and n = 4.79 at 1 μm.

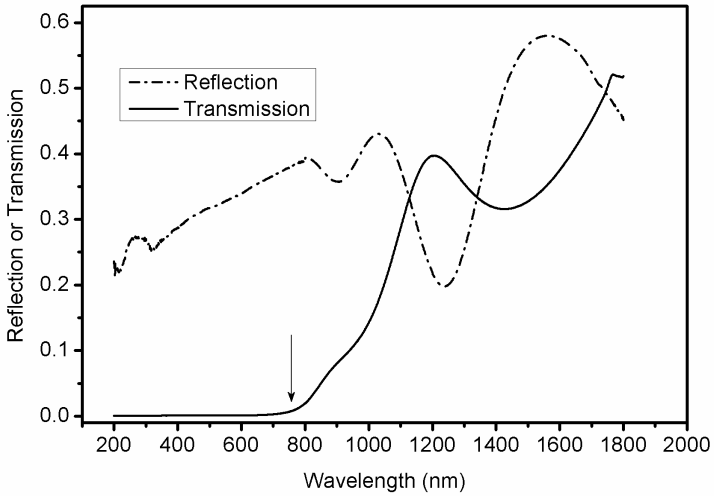

Fig. 5 UV–vis–NIR Reflection and Transmission spectra from a polycrystalline BiCuOSe film on a-SiO_2. The films are black and reflective in the visible range. A weak onset in the transmission can be observed near 750 nm (=1.65 eV) indicated by an arrow.

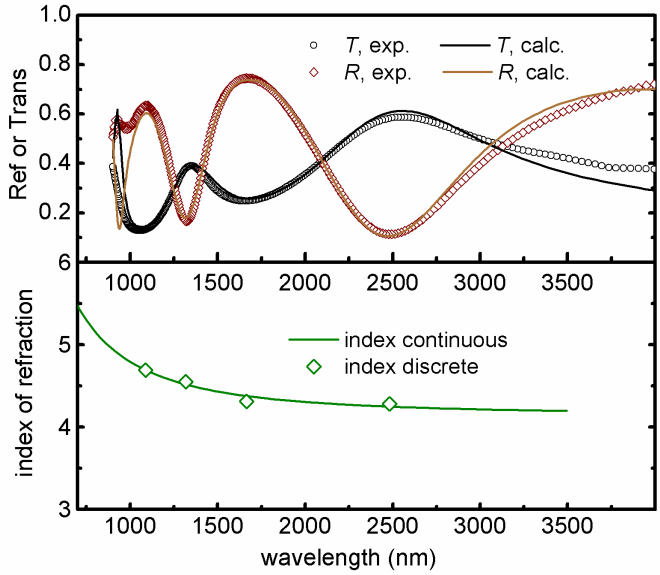

Fig. 6 The NIR reflection and transmission from a polycrystalline BiCuOSe film on a-SiO_2 The calculated reflection and transmission spectra are obtained using the dispersive index, plotted in the lower pane. Discrete calculations of the index are shown as diamonds.

Electronic Properties

Hall effect measurements show that undoped and Ca-doped BiCuOSe films exhibit p-type conductivity indicated by positive values of the Hall coefficient. In Fig. 7, the transport properties of several *c*-axis oriented BiCuOSe films are plotted as a function of Ca content in the target. The undoped film prepared on MgO (100) exhibits a conductivity of 9 S/cm with 1.4 x 10^{19} cm^{-3} and the highest measured mobility of 4 cm^2/Vs. Films prepared on $SrTiO_3$ from Ca-doped targets show elevated conductivity and free carrier density relative to undoped films with the expected fall off in mobility, due most likely to ionized impurity scattering. Hence Ca substitution of Bi in BiCuOSe is an effective method of acceptor doping, a result which is consistent with the closely related $Bi_{1-x}Sr_xCuOSe$ system (15). The conductivity reaches its maximum value of 176 S/cm when $x_{target} = 0.15$ by which point conductivity gains begin to saturate. The mobility remains reasonably high near 2 cm^2/Vs, which is equal to the value measured from polycrystalline films prepared on a-SiO_2 substrates (not plotted). High conductivity p-type films with reasonably high mobility and simple fabrication may be useful as absorber or p++ layers in thin film solar cells. The film conductivity results are consistent with resistivity measurements of Ca-doped pellets, which reveal a steady decrease in the resistivity up to $x = 0.15$, with a sharp resistivity increase when $x = 0.2$ (16). Indeed, powder diffraction measurements reveal that compositions with $x < 0.2$ are single phase, while the $x = 0.2$ powder exhibits secondary phases. Powder refinements also show that the *a* and *c* lattice parameters cease to change when $x > 0.15$, indicating the solubility limit of Ca

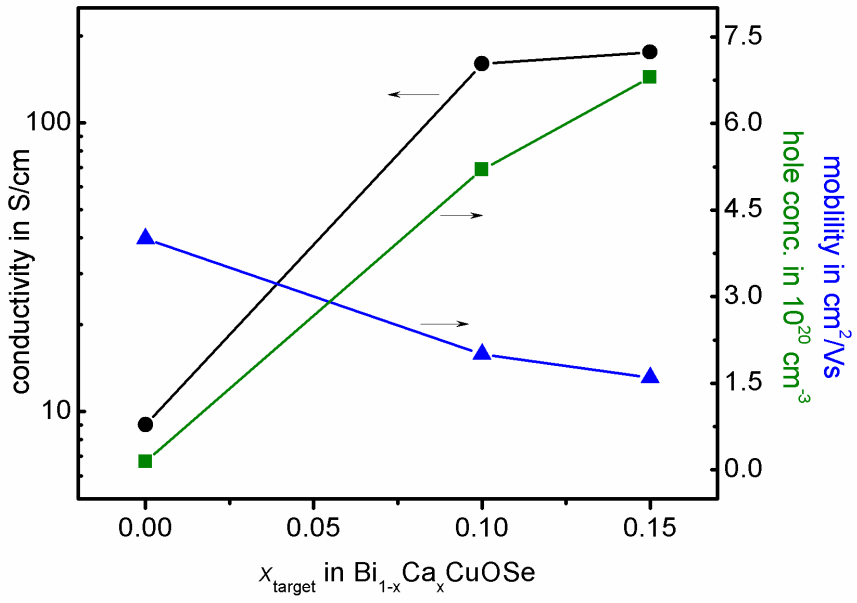

Fig. 7 Transport properties of *c*-axis oriented $Bi_{1-x}Ca_xCuOSe$ films on $SrTiO_3$ and MgO plotted versus the Ca content in the target. The rise in carrier concentration (right hand axis, linear scale) and conductivity (left hand axis, log scale) with simultaneous fall off in hole mobility are consistent with carrier generation from hole generation from Ca substitution of Bi. The lines are a guide to the eye.

in BiCuOSe powder (16).

Discussion

Our interest in the BiCuOSe system emerged from work in our group (1, 2, 17, 18) on BaCuChF (Ch = S, Se, Te) and LaCuOCh, all of which share the atomic arrangement of wide band gap metal oxide or metal fluoride layers and narrow gap copper chalcogenide layers stacked alternately along the *c*-axis of a tetragonal unit cell. However some notable difference between the Bi-based and La-based materials were immediately apparent. For instance, LaCuOCh power appears grayish (E_g = 3 eV for Ch = S) while BiCuOSe powder is black. Also, thin films of LaCuOCh cannot be prepared *in-situ* using PLD (reactive solid phase epitaxy (12) must be used), while BiCuOSe exhibits facile *in-situ* crystallization by PLD in vacuum at 400 °C. The distinct physical differences that exist between BiCuOCh and LaCuOCh stem from the disparate electronic configurations of the trivalent cations Bi^{3+} (= $[Xe]4f^{14}5d^{10}6s^{2}6p^{0}$) and Ln^{3+} (= $[Xe]4f^{0}5d^{0}6s^{0}$) (14). The $6s^2$ configuration of Bi^{3+} has the potential to form hybrid bands with the Cu *d* and Ch *p* orbitals that compose the VBM. The large, spherically symmetric 6*s* orbitals would increase the dispersive character of the VBM and provide a more conducive hole transport path. This contrasts with LaCuOCh, which affords no possibility of *s* orbital mixing due to the closed shell electronic configuration of La^{3+}. Thus we expect the hole transport properties in BiCuOCh to be quite different than in LaCuOCh, but this is not observed experimentally. The hole conduction properties of BiCuOCh and LaCuOCh are observed to be quite similar,

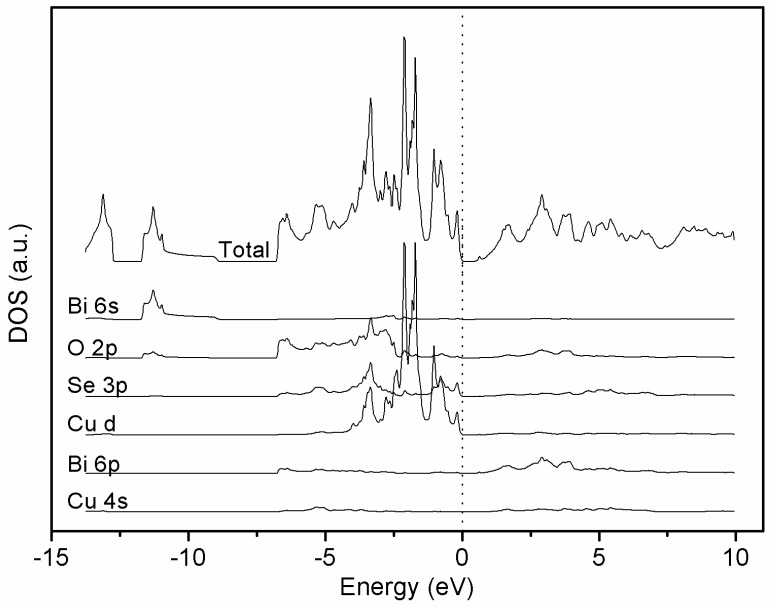

Fig. 8 The total and partial DOS calculated for BiCuOSe using the LAPW method. The Bi 6*s* states near -11 eV are far removed from the VBM and do not hybridize with Cu *d* and Ch *p* near the VBM. In the CB, Bi 6*p* states lie near the CBM, effecting a much lower band gap energy in BiCuOCh than LaCuOCh.

and on this basis the Bi 6*s* contribution to the VBM is expected to be small (14). The total and PDOS for BiCuOSe is shown in Fig. 8 and shows that the Bi *s* states lie approximately 11 eV away from the VBM and thus do not make any significant contribution at the VBM. Thus, the VBM structure of the Bi-based and La-based materials are similar (both consist of admixed Cu *d* and Ch *p* states) and hence the difference in the energy gaps of the materials should be attributed to differences in the CBM. Indeed, our calculations show that the CBM is comprised mainly of Bi 6*p* states, a result completely different from LaCuOCh, in which the CBM is made up of Cu *s* and La *d* states (14). These Bi 6*p* states lie low in the CB and effect a much lower band gap of BiCuOCh compared to LaCuOCh. The fact that Bi 6*s* does not hybridize with Ch *p* at the VBM can be explained using results of careful Rietveld refinements (14), which show that the Bi–O bonds are significantly shorter than the Bi–Ch bonds, indicating stronger orbital overlap. Stronger covalent bonding (i.e. shorter bond distances) of the Bi–O bond compared to the Bi–Ch bond result in Bi *6s* and O 2*p* hybridization deep below the VBM rather than Bi 6*s* Ch *p* hybrid orbitals at the VBM. The Bi 6*s*–O 2*p* mixing deep in the VB is clearly seen in the PDOS of Fig. 8.

Conclusion

In summary, we have prepared strongly *c*-axis oriented thin films of p-type semiconductor BiCuOSe:Ca *in-situ* on MgO (100) and $SrTiO_3$ (100) single crystal substrates at moderate substrate temperature of 450 °C by pulsed laser deposition. Undoped, *c*-axis oriented thin films on MgO exhibit $\sigma = 9$ S/cm, $n = 1.4 \times 10^{19}$ cm^{-3},

and μ = 4 cm^2/Vs, while Ca-doped films on $SrTiO_3$ show increased conductivity and carrier density of 176 S/cm and 6.8 x 10^{20} cm^{-3}, with a mobility of 1.7 cm^2/Vs, indicating that Ca substitution of Bi is an effective method of acceptor doping in BiCuOSe. Single phase polycrystalline films can be prepared on vitreous SiO_2 substrates at 400 °C and show μ = 2 cm/Vs and σ = 10 S/cm. The facile *in-situ* thin film preparation and dopability characteristics of BiCuOSe may be useful for applications which require the use of p++ layers with high conductivity and moderate hole mobility. In the optical range, BiCuOSe thin films are dark-colored and reflective with an onset of transmission in the NIR. An index of refraction of 4.79 at 1 μm was calculated from a BiCuOSe thin film. Films prepared on $SrTiO_3$ show stronger *c*-axis growth orientation than films prepared on MgO, as show by x-ray rocking curve measurements.

Acknowledgements

The authors acknowledge support from the National Science Foundation DMR 0245386 and helpful discussions with A. Zakutayev. PFN acknowledges support from an NSF IGERT (DGE 0549503).

References

(1) Park, C.; Kykyneshi, R.; Yokochi, A.; Tate, J.; Keszler, D. A. *J. Solid State Chem*. **2007**, *180*, 1672.

(2) Yanagi, H.; Tate, J.; Park, S.; Park, C.; Keszler, D. A. *Appl. Phys. Lett.* **2003**, *82*, 2814.

(3) Hiramatsu, H.; Ueda, K.; Ohta, H.; Hirano, M.; Kamiya, T.; Hosono, H. *Thin Solid Films*. **2003**, *445*, 304.

(4) Hiramatsu, H.; Ueda, K.; Ohta, H.; Hirano, M.; Kikuchi, M.; Yanagi, H.; Kamiya, T.; Hosono, H. *Appl. Phys. Lett.* **2007**, *91*, 012104.

(5) Hiramatsu, H.; Ueda, K.; Takafuji, K.; Ohta, H.; Hirano, M.; Kamiya, T.; Hosono, H. *J. Appl. Phys*. **2003**, *94*, 5805.

(6) Ueda, K.; Inoue, S.; Hosono, H.; Sarukura, N.; Hirano, M. *Appl. Phys. Lett.* **2001**, *78*, 2333.

(7) Ueda, K.; Hiramatsu, H.; Ohta, H.; Hirano, M.; Kamiya, T.; Hosono, H. *Phys. Rev. B*. **2004**, *69*, 155305.

(8) Kamihara, Y.; Watanabe, T.; Hirano, M.; Hosono, H. *J. Am. Chem. Soc*. **2008**, *130*, 3296.

(9) Watanabe, T.; Yanagi, H.; Kamiya, T.; Kamihara, Y.; Hiramatsu, H.; Hirano, M.; Hosono, H. *Inorg. Chem.* **2007**, *46*, 7719.

(10) Kohama, Y.; Kamihara, Y.; Hirano, M.; Kawaji, H.; Atake, T.; Hosono, H. *Phys. Rev. B*. **2008**, *78*, 020512.

(11) Yanagi, H.; Kawamura, R.; Kamiya, T.; Kamihara, Y.; Hirano, M.; Nakamura, T.; Osawa, H.; Hosono, H. *Phys. Rev. B*. **2008**, *77*, 224431.

(12) Hiramatsu, H.; Ohta, H.; Suzuki, T.; Honjo, C.; Ikuhara, Y.; Ueda, K.; Kamiya, T.; Hirano, M.; Hosono, H. *Cryst. Growth Des.* **2004**, *4*, 301.

(13) Cullity, B.; Stock, S. *Elements of X-Ray Diffraction*; 3rd ed.; Prentice Hall, 2001.

(14) Hiramatsu, H.; Yanagi, H.; Kamiya, T.; Ueda, K.; Hirano, M.; Hosono, H. *Chem. Mater*. **2008**, *20*, 326.

(15) Ohtani, T.; Tachibana, Y.; Fujii, Y. *J. Alloys and Compd*. **1997**, *262-263*, 175.

(16) Hersh, P. A. *Ph.D. Dissertation*, Oregon State University, 2007.

(17) Kykyneshi, R.; McIntyre, D.; Tate, J.; Park, C.; Keszler, D. *Solid State Sciences*. **2008**, *10*, 921.

(18) Park, C.; Keszler, D. A.; Yanagi, H.; Tate, J. *Thin Solid Films*. **2003**, *445*, 288.

CHAPTER 5

Thin Film Preparation and Characterization of Wide–Gap Cu_3TaCh_4 (Ch = S or Se) p-type Semiconductors

P. F. Newhouse[a,b], P. A. Hersh[b], A. Zakutayev[a], A. Richard[a,b], H. A. S. Platt[b], D. A. Keszler[a,b], and J. Tate[a,b].

[a] Department of Physics, Oregon State University, 301 Weniger Hall, Corvallis, Oregon USA 97331-6507

[b] Department of Chemistry, Oregon State University, 153 Gilbert Hall, Corvallis, Oregon USA 97331-4003

A modified version of this work appears as

P. F. Newhouse, P. A. Hersh, A. Zakutayev, A. Richard, H. A. S. Platt, D. A. Keszler, J. Tate, accepted to *Thin Solid Films*.

Abstract

The structural, optical, and electronic properties of thin films of a family of wide band gap (E_g > 2.3 eV) cubic *p*-type semiconductors Cu_3TaQ_4 (Q = S or Se) are presented. Thin films prepared by pulsed laser deposition of ceramic Cu_3TaQ_4 targets and *ex-situ* annealing of the as-deposited films in chalcogenide vapor exhibit mixed polycrystalline/[100]-directed growth on amorphous SiO_2 substrates and strong (100) preferential orientation on single-crystal yttria-stabilized zirconia substrates. CTS films prepared by an alternate synthesis technique of metallic precursor sulfurization are polycrystalline. Cu_3TaS_4 (E_g = 2.75 eV) thin films are transparent over the visible spectrum while Cu_3TaSe_4 (E_g = 2.35 eV) thin films show some absorption in the blue. Thin film solid solutions of $Cu_3TaSe_{4-x}S_x$ and $Cu_3TaSe_{4-x}Te_x$ can be prepared by annealing Cu_3TaSe_4 films in a mixed chalcogenide vapor. Powders and thin films of Cu_3TaS_4 exhibit visible photoluminescence when illuminated by UV light.

Introduction

Work done at Oregon State University on the Cu_3TaCh_4 (Ch = S, Se, Te) hereafter "CTCh") system has shown that these materials exhibit several favorable optoelectronic properties including p-type conductivity, large optical band gap energy, and tunable visible photoemission (1, 2). Also, they crystallize in the cubic sulvanite (Cu_3VS_4) structure (space group *P–43m* no. 215) (3-6) and therefore are expected to show isotropic optical and electrical properties. An isotropic structure can be advantageous for process integration as special or extreme growth conditions needed to prepare epitaxial or preferred orientations can be avoided. The cubic crystal structure of Cu_3TaCh_4 makes it unique among Cu(I)-based, wide band gap *p*-type semiconductors. The better-known delafossites $CuMO_2$ (M = Al, Sc, Cr) (7-9) or the oxide and chalcogenide fluorides (10-12) LaCuOCh and BaCuChF crystallize in hexagonal or tetragonal crystal structures, respectively. The non-isotropic crystal structure of these materials requires that thin films with optimized electronic and optical properties be epitaxially grown using high temperatures and/or single crystal substrates (13). Extensive research on the delafossites and layered oxychalcogenides has been carried out over the past decade revealing many properties and applications of technological significance including degenerate p-type conductivity and room temperature excitonic emission (14-16). By contrast, the optoelectronic merit of the CTCh system has never been investigated, and the results presented here are the first ever reported thin film preparation of any members of the sulvanite class of materials we are aware of, despite a long history of power and crystal synthesis (3-6). An image

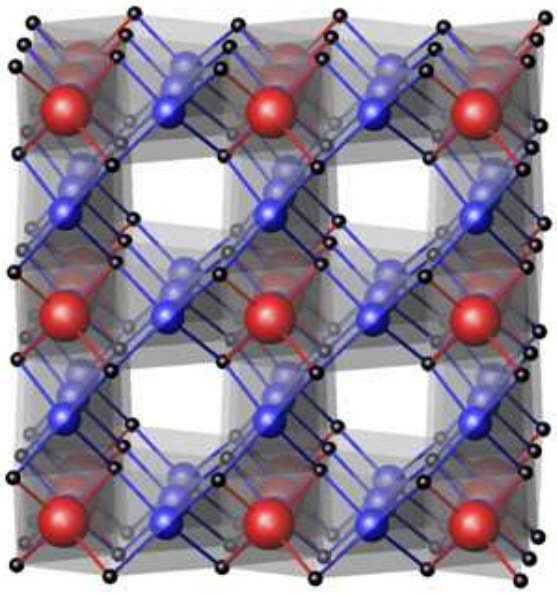

Fig. 1 Structure of Cu_3TaS_4 consisting of edge and corner shared CuS_4 tetrahedra (blue and black) and TaS_4 tetrahedra (red and black). Ta is pentavalent and four coordinate, which is quite rare. The lattice parameters in Å are CTS: 5.5036, CTSe: 5.6535, CTTe: 5.930.

of the sulvanite structure is shown in Fig. 1, consisting of edge and corner sharing $CuCh_4$ and $TaCh_4$ tetrahedra. In binary Ta chalcogenides, Ta is tetravalent, while in the CTCh structure Ta is pentavalent and four fold coordinate, which is an usual combination (17).

The large optical band gap energy of the sulfide (E_g = 2.75 eV) renders Cu_3TaS_4 (CTS) transparent to most visible light. Consequently, CTS thin films could be used in transparent electronics as p-type layers in active devices including p-n junctions, transistor channel layers, and photovoltaics. Cu_3TaSe_4 (CTSe) thin films, with a smaller band gap (E_g = 2.35 eV), may be useful in other applications where complete visible transparency is not required such as p-type absorber layers in multi-junction solar cells (18). Additionally, heteroepitaxial growth of CTCh on Si may be realized as the lattice constant match for the sulfide and selenide is quite good at 1.34% and 4.10%, respectively. Also, the visible photoluminescence (PL) properties of CTS indicate that light-emitting devices based on CTS may be realized. In particular, CTS powder exhibits intense green PL with peak intensity at 543 nm when illuminated under a UV lamp, while the selenide exhibits a PL peak at 623 nm under N_2 laser excitation (1, 19). For both compounds the wavelength of the PL can be modulated by doping W onto the Ta site, or by preparing CT(S,Se) solid solutions. W-doped CTS powder develops an additional PL peak in the red; this simultaneous red and green emission is observed as intense orange PL. Increased W-doping suppresses the green PL peak such that only a red PL peak is observed. Thus, intense green, orange, and red PL can be observed from intrinsic or W-doped CTS (1). For

the selenide, the PL is also redshifted, but a clear two-peak structure is not observed (19).

LAPW electronic structure calculations (20, 21) show that the top of the valence band in CTCh is a hybridization of Cu 3*d* and Ch 3*p* atomic orbitals, which will provide a more favorable hole transport path compared to materials in which Cu 3*d* and O 2*p* states comprise the valence band maximum (VBM), such as the delafossites (22). The calculations also indicate an indirect band gap for both sulfide and selenide compounds. In this chapter we describe the preparation of CTS, CTSe, CT(S,Se) and CT(Se,Te) thin films and their associated structural, optical, and electrical properties. We also report optical measurements of CTS single crystals prepared by chemical vapor transport.

Experiment

Two methods for CTCh thin film synthesis were developed and are presented below. Both methods involve two distinct steps consisting of thin film deposition and post-deposition *ex-situ* treatment. The first method involves the use of Cu_3TaCh_4 ceramic targets and was the preferred route for preparing high quality films. The second method involves the fabrication of Cu-Ta metal multilayer thin films and rapid sulfurization in flowing $H_2S(g)$ to form Cu_3TaS_4. The characterization results reported in this chapter, unless otherwise noted, are derived from samples prepared using the former, higher quality synthesis using ceramic targets.

CTCh Thin Films from Ceramic CTCh Targets

CTCh thin films were prepared using a two-step growth process involving pulsed laser deposition (PLD) of Cu_3TaCh_4 ceramic targets and *ex-situ* annealing of the as-deposited films in chalcogenide vapor (CVA, chalcogenide vapor anneal). *In-situ* preparation of CTCh thin films using PLD was not successful due to phase separation of the as-deposited films into binary Cu and Ta chalcogenides and/or the formation of amorphous CTCh. The phase separation could have been caused or exacerbated by the use of a chalcogen-deficient target, which is generated in the course of pellet densification at high temperatures. Thin films were deposited in a UHV chamber (base pressure 1 x 10^{-9} torr) onto heated GE 124 amorphous SiO_2 (a-SiO_2) or single-crystal (100) yttria-stabilized zirconia (YSZ) substrates using a KrF excimer laser (λ = 248 nm, τ = 25 ns) set to 10 Hz and 0.25-1 J/cm^2. The substrate temperature was maintained at ~300 °C to prevent excessive chalcogenide volatilization at higher substrate temperatures and to stabilize the film phase. The as-deposited films were reflective and dark-colored regardless of deposition parameters (see Fig. 9). The films were then annealed in evacuated fused quartz tubes containing powder of the desired phase for 1-2 h at 500-750 °C. A picture and schematic drawing of the *ex-situ* annealing process are shown in Fig. 2. The CVA films were optically transparent in the case of CTS or lightly colored but transmissive in the case of CTSe, consistent with their respective band gaps. X-ray diffraction of the annealed films revealed majority phase CTCh with mixed polycrystalline/[100]-oriented growth for samples prepared on a-SiO_2 and strong [100] growth orientation for samples

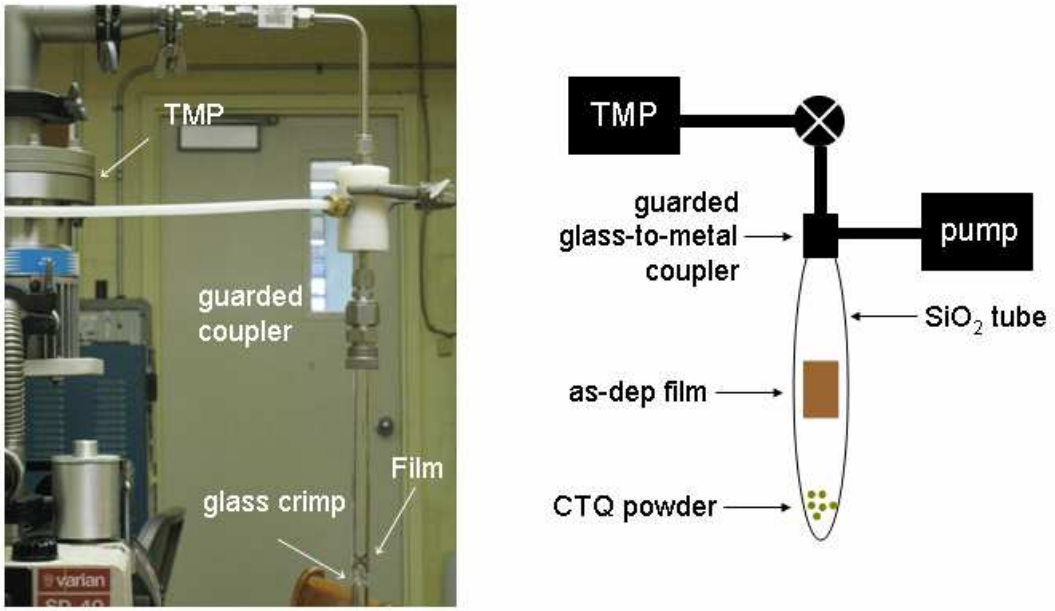

Fig. 2 Experimental and schematic images of the *ex-situ* tube sealing process. On the left, is a customized ultra-torr fitting is used to accommodate manufacturer tube diameter inconsistencies. A viton gasket in the ultra-torr fitting mates the metal and glass. This fitting is mated to a fully custom Teflon guard vacuum chamber, which creates low pressure region on the outside of the seal thereby reducing the pressure differential between the inside and outside of the tube in the region of the seal. Hence, as the seal is rotated and the glass heated with a torch, any leaks which may occur when the seal is rotated are exposed only to a low pressure, "guarded" region, rather than atmospheric pressure. Since the pressure differential is small, air leaks have little driving force to move into the tube. A ball bearing set inside the Teflon housing minimizes the amount of actual movement at the glass-viton interface, and most of the torqueing occurs at the ball bearings until the glass begins to melt and torques on itself.

prepared on YSZ.

Cu_3TaS_4 Thin Films from Diffused Cu-Ta Multilayer Precursor

Cu_3TaS_4 thin films were prepared using a two-step process consisting of the fabrication of thin stacked multilayers of metallic Cu and Ta by pulsed laser deposition and *ex-situ* rapid sulfurization of the bimetal thin film in a tube furnace under flowing H_2S and excess S powder. Films were prepared using this technique because at the time a high-density, fully sulfurized CTS ceramic target could not be prepared. The process is depicted in Fig. 3. Several reports exist on the effectiveness of Ta thin films as Cu diffusion barriers for microelectronic devices (23, 24). Hence, precursor films must be prepared such that the discrete Cu and Ta layers diffuse to form a uniformly mixed, quasi-alloy thin film. To achieve sufficient mixing, ultra thin metal layers were deposited and moderate substrate heating was used. For films prepared at 250 °C, low angle x-ray reflectivity measurements showed no superlattice periodicity, confirming that discrete layers were not present. This was not the case for films prepared at room temperature, which exhibit superlattice structure and could not be successfully sulfurized by rapid thermal processing. The precursor Cu-Ta multilayer thin films were deposited in a high vacuum chamber (base pressure 2×10^{-8} torr) onto heated a-SiO_2 or single-crystal (100) Si substrates using a KrF excimer laser (λ = 248 nm, τ = 25 ns) at 10 Hz and 6-10 J/cm^2. The large energy density values are consistent with the high ablation threshold of metals (25). A simple program was used to raster each target into the path of the beam for a set number of pulses to create

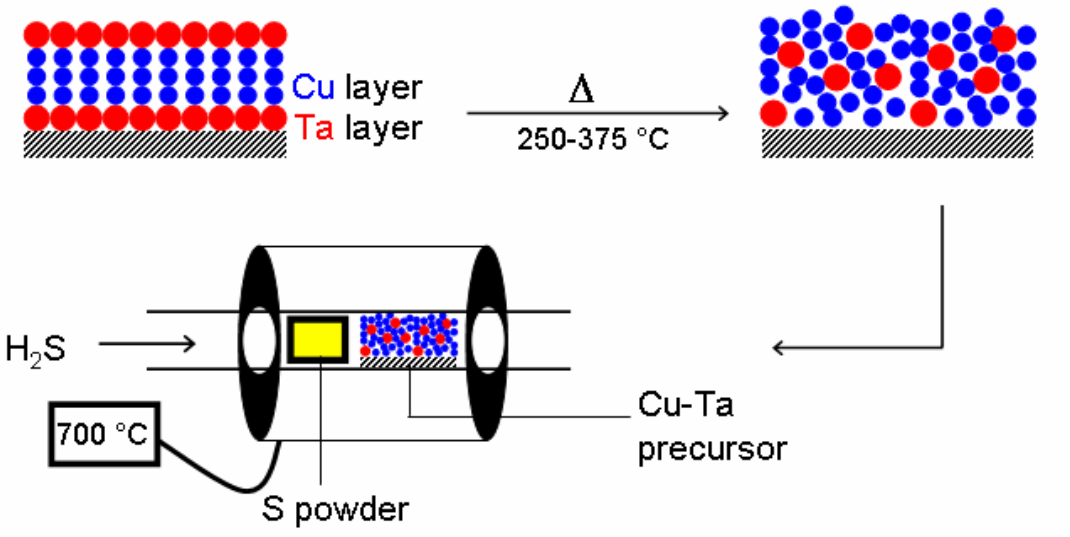

Fig. 3 Schematic of CTS thin film preparation from Cu-Ta precursor film. A stacked Cu-Ta multilayer film is prepared by PLD. With mild heating during the deposition process, the thin Cu and Ta layers interdiffuse. The diffused metal precursor is then reacted in a tube furnace under flowing H_2S to form CTS.

multilayer stacks, with pulse counts and repeat units chosen on the basis of approximate metal deposition rates and desired film stoichiometry (25). A background pressure of 1.5 mtorr Ar or 0.6-5.0 mtorr O_2 was used during each deposition. Films deposited in inert atmosphere appeared brown and shiny, while films deposited in oxygen ambient were resistive and reddish color. In the case of the oxygen-deposited films, the goal was to prepare $Cu_3TaS_{4-x}O_x$ films, which should exhibit a lager band gap than the pure sulfide. Both Ar- and O_2-deposited samples could be successfully reacted to form CTS with RTA processing, but O_2-deposited samples showed no evidence of a larger band gap. The substrate was mounted 60 mm from the targets and heated to temperatures ranging from 250-375 °C and so that the discrete Cu (~5 nm) and Ta (~1 nm) layers might interdiffuse. The Cu-Ta multilayer unit was repeated such that the multilayer total film thickness was 100-150 nm as shown by cross-sectional SEM. A best-case x-ray diffraction pattern of a CTS film produced by this method is shown in Fig. 4, indicating that films prepared by this method exhibit statistical, not preferential, crystallite orientation. In general, CTS films formed by this technique were hard to reproduce due to difficulty in controlling the metal precursor stoichiometry. An alloyed or high density pressed metal powder target with proper starting stoichiometry would be a more reliable method. Attempts were made on a pressed metal powder target with only limited success. CTSe films were not prepared by this method as H_2Se gas could not be procured.

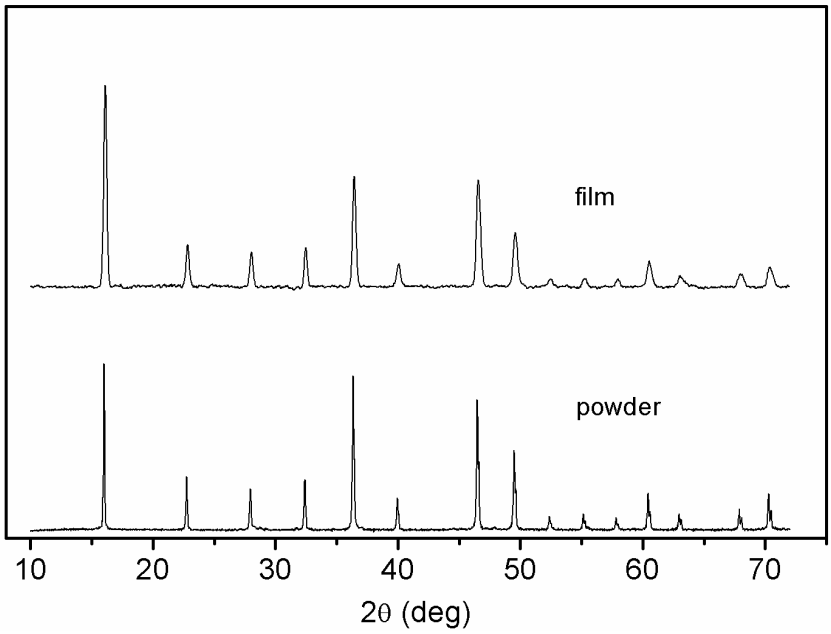

Fig. 4 The XRD patterns for a CTS film prepared from a Cu-Ta multilayer precursor and CTS powder. This synthesis method produced polycrystalline films, in contrast to films produce from ceramic targets, which exhibit significant (100) orientation even on non-crystalline substrates.

For films deposited from ceramic targets, the *ex-situ* annealing process allowed for preparation of CT(S,Se) and CT(Se,Te) solid solution thin films by annealing as-deposited CTSe films in evacuated fused quartz tubes containing 50 mg powder mixtures of CTS and CTSe or CTSe and CTTe. In the case of the CT(S,Se) solid solutions, films were heated to 625 °C for 2 h in tubes containing sulfur to selenium molar ratios of 3:1, 1:1, and 1:3. For CT(Se,Te) films, annealing was performed at 525 °C for 2 h with 3:1, 1:1 and 1:3 molar ratios of Se:Te. CTS single crystals were grown by chemical vapor transport. An evacuated fused quartz ampoule containing Cu, Ta, S, and I_2 flux was heated in a two zone furnace to 780 °C for 24 h and then cooled to room temperature, upon which the temperature gradient was reversed. The ampoule was reheated to 700 °C for 72 h and then cooled to room temperature at 10 °C/h. The ~ 1 x 1 x 0.1 mm crystals were collected and washed with deionized water to remove excess halides. CTSe single crystals of similar dimensions could not be prepared.

Thin film x-ray (Cu K_α) spectra (XRD) were taken using a Rigaku Miniflex tabletop diffractometer. Optical absorption spectra in the UV–visible range were measured using a double-monochromator grating spectrometer with W light source and a Si photodiode detector. The film thickness *d* and refractive index *n* were obtained by numerical fitting of modeled optical interference patterns to those measured. For CTS, the optical measurement results (*n* and *d*) were verified using a Metricon prism coupler to find the wavelengths of guided modes. The absorption coefficient α was calculated from the transmitted I_{trans} and reflected intensity I_{refl} using the relation $T = (1-R)e^{-\alpha d}$ where $T = I_{trans}/I_{inc}$ is the transmission coefficient,

$R = I_{refl}/I_{inc}$ is the reflection coefficient, and I_{inc} is the incident light intensity. Photoluminescence measurements were performed on CTS thin films at room temperature using a nitrogen laser excitation source (λ = 337 nm, τ = 3.5 ns) and a CCD detector.

Results and Discussion

Structural Characterization of CTCh Thin Films

The θ–2θ XRD pattern for a CTS thin film prepared on a-SiO_2 and CTS powder are shown in Fig. 5. The presence of several (*h*00) reflections and the suppression of most non-(*h*00) diffraction peaks indicate that the sample is preferentially oriented along [100] but still shows some polycrystalline character, which is manifest by weak (111) and (012) diffraction peaks. The sample also shows the presence of minority phase crystalline impurities near 31.0° and 43.9° 2θ. In general, CTCh films prepared on a-SiO_2 commonly exhibit a significant degree of [100] preferential growth with a smaller amount of polycrystalline growth. This is a significant attribute since the electronic properties of preferentially oriented films are often better than their polycrystalline counterparts. CTCh films prepared on YSZ (*a* = 5.12 Å) exhibit very strong [100] preferential growth with no or very little evidence of polycrystalline orientation despite a 7% (10%) lattice mismatch for the sulfide (selenide). In Fig. 6 the x-ray diffraction pattern from a (100) preferentially oriented CTS film on a single crystal YSZ (100) substrate and a calculated CTS powder pattern are shown. The (*h*00) reflections are labeled and substrate diffraction peaks are

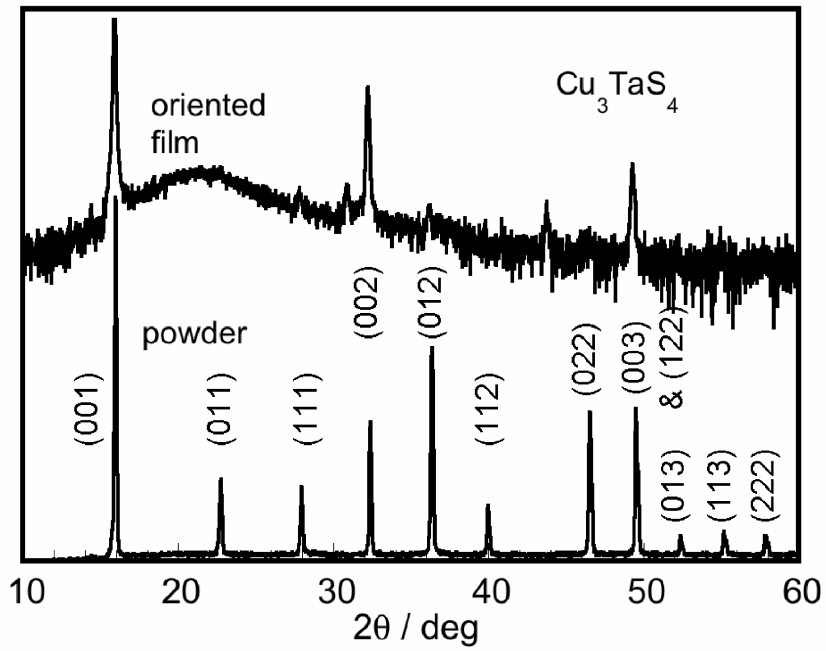

Fig. 5 The θ–2θ XRD pattern from a CTS film deposited on a-SiO_2 and annealed at 625 °C for 1h. The film patterns is plotted on a log scale and the powder pattern plotted on a linear scale. The presence of several (*h*00) diffraction peaks and suppression of most polycrystalline peaks indicates that the film is preferentially oriented along [100].

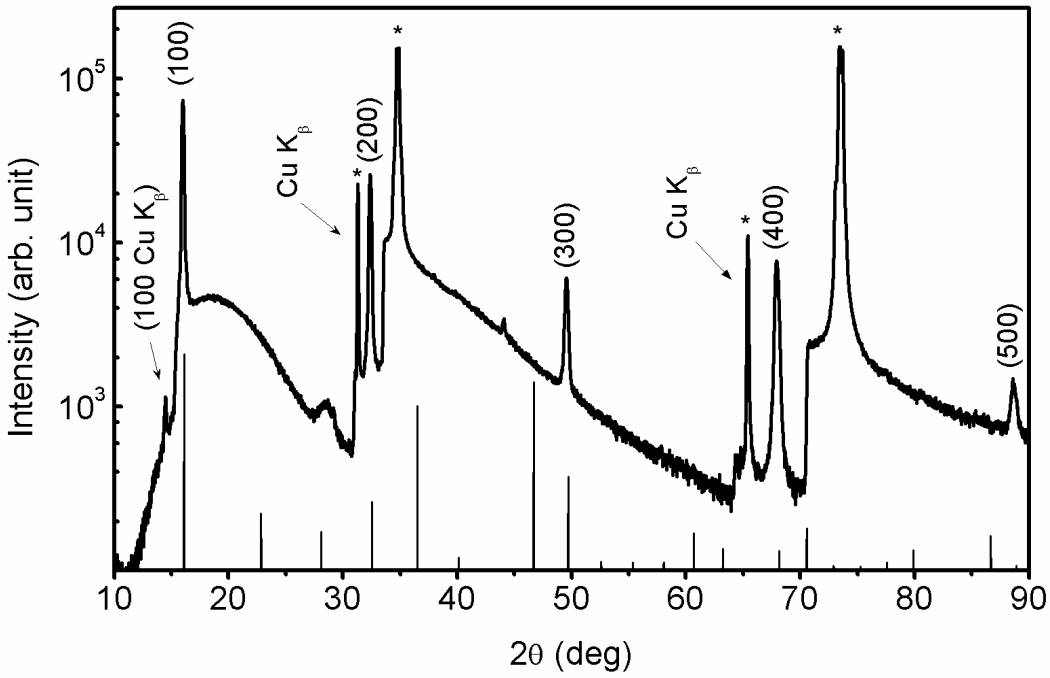

Fig. 6 The θ–2θ x-ray diffraction pattern from a CTS film prepared on YSZ (upper pane) and a calculated CTS powder pattern (lower pane). The presence of multiple (*h*00) diffraction peaks and the suppression of polycrystalline peaks of type (*hkl*) indicate that the film is preferentially oriented along [100]. Substrate peaks are indicated by an asterisk. The film and substrate exhibit significant diffracting power as even low intensity Cu K_β impurity radiation is diffracted. The film pattern sits on a large background intensity, which may result from detector saturation/re-normalization problems due to the extreme high count intensities generated by the bulk single crystal substrate and oriented thin film.

indicated by an asterisk. The diffracting power of the bulk single crystal substrate is large, and even low intensity Cu K_β radiation is diffracted by the substrate. A Cu K_β reflection near 15° 2θ can also be observed from the film (100) peak, indicating the film also has strong diffracting power and high degree of orientation. The broad peak near 29° 2θ is ascribed to Ta_2O_5, which can form if the base pressure during the tube sealing process is too high. The sensitivity of the films to residual oxygen in the tube upon heating was the impetus for the development of a guarded, high vacuum tube sealing method (see Fig. 2). Prior to the development of this method only poor quality samples could be prepared and high temperatures could not be used due to the higher tube background pressure.

$Cu_3TaCh_{4-x}Ch_x'$ Solid Solution Thin films

The *ex-situ* annealing process allowed for preparation of CT(S,Se) and CT(Se,Te) solid solution thin films by annealing as-deposited CTSe films in evacuated fused quartz tubes containing powder mixtures of CTS and CTSe or CTSe and CTTe. To verify incorporation of the substituted chalcogenide atom, the position of the (100) reflection in the thin film XRD pattern was monitored and elemental concentrations were measured using electron probe microanalysis (EPMA). The low angle (100) peak (15-16° 2θ) was chosen rather than higher angle peaks because it exhibited the highest intensity and best peak shape, which facilitated accurate peak position determination. Moreover, peaks present at higher (more accurate) angle in one film

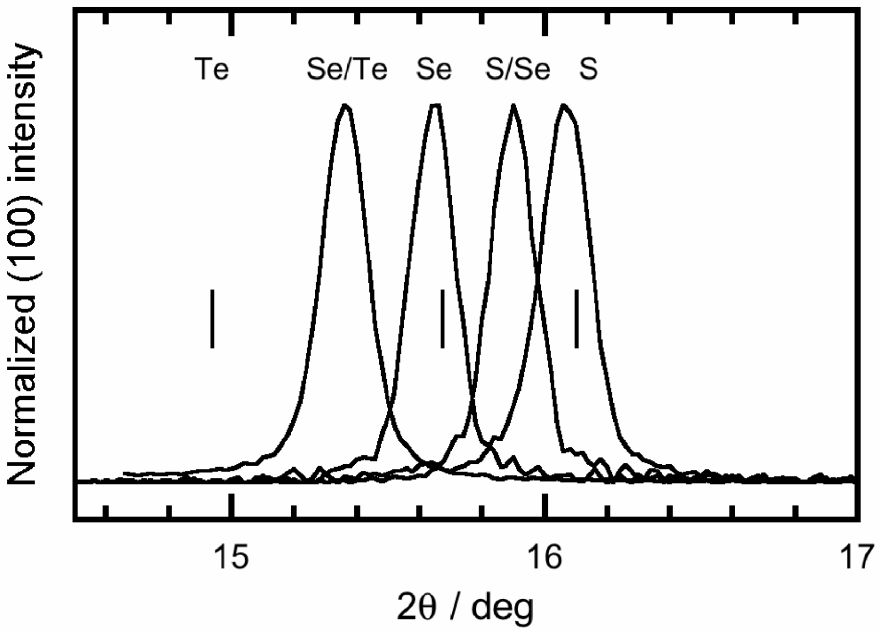

Fig. 7 The normalized (100) XRD peaks from thin films of (L to R) CT(Se,Te), CTSe, CT(S,Se), and CTS. The calculated (100) peak positions for pure CTTe, CTSe, and CTS are shown as lines. A pure phase CTTe film was not attempted.

were not necessarily present in a different film (cf. the (200) reflection of CTSe is strongly suppressed, yet strong in CTS). Fig. 7 shows the position of the normalized (100) XRD peaks for thin films of CTS, CT(S,Se), CTSe, and CT(Se,Te), which show good agreement with the angular positions predicted by Vegard's law on the basis of the measured chalcogenide ratios (Fig. 8 and Table 1). Preparation of a single phase CTTe film was not attempted although majority phase powder synthesis was achieved. Also shown as lines are the positions of the (100) peaks for CTS, CTSe, and CTTe calculated from single crystal refinement data (1, 26). In the case of the CT(S,Se) film, movement of the (100) peak to higher 2θ relative to pure CTSe is indicative of a contraction of the lattice due to substitution of Se by the smaller S, thus indicating that a CT(S,Se) solid solution thin film has been prepared. Analogous peak movement to lower 2θ was observed in the case of the CT(Se,Te) film where the larger Te substitutes for Se. These results indicate that smooth modulation of the optical and electronic properties within the CTCh family of compounds may be realized with chalcogenide solid solutions. Previous work has also shown optical band gap modulation among metal solid solutions of the $Cu_3M_{1-x}M'_xCh_4$ (M = Ta, Nb, V) family of compounds, making the sulvanite class of materials potentially quite versatile (1). Also, EPMA and XRD indicated that as-deposited CTSe films could be completely sulfurized by annealing the CTSe film in pure CTS vapor such that a $CTS_{4-x}Se_x$ with $x \sim 0.0$ could be prepared from an as-deposited CTSe film.

As verification of the lattice parameter changes predicted by Vegard's Law, the *d*-spacing [for the (100) plane, $d = a_{lattice}$] of several $Cu_3TaCh_{4-x}Ch'_x$ solid solution

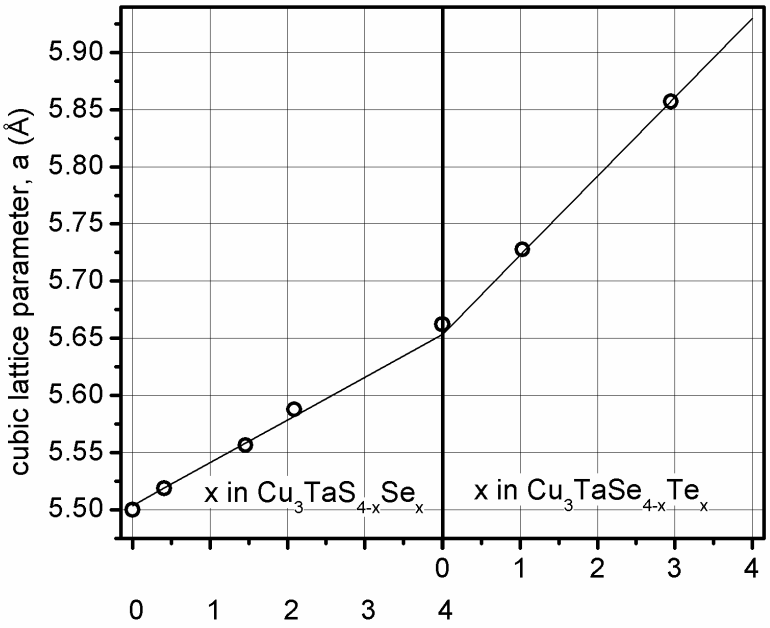

Fig. 8 The lattice parameters of several $Cu_3TaCh_{4-x}Ch'_x$ solid solution thin films plotted as a function of the molar chalcogenide concentration, *x*, as measured by EPMA (open circles). The solid connecting lines represent the lattice constants predicted by Vegard's Law.

Table 1 The molar chalcogenide concentration *x* in $Cu_3TaCh_{4-x}Ch'_x$ for solid state solution powders and thin films. EPMA was used to determine the film *x*, and the *d*-spacing calculated on the basis of Vegard's Law. Measured *d*-spacings are determined from the position of the (100) peak in the film x-ray diffraction pattern. The calculated *d*-spacing of the pure compounds are single crystal lattice refinements.

powder *x*	film *x* in $CTS_{4-x}Se_x$	d_{meas} (Å)	d_{calc} (Å)	film *x* in $CTSe_{4-x}Te_x$	d_{meas} (Å)	d_{calc} (Å)
0	--	5.4999	5.5036(4)	--	5.6622	5.6535(7)
1	0.41	5.5186	5.5190	1.03	5.7277	5.7247
2	1.46	5.5564	5.5583	--	--	--
3	2.09	5.5877	5.5819	2.95 (calc)	5.8572	5.8572
4	--	5.6622	5.6535(7)	--	--	5.930(2)

thin films are plotted as a function of the chalcogenide molar concentration, *x*, which was measured using EPMA (Fig. 8, open circles). The solid lines represent the predicted value of the lattice parameter based on Vegard's law (27). For the $x = 0$ and $x = 4$ endpoints, the single crystal lattice parameters were used. The film lattice parameters are in are close agreement with the lattice parameters predicted by Vegard's Law. The data from Fig. 8 is summarized in Table 1. Note that the chalcogenide molar ratios of the powder mixtures used for annealing the CT(S,Se) films differ from the measured film ratios. For example, a 3:1 S:Se powder mixture yields a thin film with a S:Se ratio of 3.59:0.41, indicating that at these annealing temperatures S is the favored chalcogen. However, for the CT(Se,Te) system, powder and film chalcogenide ratios are in closer agreement, perhaps due to closer vapor pressures of CTSe and CTTe.

Optical Properties

The spectral dependence of the transmission and reflection coefficients for the CTS film of Fig. 4 ($d = 200$ nm) is shown in Fig. 9. Intensity modulations in the *T* and *R* spectra as a function of wavelength are due to interference of reflections at the air-film and film-substrate interfaces. The wavelength-dependent index of refraction is plotted in the inset. From 477 nm to 852 nm *n* varies from 2.45 to 2.19. These observations are consistent with a refractive index $n = 2.30$ measured at 632.8 nm using a prism coupler. The transmission coefficient of the CTS film averaged over the visible spectrum is 55% and the reflection coefficient is 21%. This value of *T* is not

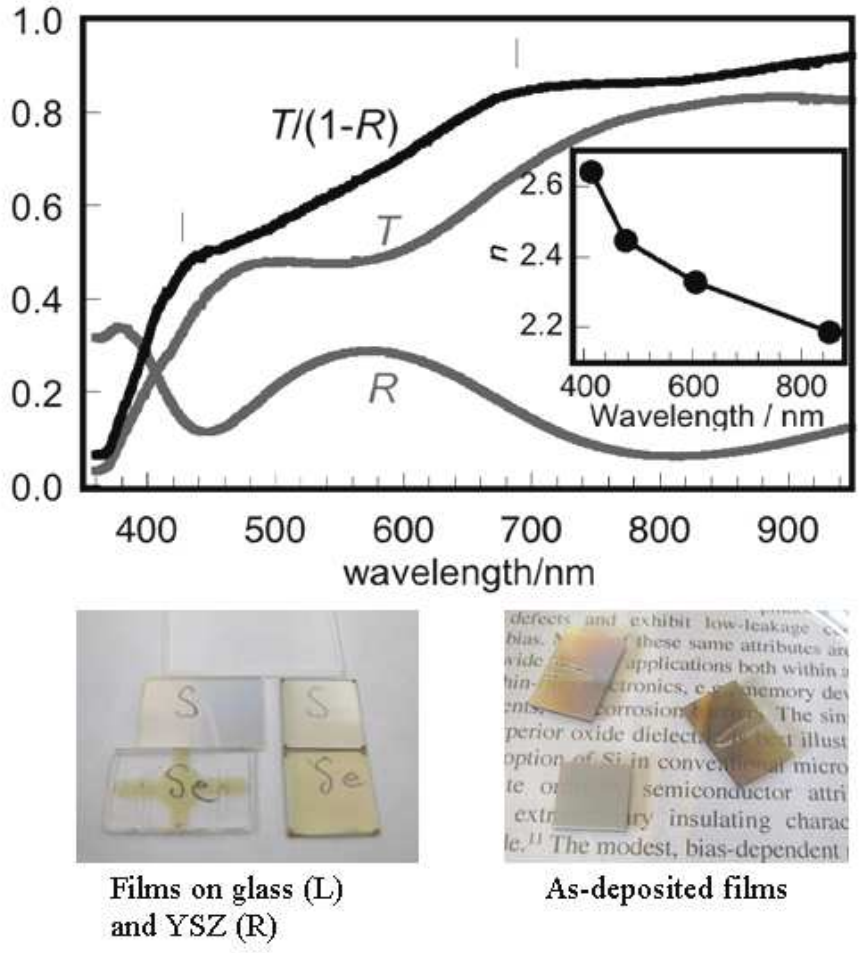

Fig. 9 The spectral dependence of the transmission T and reflection R coefficients for a 200 nm CTS film on a-SiO_2. Also plotted is $T/(1-R) = e^{-\alpha d}$, from which the absorption coefficient may be obtained. The inset shows the wavelength-dependent refractive index for this film. Below, images of crystalline CTS and CTSe films on glass and YSZ after CVA and a piece of blank glass for reference. Also shown are the as-deposited films, which are dark and amorphous.

very large, but thinner films of ~100 nm show larger transmission coefficients of 65-70% raw *T* over the visible range. The reflection-corrected transmission spectrum $T/(1-R) \approx e^{-\alpha d}$ provides a measure of the absorption coefficient. The rapid absorption change near 360 nm signals the band gap, while the intermediate absorption over 450-700 nm (indicated by vertical bars) may be related to the PL absorption. CTSe thin films exhibit similar spectra but show a delay in the onset of transmission compared to CTS due to the lower band gap energy. The large indices of refraction, which also extend into the near IR, may make CTCh a useful element of a dielectric mirror. Also in shown Fig. 9 are images of as-deposited and CVA-treated CTCh films. The as-deposited films are very dark and amorphous, while the annealed films are crystalline and transparent. A blank pieces of glass is shown for a reference.

Electronic structure calculations show that materials of the group Cu_3TaCh_4 have indirect band gaps (20, 21). Formally, the band gap energy for an indirect-gap material is found by plotting the product $(\alpha E)^{1/2}$ *vs. E* and extrapolating the linear portion of this curve to the energy axis. The result of this analysis for a CTS thin film is shown in Fig. 10 in which the extrapolated band gap energy is ~2.7 eV, in good agreement with the spectral position of the fundamental onset of absorption for a CTS single crystal located at 2.72 eV. The broad sub-bandgap absorption in the CTS film absorption spectrum of Fig. 10 may be caused by defect states in the band gap, which could also account for the observed PL. The position of this feature is roughly consistent with the PL peak at 543 nm measured from CTS powder and a thin film, shown in Fig. 11. The PL from CTS powder is intense and easily visible to the

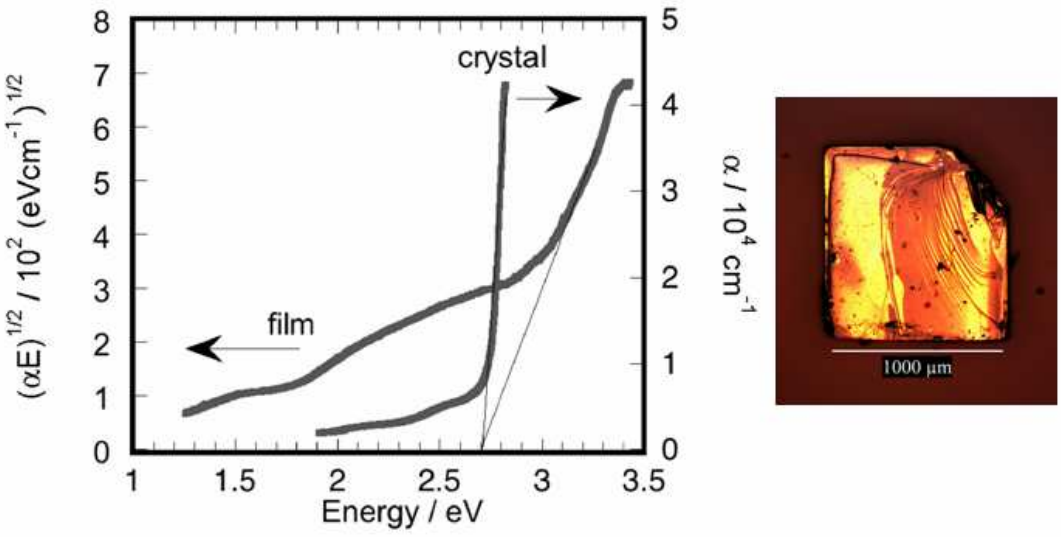

Fig. 10 $(\alpha E)^{1/2}$ *vs. E* indirect band gap analysis for a CTS film on a-SiO_2. The extrapolated film band gap of 2.7 eV agrees well with the position of the fundamental optical absorption at 2.72 eV for a CTS single crystal. An image of a CTS single crystal is shown at right. When viewed in transmission, the crystal appears light yellow.

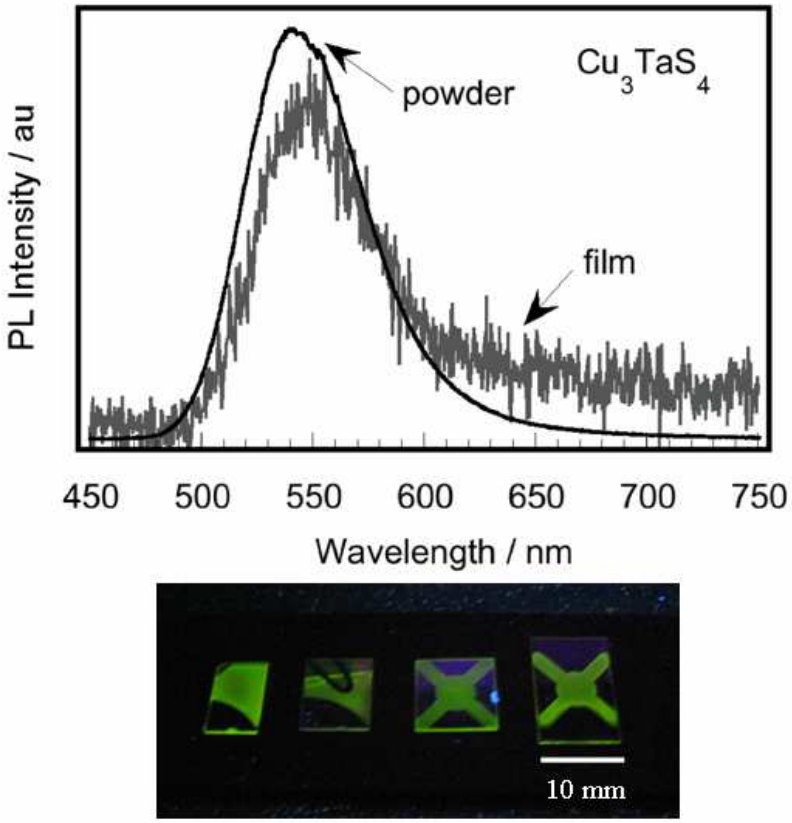

Fig. 11 CTS powder and thin film photoluminescence spectra. The film spectrum was obtained from a film with no apparent photoluminescence when viewed under a UV lamp. Some films were brightly luminescent (below) depending on the annealing conditions. Preliminary indications are that brighter luminescence correlated with lower tube sealing pressures afforded by the guarded manifold of Fig. 2.

eye, while the CTS film PL is much weaker. This film had no apparent PL when viewed under UV light, although some films emit brightly, as show in Fig. 11. A preliminary explanation correlates increased PL brightness with lower tube sealing pressures, possibly due to fewer impurities. CTSe powder shows a PL peak at 623 nm, but a simple UV lamp is not a sufficient excitation source so a nitrogen laser was used.

Previous measurements have shown that a direct correlation exists between the Cu vacancy concentration (V_{Cu}) of CTS and the PL intensity (1). Cu-deficient $Cu_{3-x}TaS_4$ (x = 0.0-0.1) powder revealed heightened PL intensity relative to stoichiometric CTS powder, indicating that the V_{Cu} concentration plays a key role in the PL mechanism. In Cu(I) containing compounds like LaCuOSe, V_{Cu} states are acceptor states, usually located just above the VBM. Excitation spectra of CTS powder revealed no detectable PL until $E_{excite} \geq E_g$, indicating that the emission of light requires band gap absorption. These data in conjunction with band gap measurements of single crystals can be combined to form a simple model of the PL mechanism in CTS in which band gap absorption is followed by decay to a V_{Cu} state (Fig. 12). As such, the model indicates that the V_{Cu} level (the acceptor level) is over 0.4 eV above the VBM and out of room temperature energy range. Hence, CTS should be an electronic insulator at room temperature. However, the model does not consider non-radiative/infrared emission which may take place from the CBM to some other state in the band gap, followed by radiative decay. This would have the effect of reducing the energy of the V_{Cu} state. Nonetheless, this provides a reasonable, first order

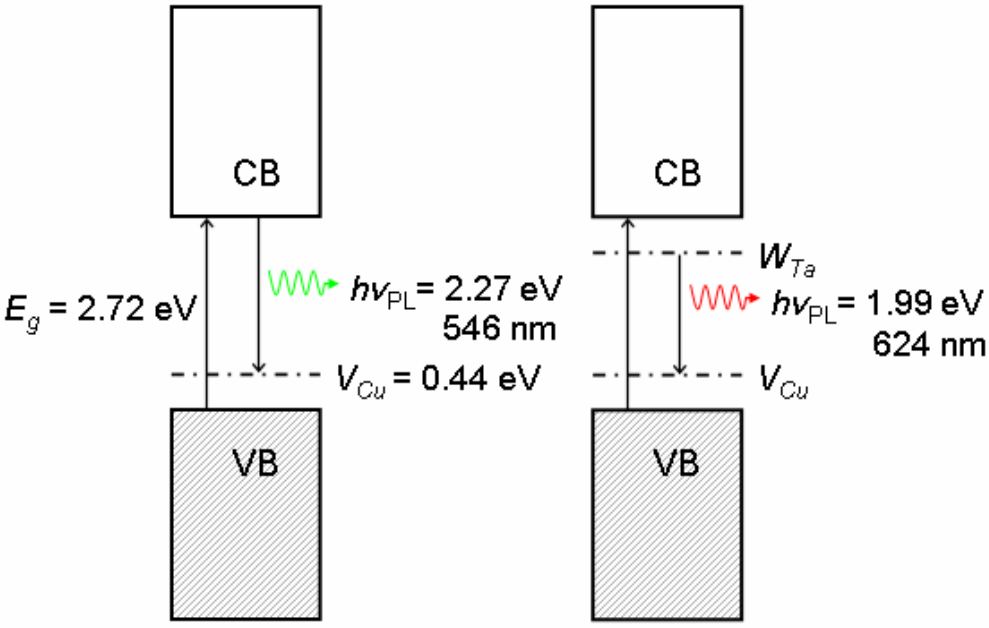

Fig. 12 Possible PL mechanism for CTS based on experimental data for the band gap and PL emission energy. This model assumes that the decay occurs from the conduction band minimum, thereby placing the V_{Cu} level at 0.44 eV

explanation for the insulating nature of these compounds. Fig. 12 also shows a possible PL mechanism for W-doped CTS, in which a W donor state is created just below the conduction band. Donor state doping is expected from W^{6+} substitution of Ta^{5+}. This model accounts for the redshifted PL observed from CTS:W.

Electronic Properties

Seebeck coefficients measured at room temperature from sintered pellets of CTS and CTSe indicate p-type conductivity in both compounds, with values of +27 μV/K for the sulfide and +24 μV/K for the selenide. Modulation of the conductivity in CTCh pellets was achieved by doping Zr (increased σ) or W (decreased σ) into CTCh (1). However, all pure/majority phase CTCh thin films prepared by the two-step PLD/CVA process were electrically insulating following the CVA, as shown by a simple ohmmeter test of the as-annealed films. But, if the films or crystals were directly heated in air on a hot plate at 150-200 °C for 0.5-2 min both became conducting no matter how they were contacted (i.e. gold paste or stainless steel). Preliminary evidence suggests that the induced conductivity may correlate with the formation of an impurity phase, detectable with XRD from films on a-SiO_2, but more work is needed for an authoritative conclusion. Given this, we measured the Hall effect from the (00*l*) aligned CTS film in Fig. 6 and found unambiguous p-type conduction with mobility of 0.8 cm^2/Vs, hole density 2.9 x 10^{20} cm^{-3}, and resistivity of 27 mOhm cm (= 37 S/cm) with no detectable XRD impurity after the hot plate anneal. Note, however, that the high intensity substrate background makes impurity detection

difficult, unlike films on vitreous substrates. The anomalous conduction properties of the film system may be related to the known ionic conduction properties of closely related Cu_3VS_4 (sulvanite) in which Cu+ ions are very mobile (28). Also, its likely that the sintering of the pellets caused significant loss of one or more elements (most likely the lower vapor pressure chalcogenide), given their dark grey, semi-lustrous appearance. This could have influenced the conductivity of the specimens. Powders synthesized in a sealed tube showed color indicative of a wide band gap (i.e. beige CTS and true brown CTSe) and should not be chalcogenide-deficient.

For films prepared on a-SiO_2, optical and electron microscopy revealed the presence of extensive microcracking on the film surface after CVA, which may be due to significant differences in the thermal expansion coefficients of the CTS film and the a-SiO_2 substrate (Fig. 13). Films prepared on YSZ and Si wafers did not show obvious microcracking following CVA. It is unclear if the observed top-down microcracking extends downward to the film-substrate interface, possibly increasing the resistance, but cross sectional SEM images did not reveal clear evidence of such behavior (Fig. 13). However, the cross sectional SEM does indicate that the film is highly dense. Interestingly, even microcracked films could be made conducting with a hot plate anneal, but their Hall effect properties were unreliable. Top-down images of CTS films prepared on a-SiO_2 are shown in Fig. 13 in which the microcracking is clearly observable.

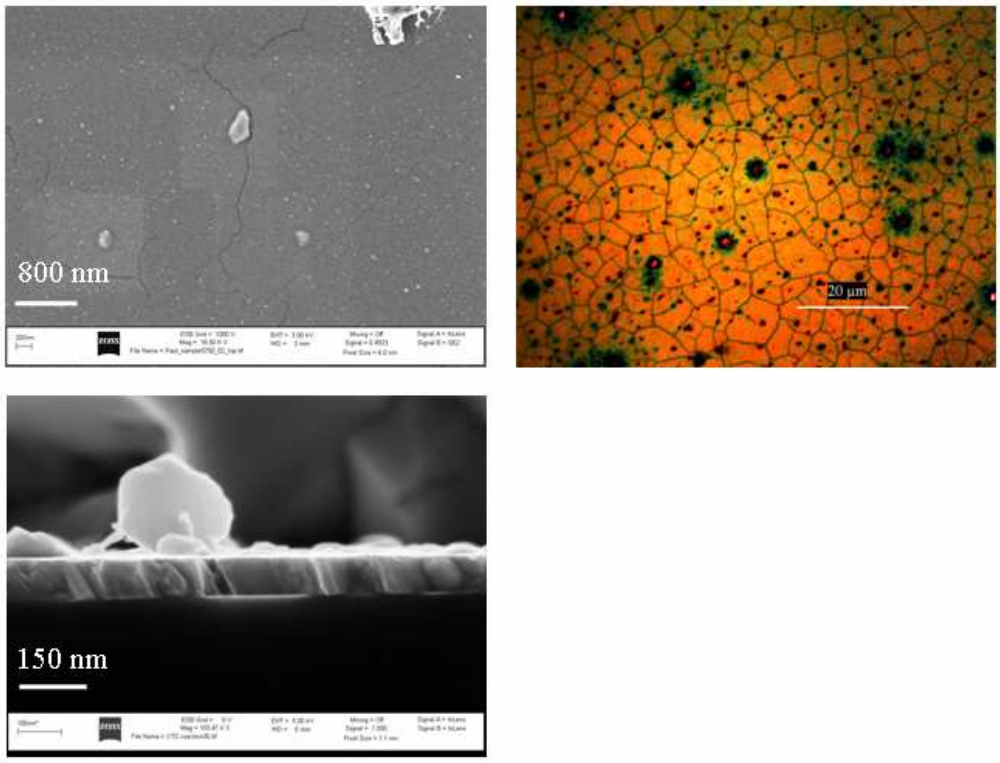

Fig. 13 Optical and electron micrographs of CTS on a-SiO_2 exhibiting microcracks.

Zr-doped Cu_3TaS_4

In order to test the apparent insulating nature of the CTCh film system, two methods of doping were attempted. Previous work on sintered CTCh pellets indicated that substituting Zr^{4+} on the Ta^{5+} site is a suitable method of hole doping (1). In the first method CVA doping was attempted by heating undoped, as-deposited CTS films with CTS:Zr powder. If successful, annealing the film at 625 °C in the presence of CTS:Zr powder would create a partial pressure of CTS:Zr(g) or a binary Zr-S(g) compound which could be incorporated into the film. However, both undoped and purportedly Zr-doped films (we say purportedly because we do not know if doping by CVA actually transports dopant atoms) were electrically insulating despite majority phase XRD patterns. In the second method, films were prepared using a $Cu_3Ta_{0.9}Zr_{0.1}S_4$ sintered pellet as the ablation source and $Cu_3Ta_{0.95}Zr_{0.5}S_4$ CVA powder (10% doped powder was not available). This film showed a majority phase XRD pattern, but was also electrically insulating. In both doping methods, EPMA should be used to determine if Zr was transported into the films. If successful, dopant transport by CVA would be a significant result. CVA doping was also attempted with other, more volatile elements including P and In but the samples remained insulating. However, in these cases it is unclear if the more volatile element was even incorporated into the powder as a dopant. More work is needed to clarify the thin film dopability of these systems and cation and anion CVA doing should be further investigated.

Cu_3TaCh_4 Electronic Structure

The electronic structure of Cu_3TaCh_4 (Ch = S, Se, Te) materials was calculated using Wien 2k (20). The total DOS for CTS is shown in Fig. 14, and a zoomed-in view of the total DOS near the band edges for all three compounds is shown in the inset. Note that the band gap energies follow CTTe < CTSe < CTS, in agreement with experiment. The calculated gaps are significantly smaller than the experimental values, this being a well-known shortcoming of the LAPW method. The PDOS results also indicate that the VBM is composed mainly of Cu 3*d* and S 3*p* states. The CBM is formed primarily from Ta 5*d* and S 3*p* states, with almost no Cu 4*s* contribution near the CBM, in contrast to similar wide gap, Cu(I) compounds like LaCuOSe in which Cu 4*s* orbital are a significant constituent of the CBM (29). The selenide and telluride compounds exhibit nearly identical features, but with the appropriate contraction of the band gap energy. The band structure of CTSe is shown in Fig. 15. The band gap is indirect, with VBM at R and the CBM at X. The band structures of CTS and CTTe are similar, but exhibit increased or decreased band curvature relative to the selenide depending on the size of the chalcogen.

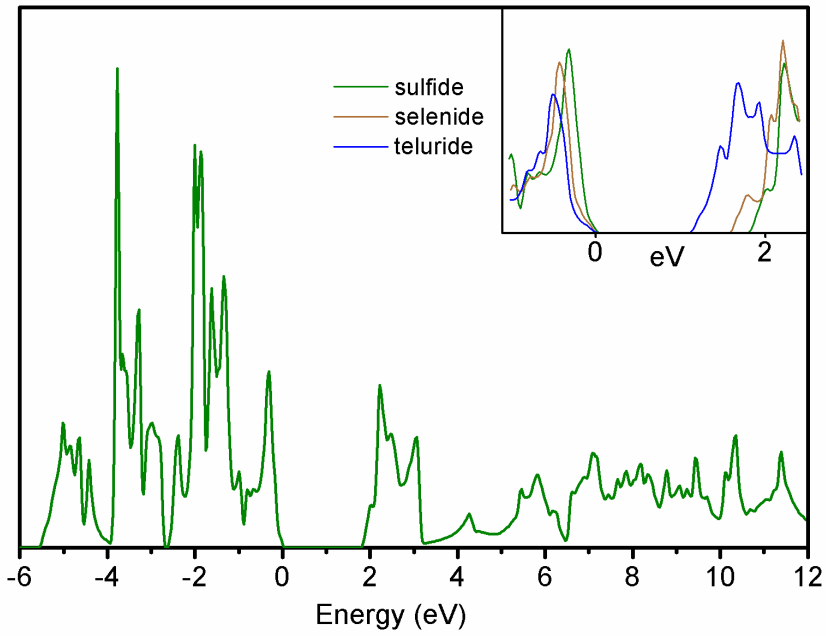

Fig. 14 Total density of states for CTS. The calculated gap is 1.81 eV. The inset shows a zoomed-in view of the total DOS for the sulfide, selenide, and telluride showing the observed trend in band gap energy.

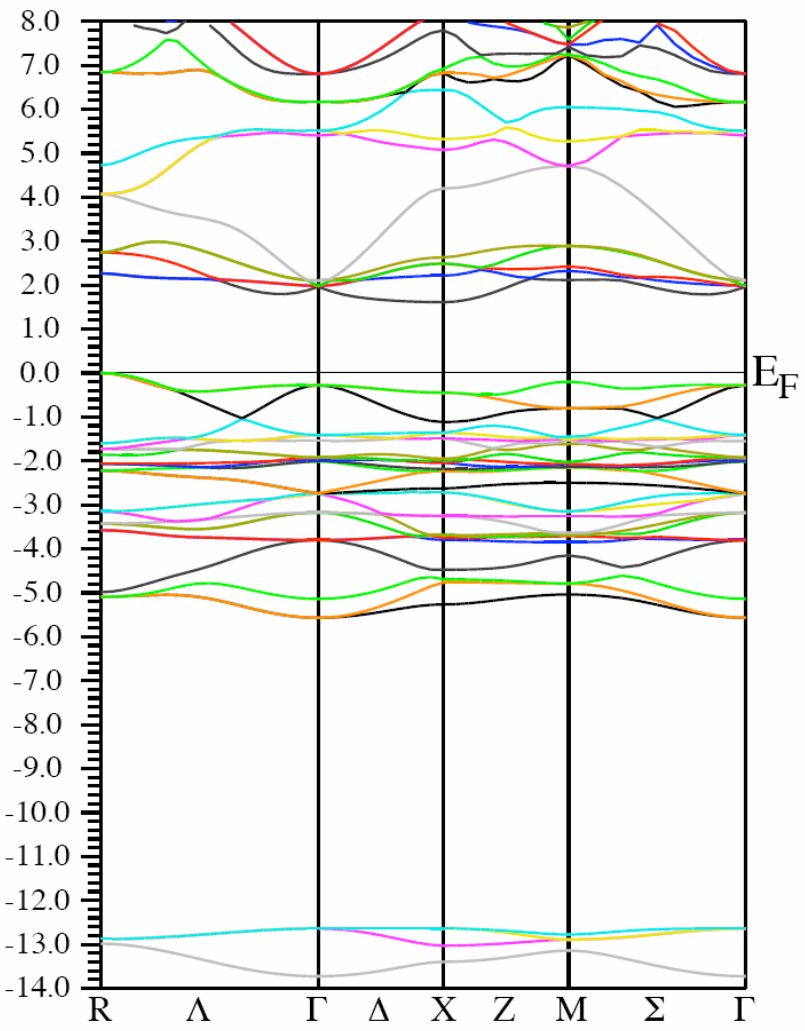

Fig. 15 LAPW band structure for CTSe. The VBM is located at R and the CBM is located at X. CTS and CTTe show similar structures.

Conclusions

Cu_3TaCh_4 and $Cu_3Ta(Ch,Ch')_4$ solid solution thin films have been using a two-step growth procedure involving PLD and *ex-situ* annealing in chalcogenide vapor. An alternate polycrystalline CTS film synthesis method involving the fabrication of stacked Cu-Ta multilayers and rapid heating in flowing $H_2S(g)$ has also been presented. Films prepared on a-SiO_2 and YSZ exhibit (100) preferential orientation and are transparent over the visible spectrum when Ch = S and lightly colored when Ch = Se. Optical absorption measurements of CTS single crystals reveal a band gap energy of 2.72 eV, while diffuse reflectance measurements of CTSe powder show a band gap of 2.35 eV. Solid state solution thin films show *d*-spacing changes in good agreement with Vegard's Law. CTS powder exhibits intense, visible photoluminescence (λ_{max} = 543 nm) when illuminated by a UV lamp, while the selenide shows a weaker, red shifted PL peak at 623 nm. CTCh films are electrically insulating unless they are heated on a hot plate in air for 0.5-2 min at 150-200 °C. For a (00*l*)-aligned CTS film on YSZ, the electronic properties measured after air heating are hole mobility of 0.8 cm^2/Vs, hole density of 2.9 x 10^{20} cm^{-3}, and resistivity of 27 mOhm cm (=37 S/cm). After CVA, CTCh films on a-SiO_2 exhibit surface microcracking, while films on YSZ do not. Undoped pellets exhibit p-type conduction and conductivity modulation capability from Zr and W-doping. Electronic structure calculations show that the VBM is composed of Cu 3*d* and Ch 3*p* states while the CBM is primarily Ta 5*d* and Ch 3*p* states. The calculated band gap indicates that the transition is indirect. The optoelectronic properties CTCh compounds and their

isotropic crystal structure indicate that these materials could be applied in a variety of transparent electronic and photovoltaic applications.

Acknowledgements

This work was supported by the National Science Foundation DMR 0245386. PFN acknowledges support from an NSF IGERT (DGE 0549503) and mechanical support from Ted Hinke. We thank Jason Stowers and Kurt Langworthy for assistance with SEM images.

References

(1) Hersh, P. A. *Ph.D. Dissertation*, Oregon State University, 2007.

(2) Newhouse, P. F.; Hersh, P. A.; Zakutayev, A.; Platt, H. A. S.; Richard, A.; Keszler, D. A.; Tate, J. *Accepted to Thin Solid Films*. **2008**.

(3) Pauling, L.; Hultgren, R. *Z. Kristallogr. A.* **1933**, *84*, 204.

(4) Trojer, F. *Am. Mineral.* **1966**, *51*, 890.

(5) Hulliger, V. F. *Hel. Phys. Acta*. **1961**, *34*, 379.

(6) Delgado, G. E.; Mora, A. J.; Duran, S.; Munoz, M.; Grima-Gallardo, P. *J. Alloys Compd.* **2007**, *439*, 346.

(7) Hahn, H.; Lorent, C. D. *Z. Anorg. Allg. Chem.* **1955**, *279*, 281.

(8) Kohler, B. U.; Jansen, M. *Z. Anorg. Allg. Chem.* **1986**, *543*, 73.

(9) Crottaz, O.; Kubel, F.; Schmid, H. *J. Sol. State. Chem.* **1996**, *122*, 247.

(10) Palazzi, M. *Acad. Sci. Paris*. **1981**, *292*, 789.

(11) Zhu, W.; Huang, Y.; Wu, F.; Dong, C.; Chen, H.; Zhao, Z. *J. Solid State Chem.* **1994**, *29*, 505.

(12) Ueda, K.; Hosono, H. *Thin Solid Films*. **2002**, *411*, 115.

(13) Hiramatsu, H.; Ohta, H.; Suzuki, T.; Honjo, C.; Ikuhara, Y.; Ueda, K.; Kamiya, T.; Hirano, M.; Hosono, H. *Cryst. Growth Des.* **2004**, *4*, 301.

(14) Hiramatsu, H.; Ueda, K.; Ohta, H.; Hirano, M.; Kamiya, T.; Hosono, H. *Thin Solid Films*. **2003**, *445*, 304.

(15) Hiramatsu, H.; Ueda, K.; Ohta, H.; Hirano, M.; Kikuchi, M.; Yanagi, H.; Kamiya, T.; Hosono, H. *Appl. Phys. Lett.* **2007**, *91*, 012104.

(16) Hiramatsu, H.; Ueda, K.; Takafuji, K.; Ohta, H.; Hirano, M.; Kamiya, T.; Hosono, H. *J. Appl. Phys.* **2003**, *94*, 5805.

(17) Keszler, D. A. *private communication*.

(18) Dimroth, F.; Kurtz, S. *Mat. Res. Soc. Bull.* **2007**, *32*.

(19) Zakutayev, A. *unpublished*. **2008**.

(20) Tate, J. *unpublished*. **2008**.

(21) Garcia, W.; Aramburo, A.; Guillen, J. *Revista Colombiana de Fsica*. **2008**, *40*, 36.

(22) Kawazoe, H.; Yanagi, H.; Ueda, K.; Hosono, H. *Mat. Res. Soc. Bull.* **2000**, *25*, 28.

(23) Clevenger, L. A.; Bojarczuk, N. A.; Holloway, K.; Harper, J. M. E.; Cabral, J.; Schad, R. G.; Cardone, F.; Stolt, L. *J. Appl. Phys.* **1993**, *73*, 300.

(24) Laurila, T.; Zeng, K.; Kivilahti, J. K.; Molarius, J.; Suni, I. *J. Appl. Phys.* **2000**, *88*, 3377.

(25) Chrisey, D. B.; Hubler, G. K. *Pulsed Laser Deposition of Thin Films*; 1st ed.; Wiley-Interscience, 1994.

(26) Li, J.; Guo, H.; Proserpio, D. M.; Sironi, A. *J. Sol. State. Chem.* **1995**, *117*, 247.

(27) Denton, A. R.; Ashcroft, N. W. *Phys. Rev. A.* **1991**, *43*, 3161.

(28) Arribart, H.; Sapoval, B.; Gorochov, O.; LeNagard, N. *Solid State Commun*. 1978, 26, 435.

(29) Hiramatsu, H.; Yanagi, H.; Kamiya, T.; Ueda, K.; Hirano, M.; Hosono, H. *Chem. Mater*. **2008**, *20*, 326.

Thin Film Preparation and Characterization of $BaBiO_3$

P. F. Newhouse[a,b], P. A. Hersh[b], J. Stowers[b], D. A. Keszler[a,b], and J. Tate[a,b].

[a] Department of Physics, Oregon State University, 301 Weniger Hall, Corvallis, Oregon USA 97331-6507

[b] Department of Chemistry, Oregon State University, 153 Gilbert Hall, Corvallis, Oregon USA 97331-4003

Abstract

Thin films of $BaBiO_3$ and $Ba_{1-x}K_xBiO_3$ have been prepared on vitreous SiO_2 and single crystal MgO (001) substrates using pulsed laser ablation of ceramic $Ba_{1-x}K_xBiO_3$ (x = 0, 0.1, 0.4) targets. Measurements of the film composition reveal that $BaBiO_3$:K films are K-deficient with respect to the target nominal K concentration by as much as half. Films deposited onto glass substrates show polycrystalline orientation, while films on MgO (100) exhibit strong [100]-directed growth. Seebeck coefficient and resistivity measurements of a sintered $BaBiO_3$ pellet reveal p-type conduction (+465 μV/K) and ρ = 2.2 kOhm cm, respectively. Undoped and K-doped films with x_{film} = 0.06-0.07 were electrically insulating, while a film with x = 0.17 showed 15 Ohm cm. UV–vis transmission spectra of BBO films exhibit a broad onset of transmission near 650 nm (=1.91 eV) ascribed to the fundamental bad gap and a peak near 420 nm (=2.95 eV) ascribed to intervalent charge transfer, imparting a violet-blue appearance when viewed in transmission. Occasional microcracking of the $BaBiO_3$ film surface was observed for films on SiO_2 and MgO, which could be due to oxidative shrinkage.

Introduction

The discovery of high temperature superconductivity in $BaPb_{1-x}Bi_xO_3$ by Sleight in 1975 and began a vigorous and continuing research effort into the family of compounds based on the distorted perovskite $BaBiO_3$ (BBO) (1). Later, more interest was generated when it was found that samples which were heavily K doped, viz. $Ba_{1-x}K_xBiO_3$ (BKBO), also showed superconductivity with maximum T_c = 30 K at x = 0.4 (2). Excitement over these materials stemmed from the fact that these compounds were the first non-cuprates to exhibit such high transition temperatures and might provide clues to elucidate the mechanism of superconductivity. More recently, BBO has generated interest as a strong photocatalytic material which oxidizes organic compounds in the presence of visible light (3, 4). From a more fundamental vantage point, the parent compound BBO has been studied as the foremost example of Bi charge disproportionation (5, 6). In BBO the formal valence of Bi is +4, and on this basis BBO is predicted to be metallic due to its half-filled $6s^1$ band (6). However, this is not observed experimentally, and BBO is found to be a semiconductor with $E_g \sim 2$ eV. Rather than containing a single tetravalent Bi, the compound can be expressed as $Ba_2Bi^{3+}Bi^{5+}O_6$ in which the Bi atoms have disproportionated into their preferred 3+ and 5+ valence states giving rise to an ordered array of charge fluctuation, a so-called charge density wave. Structurally, this is manifested as two distinctly different Bi–O distances which result in alternately expanded and contracted BiO_6 octahedra (5, 7). This can be envisioned as a frozen breathing-mode type displacement of the BiO_6 octahedra. The band gap is opened up between filled Bi^{3+} valence band states and empty Bi^{5+} conduction band states. Thus

the VB configuration in BBO should be Bi $6s^2$ and a good starting point for the development of p-type transparent conducting oxide (TCO) since holes created in the *s*-type VB should have high mobility (8). This presumes that the Bi 6*s* level lie above the O 2*p* level in the VB. This is not the case in Bi_2O_3 (O 2*p* lies above Bi 6*s*) and for BBO this has been a point of controversy and conflicting results, which photoemission experiments and DFT calculations have tried to resolve (6, 9). Our interest in BBO began from the possibility of the ns^2-type VB, even though the band gap is too small for use as a TCO. Nonetheless, the gap might be engineered in such a way as to preserve the VB character and increase the visible transparency. In particular, Ce-doping of Bi has revealed the possibility of band gap widening with a trade off with increased resistivity (10). Thus one may envision a p-type TCO evolving from hole-doped $Ba_{1-x}K_xBi_{1-y}Ce_yO_3$. In this chapter we present our results of thin film preparation and characterization of BBO and K-doped BBO (BKBO). Our results show that BBO remains electronically insulating when K concentration is low and becomes conducting when $x \sim 0.2$. Also, we present the results of thin film electron microprobe measurements which show that a large portion of K is lost during the deposition and/or the target sintering process. In Figs. 1 and 2 we present our results of x-ray diffraction measurements of BBO films on vitreous and crystalline substrates. We also outline a method to produce high quality BKBO films using oriented template and passivation layers. Finally, in Fig. 5, an optical micrograph of a severely microcracked BBO film on MgO is shown and discussed on the basis of oxidation-induced cracking.

Experiment

Thin films of $BaBiO_3$ were deposited onto heated amorphous SiO_2 (a-SiO_2) and single crystal MgO (001) substrates using pulsed laser ablation of ceramic $BaBiO_3$ and $Ba_{1-x}K_xBiO_3$ targets in a high vacuum chamber. For target preparation, powders were first synthesized using stochiometric quantities of $BaCO_3$ and Bi_2O_3, thoroughly mixed and heated in air at 900 °C for 24 h. This was followed by cold pressing at 1.5 tons and air sintering at 850 °C. The resulting target was brown and 85% dense. K-doped targets were prepared in the same manner, with K_2CO_3 and reaction and sintering temperatures of 800 °C and 750 °C, respectively. Volatilization of K during pellet sintering was suspected based on the appearance of the targets, which were darker than the undoped target with a glossy finish around the edges. The density was not quite as high as the undoped target (60-70%), and the K-doped targets were moderately or strongly hydroscopic depending on the doping level. Films were deposited in 100 mtorr of grade 4.7 O_2 using a Lambda Physik Compex 201 excimer laser (λ = 248 nm, τ = 25 ns) set to 10 Hz and 1.5-2 J/cm^2. The targets ablated easily due to the high absorbance of the targets. The preparation of BKBO films on MgO consisted of two sequential steps *in-situ* beginning with (*i*) deposition of a thin, undoped BBO template layer at high temperature and (*ii*) deposition of K-doped film at lower temperature to avoid excessive K volatilization. The target was positioned 50 mm from the substrate, which was heated to 375-450 °C. Room temperature depositions were also performed, but such films were optically transparent and insulating, most likely consisting of amorphous binary oxides of Ba

and Bi. Films were cooled in the deposition ambient, or annealed at deposition temperature in 760 torr O_2 for 1 h.

Films were characterized by fixed incidence and θ–2θ x-ray diffraction (XRD), electrical conductivity, variable field Hall effect transport measurements, UV–vis transmission and reflection, and by electron probe microanalysis (EPMA). Fixed incident angle XRD spectra (Cu K_α) were measured using a Rigaku Rapid R-axis diffractometer while a Rigaku Miniflex tabletop diffractometer was used to acquire θ–2θ patterns. For measurements using the Rapid R-axis diffractometer a two-dimensional area detection screen allowed reflections from a range of 2θ and χ angles to be acquired simultaneously. Electrical conductivity from pellets and thin films was measured at room temperature in the van der Pauw configuration on a Lakeshore 7504 Hall measurement system. For measurements of pellet electrical properties, Ag contacts were deposited using PLD at room temperature in 100 mtorr of N_2. Optical transmission and reflection spectra in the UV–visible range were measured using a double grating spectrometer coupled to a Xe light source and a Si diode detector. Seebeck measurements were performed at room temperature on an in-house designed system consisting of a Keithley 195A digital multimeter and a Tektronix DM 5120 digital multimeter. EPMA was performed using a Cameca SX50 electron microprobe using multivoltage thin film analysis.

Results and Discussion

Structural Characterization of $BaBiO_3$ Thin Films

The XRD patterns from undoped BBO powder and a thin film are shown in Fig 1. The film deposited in 100 mtorr O_2 on vitreous SiO_2 at 400 °C is pure phase and exhibits statistical orientation, which is easily noted from the close match in peak intensity ratios from the powder and film. The XRD patterns from polycrystalline BKBO films appear identical to undoped films, with a slight peak shift to higher angle (smaller *d*-spacing) on account of the lattice contraction induced by potassium substitution. The θ–2θ XRD pattern from a (00*l*) preferentially oriented BBO/BBOK/BBO film on MgO (100) is shown in Fig. 2. The (00*l*) peaks are labeled and the substrate peaks are indicated by an asterisk. In the lower pane, the pattern is plotted on a linear scale, and only high intensity (00*l*)-type peaks are observed. In the upper pane, the same pattern is plotted on a log scale, and many additional polycrystalline peaks can be observed, including the most intense powder peak near 29° 2θ. However, the intensities of the (00*l*) peaks are greatly enhanced relative to their statistical distributions, and the (00*l*) peaks exhibit 2-4 orders of magnitude higher intensity than the polycrystalline peaks, indicating strong [100]-directed growth. This film was prepared by first depositing a thin (~10 nm), undoped BBO template layer at 550 °C on the MgO (100) surface. Due to the high temperature growth, this layer should be strongly crystalline or even preferentially oriented, providing an oriented growth template and near perfect lattice match for the K-doped middle layer (~400 nm), which was deposited from the $x = 0.4$ target at lower

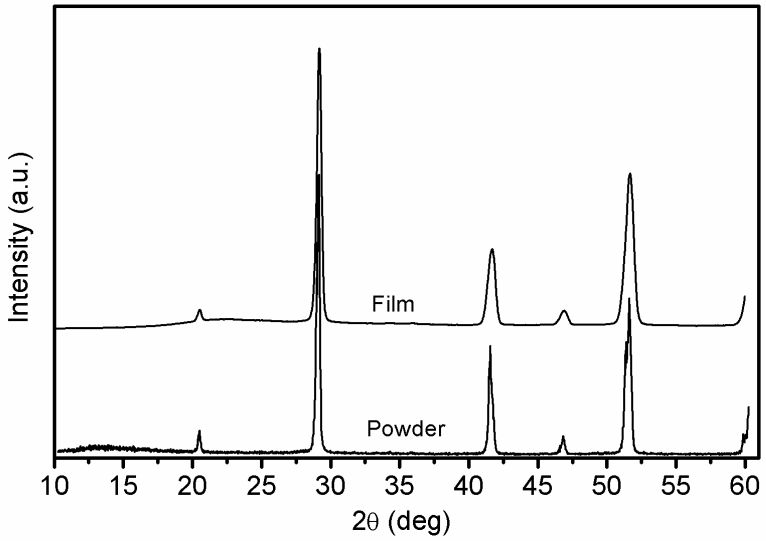

Fig. 1 Thin film and powder diffraction patterns of $BaBiO_3$ showing polycrystalline orientation.

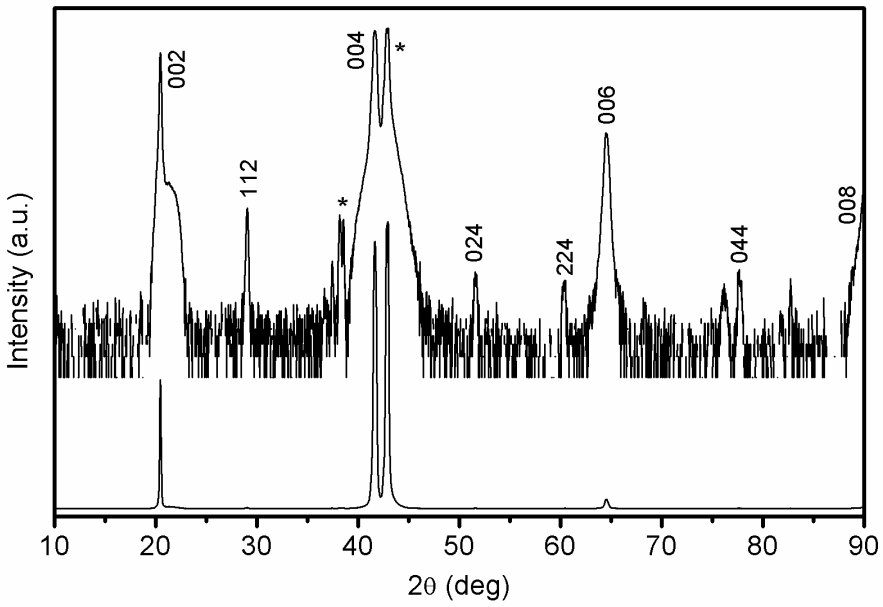

Fig. 2 θ–2θ XRD pattern from a (00*l*) preferentially oriented BKBO film on MgO plotted on log (upper pane) and linear scales (lower pane). The peaks are labeled and substrate reflections are indicated by an asterisk.

temperature (350 °C) to prevent excessive volatilization of K at high substrate temperatures. Finally, a thin layer of undoped BBO (~5 nm) was deposited to passify the hydroscopic K-doped middle layer. The formation of an oriented, undoped template layer has been known to improve the overall quality of BKBO films (11).

Optical Properties

When viewed in reflection, as-deposited crystalline films of BBO appear brown and shiny. However, when viewed in transmission the color of the films is violet-blue. This interesting feature is manifested in the UV–vis transmission spectrum of BKBO film ($x = 0.06$) on a-SiO_2 as a broad 5-20% transmission hump located at 415-425 nm (Fig. 3). The origin of this feature is most likely related to intervalent charge transfer between Bi^{3+} and Bi^{5+} (12). K doping attenuates this effect, and the transmission hump intensity is decreased by an order of magnitude for a film with $x \sim 0.17$. The reflectance (R) of the film over the UV–vis averages 19%, while no transmission (T) of light over this region (aside from the feature near 430 nm) can be measured until $\lambda \sim 650$ nm (=1.91 eV), at which point a broad onset of transmission begins. The weak onset makes assignment of the band gap energy difficult, but literature values suggest about 2 eV, in reasonable agreement with the observed transmission onset in the films (13).

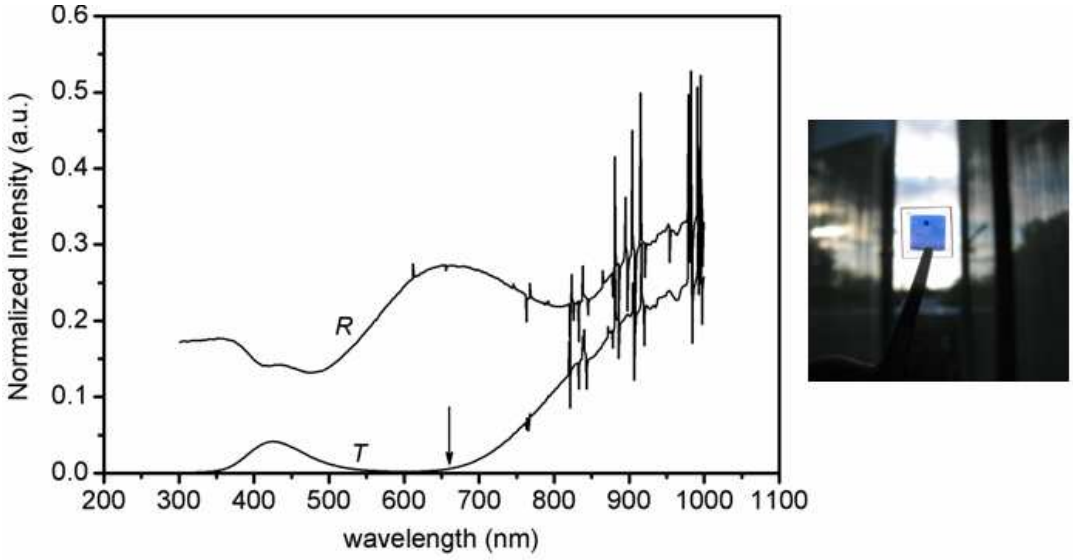

Fig. 3 The UV–visible transmission (lower pane) and reflection (upper pane) from a BKBO film with $x_{film} \sim 0.06$. The films appear brown when viewed in reflection and violet blue when viewed in transmission. The feature near 430 nm in the transmission scan is ascribed to intervalent charge transfer between Bi^{3+} and Bi^{5+} and gives the films their blue appearance. The sharp lines at high wavelength are atomic Xe peaks.

Electronic Properties

The majority carrier type in BBO at room temperature was determined to be positive holes by thermovoltage measurements of a sintered BBO pellet with PLD Ag contacts in which an increasingly positive thermovoltage is measured as the thermal gradient across the sample increases (Fig. 4). The Seebeck coefficient extracted from the linear fit to the data is 475 μV/K. In all cases, undoped pellets showed room temperature conductivity with a simple ohmmeter test, while the undoped films were insulating. This could be due to variable oxygen content in the films or a microcracked film surface. Films could be made conducting only with significant K incorporation, and a film with $x \sim 0.17$ showed a resistivity of 15 Ohm cm. Hall effect measurements on this sample were inconclusive, exhibiting mixed carrier sign. For this film, Ohmic contacts were prepared using colloidal Au with gentle heating in air (60 °C, 10 min). For the bulk phase, the room temperature resistivity measured from a sintered BBO pellet is 2.2 kOhm cm, in good agreement with the literature value of 2 kOhm cm (14). In general, ohmic IV curves to BBO or BKBO films or pellets could not be obtained unless laser deposited Ag or colloidal Au was used, as both colloidal Ag and soldered or pressed In metal failed to give linear IV curves. This is shown in Fig. 4 by the IV curves of a BBO pellet with various contacting schemes.

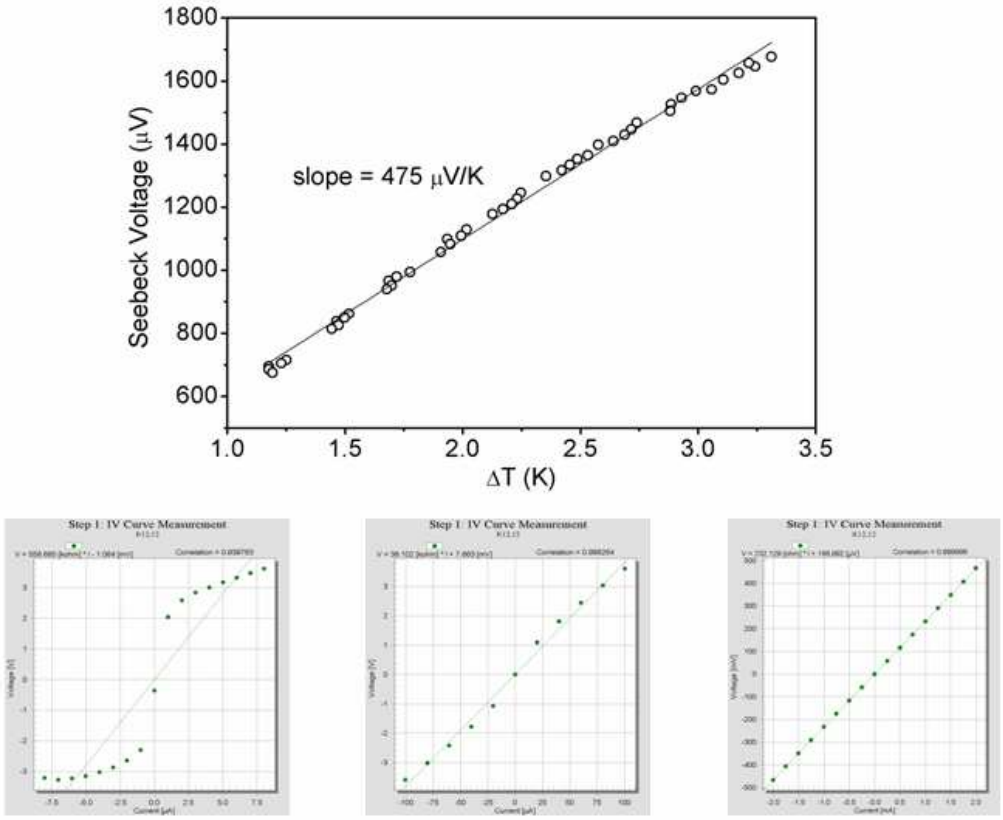

Fig. 4 (Top) The room temperature Seebeck coefficient measured from a sintered BBO pellet with laser deposited Ag contacts. Below, IV curves from a BBO pellet are plotted. From left to right, the IV curves obtained using stainless steel tension contacts, colloidal Ag contacts, and laser ablated Ag contacts.

Film Composition

Quantitative measurement of the elemental composition of undoped and K-doped BBO films were performed using EPMA. The results are summarized in Table 1. Films prepared from (pre-sintered) $x = 0.1$ and $x = 0.4$ targets exhibit significantly less K than the target, with x_{film} values just over half ($x_{film} = 0.06$-0.07) of the pre-sintered value for $x = 0.1$ and well under half ($x_{film} = 0.17$) for 40%. This indicates that the sintered targets contain far less K than expected (as discussed in the experimental section), or that K is lost during film deposition, with both processes being likely. However, the sintered pellet K concentration is unknown, so it is difficult to determine when the K loss is occurring. The K loss is also reflected in the (Ba+K/Bi) cation ratio, with all value less than then theoretical value of 1. We note also that substrate heating can exacerbate the K loss, with greater K loss from films deposited at higher temperature. The problem of K volatilization has been observed and is ameliorated by overdoping of K by as much as 100%. Films deposited onto Si wafers with only a native oxide layer allow quantitative determination of the film oxygen content, while bulk oxide substrates like SiO_2 and MgO make film oxygen quantification less reliable. For sample 14 the cation:anion ratio is very close to the theoretical value of 0.66, indicating that this sample is just slightly oxygen deficient (or cation rich, but this scenario is unlikely). Also, this sample exhibits a cation ratio (Ba+K/Bi) closest to theory.

Table 1 Film composition data obtained from several $Ba_{1-x}K_xBiO_3$ films using EPMA. For K-doped films, the pre-sintered x_{target} and the measured x_{film} are notably different, suggesting that K is volatized in the laser plume or the target sintering. Both processes are likely. Samples 13 and 14 show total cation:anion ratios closest to the theoretical value of 0.66.

sample no.	x_{target} (pre-sinter)	x_{film}	(Ba+K)/Bi	(Ba+K+Bi)/O	substrate
7	0	--	0.947	0.832	a-SiO_2
9	0.1	0.06	0.871	1.524	a-SiO_2
10	0.1	0.07	0.891	0.739	a-SiO_2
11	0.4	0.17	0.940	0.749	MgO
13	0.1	0.06	0.962	0.700	Si
14	0	--	0.982	0.679	Si

Film Morphology

Occasionally, BBO films deposited on a-SiO_2 and MgO exhibit severe microcracking of the film surface. An image of this phenomenon is shown in Fig. 5, an optical micrograph of a BBO film on MgO. According to (15), this effect is attributed to variable oxygen content of the films. That is, following the deposition of a nominally oxygen deficient film at a given temperature in oxygen ambient, the film will take up oxygen on cooling from the growth temperature and cause shrinkage of the lattice and induce cracking. Hence, during growth, film oxygen deficiency should be minimized to avoid surface microcracking. Lower temperature growth should favor reduced oxygen deficiency of the films but will decrease the crystal orientation of the films. An alternative approach is to grow a thin, oriented nucleation layer at high temperature, then reduce the temperature for growth of the main film layer, as discussed in the experimental section. This method will allow for the growth of oxygenated films at lower temperature.

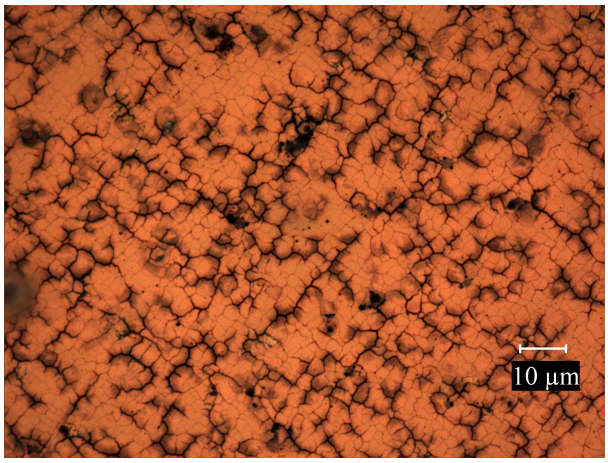

Fig. 5 Optical micrograph of a BBO film surface on an MgO substrate exhibiting severe microcracking.

Conclusion

In summary, we have prepared polycrystalline and preferentially oriented films of $Ba_{1-x}K_xBiO_3$ on vitreous SiO_2 and MgO (100) substrates. The undoped films and BKBO films (x = 0.05-0.07) are electronically insulating while an oriented film with $x \sim 0.17$ on MgO showed 15 Ohm cm. The resistivity of a sintered BBO pellet is 2.2 kOhm cm, in agreement with literature values (14). The room temperature Seebeck coefficient was determined to be 475 μV/K. Quantitative elemental analysis of the films reveals that BKBO films are K-deficient by as much as half of the target nominal K concentration. Severe overdoping of K is needed to solve this problem. BBO films are strongly absorbing in the UV-visible range and show peaks attributed to $Bi^{3+} \leftrightarrow Bi^{5+}$ charge transfer. The band gap energy of BBO (~2 eV) is too low for transparent applications, but the VB electronic structure may provide a high mobility hole transport path as a starting point for band gap engineering.

Acknowledgments

We thank Dr. Hiroshi Mizoguchi and Professor A. Sleight for helpful discussions. This research is based on work supported by the National Science Foundation under Grant No. 0245386 and by the Army Research Office under MURI E-18-667-G3.

References

(1) Sleight, A. W.; Gillson, J. L.; Bierstedt, P. E. *Solid State Commun.* **1975**, *17*, 27.

(2) Cava, R. J.; Batlogg, B.; Krajewski, J. J.; Farrow, R.; Rupp, L. W.; White, A. E.; Short, K.; Peck, W. F.; Kometani, T. *Nature*. **1988**, *332*, 814.

(3) Tang, J.; Zou, Z.; Ye, J. *Angew. Chem. Int. Ed*. **2004**, *43*, 4463.

(4) Lakshminarasimhan, N.; Park, Y.; Choi, W. *Chem. Phys. Lett*. **2008**, *452*, 264.

(5) Cox, D. E.; Sleight, A. W. *Acta Crystallogr. B*. **1979**, *35*, 1.

(6) Mattheiss, L. F.; Hamann, D. R. *Phys. Rev. B*. **1983**, *28*, 4227.

(7) Cox, D. E.; Sleight, A. W. *Solid State Commun.* **1976**, *19*, 969.

(8) Kawazoe, H.; Yanagi, H.; Ueda, K.; Hosono, H. *Mat. Res. Soc. Bull.* **2000**, *25*, 28.

(9) Franchini, C.; Sanna, A.; Marsman, M.; Kresse, G. *Cond. Mat.* **2008**. arXiv:0803.0619v1.

(10) Hui, Z.; Michele, P. *J. Mater. Chem.* **2002**, *12*, 3787.

(11) Norton, D. P.; Budai, J. D.; Chakoumakos, B. C.; Feenstra, R. *Appl. Phys. Lett.* **1993**, *62*, 414.

(12) Mizoguchi, H.; Kawazoe, H.; Hosono, H.; Fujitsu, S. *Solid State Commun.* **1997**, *104*, 705.

(13) Tajima, S.; Uchida, S.; Masaki, A.; Takagi, H.; Kitazawa, K.; Tanaka, S.; Sugai, S. *Phys. Rev. B*. **1987**, *35*, 696.

(14) Drost, R. J.; Fu, W. T. *Mat. Res. Bull*. **1995**, *30*, 471.

(15) Hellman, E. S.; Hartford, E. H.; Gyorgy, E. M. *Appl. Phys. Lett.* **1991**, *58*, 1335.

CHAPTER 7

Conclusion

In summary, we have presented here our results of thin film growth and characterization of several wide–gap chalcogenide and oxide materials which may be applied in transparent electronics. The method of pulsed laser deposition was described in terms of its key advantages and disadvantages, among which are the faithful reproduction of the target cation stoichiometry in the film under most conditions, highly energetic ablated species, and experimental simplicity and flexibility. The most significant limitations of PLD include the generation of micron-sized particles from the target and the difficulty in preparing uniformly thick coatings over large area. All the samples investigated in this research were prepared by PLD.

In chapter 3 we presented our findings on W-doped In_2O_3 and the remarkable result of a 3.2-fold increase in the electron mobility compared to In_2O_3:Sn. In particular, we have prepared IWO thin films which exhibit $\mu = 112$ cm^2/Vs, $n = 1.67 \times 10^{20}$ cm^{-3}, and $\rho = 3.37 \times 10^{-4}$ Ohm cm at room temperature on an amorphous substrate. Also, we have summarized the unexpected mechanism of transition metal magnetic exchange interactions which account for the anomalously high mobility measured from W, Mo, and Zr-doped In_2O_3. In particular, the exchange interactions impart spin distinguishability to the $[W_{In}^{\bullet\bullet\bullet} O_i'']^{\bullet}$ charge generating defects, such that free carriers now only “see” (that is, scatter from) a defect of the same spin. The result of this is an effective two-fold reduction in the number of scattering centers. Future work on this system may include investigations on the upper limit of the mobility in these compounds. Also, the conductivity of In_2O_3:Sn remains significantly higher than In_2O_3:W due a larger carrier density. Future research may be undertaken to increase the carrier density of IWO while maintaining the high mobility of carriers.

In chapter 4 we presented out results on the oxychalcogenide BiCuOSe. In particular, we have demonstrated facile, high quality thin film preparations on a-SiO_2 and single crystalline MgO and $SrTiO_3$ substrates. BiCuOSe is a black p-type semiconductor which exhibits high hole mobility of 4 cm^2/Vs and a conductivity of up to 176 S/cm when Ca is substituted for Bi. Electronic structure calculations reveal that the disparate electronic configurations of the Bi^{3+} and La^{3+} ions account for the distinct chemical and physical differences of BiCuOSe (low band gap, low temperature *in-situ* preparation) and LaCuOSe (high band gap, high temperature *ex-situ* preparation).

In chapter 5 we presented novel research on thin films of two members of the sulvanite class of materials, wide–gap Cu_3TaCh_4 (Ch = S, Se). Using a two-step growth method consisting of PLD and *ex-situ* chalcogenide vapor annealing (CVA) we have prepared (100)-aligned films on both amorphous and crystalline substrates. The band gap energies were measured to be 2.72 eV for the sulfide and 2.35 eV for the selenide. The materials are p-type, and an oriented CTS film revealed a mobility of 0.8 cm^2/Vs, $p = 2.86 \times 10^{20}$ cm^{-3}, and ρ = 27 mOhm cm (=37 S/cm). Also, we described a simple method to prepare thin film solid solutions of $Cu_3Ta(ChCh')_4$. Future work on this system should include the fabrication of very high quality, highly dense ablation targets. This would improve film morphology greatly and perhaps make *in-situ* growth possible. Also, cation and anion doping by CVA should be explored more fully in conjunction with EPMA.

Chapter 6 described the preparation of the charge-ordered compound $BaBiO_3$ (BBO). This material undergoes charge disproportionaton of Bi via $2Bi^{4+} \rightarrow Bi^{3+} + Bi^{5+}$ and an energy gap is opened up between the filled Bi^{3+} valence band and the empty Bi^{5+}

conduction band. The $6s^2$ valence band configuration should provide a high mobility hole transport path, and band gap engineering with Ce alloying widens the 2 eV optical gap making this material a possible parent compound for a p-type transparent conductor. However, undoped thin films of BBO are electrically insulating, and only high levels of K doping would impart conductivity in the films. Additionally, significant loss of K during the deposition and/or the target sintering represent non-trivial challenges to overcome.

(1) Arribart, H.; Sapoval, B.; Gorochov, O.; LeNagard, N. *Solid State Commun*. **1978**, *26*, 435.

(2) Burstein, E. *Phys. Rev*. **1953**, *93*, 632.

(3) Cava, R. J.; Batlogg, B.; Krajewski, J. J.; Farrow, R.; Rupp, L. W.; White, A. E.; Short, K.; Peck, W. F.; Kometani, T. *Nature*. **1988**, *332*, 814.

(4) Chrisey, D. B.; Hubler, G. K. *Pulsed Laser Deposition of Thin Films*; 1st ed.; Wiley-Interscience, 1994.

(5) Clevenger, L. A.; Bojarczuk, N. A.; Holloway, K.; Harper, J. M. E.; Cabral, J.; Schad, R. G.; Cardone, F.; Stolt, L. *J. Appl. Phys*. **1993**, *73*, 300.

(6) Coutts, T. J.; Young, D. L.; Li, X. *Mat. Res. Soc. Bull*. **2000**, *25*, 58.

(7) Cox, D. E.; Sleight, A. W. *Acta Crystallogr. B*. **1979**, *35*, 1.

(8) Cox, D. E.; Sleight, A. W. *Solid State Commun*. **1976**, *19*, 969.

(9) Crottaz, O.; Kubel, F.; Schmid, H. *J. Sol. State. Chem*. **1996**, *122*, 247.

(10) Cullity, B.; Stock, S. *Elements of X-Ray Diffraction*; 3rd ed.; Prentice Hall, 2001.

(11) Delgado, G. E.; Mora, A. J.; Duran, S.; Munoz, M.; Grima-Gallardo, P. *J. Alloys Compd*. **2007**, *439*, 346-349.

(12) Denton, A. R.; Ashcroft, N. W. *Phys. Rev. A*. **1991**, *43*, 3161.

(13) Dimroth, F.; Kurtz, S. *Mat. Res. Soc. Bull*. **2007**, 32.

(14) Drost, R. J.; Fu, W. T. *Mat. Res. Bull*. **1995**, *30*, 471.

(15) Eason, R. *Pulsed Laser Deposition of Thin Films: Applications-Led Growth of Functional Materials*; Wiley-Interscience, 2006.

(16) Franchini, C.; Sanna, A.; Marsman, M.; Kresse, G. *Cond. Mat*. **2008**. arXiv:0803.0619v1.

(17) Garcia, W.; Aramburo, A.; Guillen, *J. Revista Colombiana de Fsica*. **2008**, *40*, 36.

(18) Garrelie, F.; Loir, A. S.; Donnet, C.; Rogemond, F.; Le Harzic, R.; Belin, M.; Audouard, E.; Laporte, P. *Surf. Coat. Technol*. **2003**, *163-164*, 306.

(19) Greer, J. A.; Tabat, M. D. *J. Vac. Sci. Technol. A*. **1995**, *13*, 1175.

(20) Hahn, H.; Lorent, C. D. *Z. Anorg. Allg. Chem*. **1955**, *279*, 281.

(21) Hamberg, I.; Granqvist, C. G. *J. Appl. Phys*. **1986**, *60*, R123.

(22) Hellman, E. S.; Hartford, E. H.; Gyorgy, E. M. *Appl. Phys. Lett*. **1991**, *58*, 1335.

(23) Hersh, P. A. *Ph. D. dissertation*, Oregon State University, 2007.

(24) Hiramatsu, H.; Ohta, H.; Suzuki, T.; Honjo, C.; Ikuhara, Y.; Ueda, K.; Kamiya, T.; Hirano, M.; Hosono, H. *Cryst. Growth Des*. **2004**, *4*, 301.

(25) Hiramatsu, H.; Ueda, K.; Ohta, H.; Hirano, M.; Kamiya, T.; Hosono, H. *Thin Solid Films*. **2003**, *445*, 304.

(26) Hiramatsu, H.; Ueda, K.; Ohta, H.; Hirano, M.; Kikuchi, M.; Yanagi, H.; Kamiya, T.; Hosono, H. *Appl. Phys. Lett*. **2007**, *91*, 012104.

(27) Hiramatsu, H.; Ueda, K.; Takafuji, K.; Ohta, H.; Hirano, M.; Kamiya, T.; Hosono, H. *J. Appl. Phys*. **2003**, *94*, 5805.

(28) Hiramatsu, H.; Yanagi, H.; Kamiya, T.; Ueda, K.; Hirano, M.; Hosono, H. *Chem. Mater*. **2008**, *20*, 326-334.

(29) Hosono, H.; Ohta, H.; Hayashi, K.; Orita, M.; Hirano, M. *J. Cryst. Growth*. **2002**, *237-239*, 496.

(30) Hui, Z.; Michele, P. *J. Mater. Chem*. **2002**, *12*, 3787.

(31) Hulliger, V. F. *Hel. Phys. Acta*. **1961**, *34*, 379.

(32) Kamihara, Y.; Watanabe, T.; Hirano, M.; Hosono, H. *J. Am. Chem. Soc*. **2008**, *130*, 3296.

(33) Kawazoe, H.; Yanagi, H.; Ueda, K.; Hosono, H. *Mat. Res. Soc. Bull*. **2000**, *25*, 28-36.

(34) Kawazoe, H.; Yasukawa, M.; Hyodo, H.; Kurita, M.; Yanagi, H.; Hosono, H. *Nature*. **1997**, *389*, 939.

(35) Kohama, Y.; Kamihara, Y.; Hirano, M.; Kawaji, H.; Atake, T.; Hosono, H. *Phys. Rev. B*. **2008**, *78*, 020512.

(36) Kohler, B. U.; Jansen, M. *Z. Anorg. Allg. Chem*. **1986**, *543*, 73.

(37) Koida, T.; Kondo, M. *Appl. Phys. Lett*. **2006**, *89*, 082104.

(38) Kykyneshi, R.; McIntyre, D.; Tate, J.; Park, C.; Keszler, D. *Solid State Sci*. **2008**, *10*, 921.

(39) Lakshminarasimhan, N.; Park, Y.; Choi, W. *Chem. Phys. Lett*. **2008**, *452*, 264.

(40) Laurila, T.; Zeng, K.; Kivilahti, J. K.; Molarius, J.; Suni, I. *J. Appl. Phys*. **2000**, *88*, 3377.

(41) Laux, S.; Kaiser, N.; Zoller, A.; Gutzelmann, R.; Lauth, H.; Bernitzki, H. *Thin Solid Films*. **1998**, *335*, 1.

(42) Li, J.; Guo, H.; Proserpio, D. M.; Sironi, A. *J. Sol. State. Chem*. **1995**, *117*, 247.

(43) Li, Y.; Yao, X.; Tanabe, K. *Physica C*. **1998**, *304*, 239.

(44) Maruyama, T.; Tago, T. *Appl. Phys. Lett*. **1994**, *64*, 1395.

(45) Mattheiss, L. F.; Hamann, D. R. *Phys. Rev. B*. **1983**, *28*, 4227.

(46) Medvedeva, *J. Appl. Phys. A*. **2007**, *89*, 43.

(47) Medvedeva, J. E. *Phys. Rev. Lett*. **2006**, *97*, 086401.

(48) Meng, Y.; Yang, X.; Chen, H.; Shen, J.; Jiang, Y.; Zhang, Z.; Hua, Z. *Thin Solid Films*. **2001**, *394*, 218.

(49) Minami, T. *Thin Solid Films*. **2008**, *516*, 5822.

(50) Mizoguchi, H.; Kawazoe, H.; Hosono, H.; Fujitsu, *S. Solid State Commun*. **1997**, *104*, 705.

(51) Moss, T. S. *Proc. Phys. Soc. London*. **1954**, *B67*, 775.

(52) Moulder, J. F.; Stickle, W. F.; Sobol, P. E.; Bomben, K. D. *Handbook of X Ray Photoelectron Spectroscopy: A Reference Book of Standard Spectra for Identification and Interpretation of XPS Data*; Reissue.; Physical Electronics, 1995.

(53) Newhouse, P. F.; Park, C-H.; Keszler, D. A.; Tate, J.; Nyholm, P. S. *Mat. Res. Soc. Symp. Proc*. **2006**, *905E*, 0905-DD01-02.1.

(54) Newhouse, P. F.; Hersh, P. A.; Zakutayev, A.; Platt, H. A. S.; Richard, A.; Keszler, D. A.; Tate, J. *Accepted to Thin Solid Films*.

(55) Newhouse, P. F.; Park, C.; Keszler, D. A.; Tate, J.; Nyholm, P. S. *Appl. Phys. Lett*. **2005**, *87*, 112108.

(56) Norton, D. P.; Budai, J. D.; Chakoumakos, B. C.; Feenstra, R. *Appl. Phys. Lett*. **1993**, *62*, 414.

(57) Norton, D. P.; Park, C.; Budai, J. D.; Pennycook, S. J.; Prouteau, C. *Appl. Phys. Lett*. **1999**, *74*, 2134.

(58) Ohta, H.; Orita, M.; Hirano, M.; Hosono, H. *J. Appl. Phys*. **2002**, *91*, 3547.

(59) Ohta, H.; Orita, M.; Hirano, M.; Tanji, H.; Kawazoe, H.; Hosono, H. *Appl. Phys. Lett*. **2000**, *76*, 2740.

(60) Ohtani, T.; Tachibana, Y.; Fujii, Y. *J. Alloys Compd*. **1997**, *262-263*, 175.

(61) Palazzi, M. *Acad. Sci. Paris*. **1981**, *292*, 789.

(62) Park, C.; Keszler, D. A.; Yanagi, H.; Tate, J. *Thin Solid Films*. **2003**, *445*, 288.

(63) Park, C.; Kykyneshi, R.; Yokochi, A.; Tate, J.; Keszler, D. A. *J. Solid State Chem*. **2007**, *180*, 1672.

(64) Pauling, L.; Hultgren, R. *Z. Kristallogr. A*. **1933**, *84*, 204.

(65) Pechen, E. V.; Varlashkin, A. V.; Krasnosvobodtsev, S. I.; Brunner, B.; Renk, K. F. *Appl. Phys. Lett*. **1995**, *66*, 2292.

(66) Reilly, A.; Allmond, C.; Watson, S.; Gammon, J.; Kim, J. G. *J. Appl. Phys*. **2003**, *93*, 3098.

(67) Sleight, A. W.; Gillson, J. L.; Bierstedt, P. E. *Solid State Commun*. **1975**, *17*, 27.

(68) Tahar, R. B. H.; Ban, T.; Ohya, Y.; Takahashi, Y. *J. Appl. Phys*. **1998**, *83*, 2631.

(69) Tajima, S.; Uchida, S.; Masaki, A.; Takagi, H.; Kitazawa, K.; Tanaka, S.; Sugai, S. *Phys. Rev. B*. **1987**, *35*, 696.

(70) Tang, J.; Zou, Z.; Ye, *J. Angew. Chem. Int. Ed*. **2004**, *43*, 4463.

(71) Tate, J. *unpublished*.

(72) Trojer, F. *Am. Mineral*. **1966**, *51*, 890.

(73) Ueda, K.; Hiramatsu, H.; Ohta, H.; Hirano, M.; Kamiya, T.; Hosono, H. *Phys. Rev. B*. **2004**, *69*, 155305.

(74) Ueda, K.; Hosono, H. *Thin Solid Films*. **2002**, *411*, 115.

(75) Ueda, K.; Inoue, S.; Hosono, H.; Sarukura, N.; Hirano, M. *Appl. Phys. Lett*. **2001**, *78*, 2333.

(76) van Hest, M. F. A. M.; Dabney, M. S.; Perkins, J. D.; Ginley, D. S.; Taylor, M. P. *Appl. Phys. Lett*. **2005**, *87*, 032111.

(77) Walsh, A.; Da Silva, J. L. F.; Wei, S. *Phys. Rev. B*. **2008**, *78*, 075211.

(78) Warmsingh, C.; Yoshida, Y.; Readey, D. W.; Teplin, C. W.; Perkins, J. D.; Parilla, P. A.; Gedvilas, L. M.; Keyes, B. M.; Ginley, D. S. *J. Appl. Phys*. **2004**, *95*, 3831.

(79) Watanabe, T.; Yanagi, H.; Kamiya, T.; Kamihara, Y.; Hiramatsu, H.; Hirano, M.; Hosono, H. *Inorg. Chem*. **2007**, *46*, 7719.

(80) Wong, H. Y.; Ong, C. W.; Kwok, R. W. M.; Wong, K. W.; Wong, S. P.; Cheung, W. Y. *Thin Solid Films*. **2000**, *376*, 131.

(81) Yanagi, H.; Kawamura, R.; Kamiya, T.; Kamihara, Y.; Hirano, M.; Nakamura, T.; Osawa, H.; Hosono, H. *Phys. Rev. B*. **2008**, *77*, 224431.

(82) Yanagi, H.; Tate, J.; Park, S.; Park, C.; Keszler, D. A. *Appl. Phys. Lett*. **2003**, *82*, 2814.

(83) Yoshida, Y.; Wood, D. M.; Gessert, T. A.; Coutts, T. *J. Appl. Phys. Lett*. **2004**, *84*, 2097.

(84) Zakutayev, A.; Platt, H. A. S. *unpublished*.

(85) Zhang, Y.; Russo, R. E.; Mao, S. S. *Appl. Phys. Lett*. **2005**, *87*, 133115.

(86) Zhu, W.; Huang, Y.; Wu, F.; Dong, C.; Chen, H.; Zhao, Z. *J. Solid State Chem*. **1994**, *29*, 505.

Appendices

Appendix A

Design, Integration and Development of OSU Pulsed Laser Deposition Facilities.

P. F. Newhouse[a], Hiroshi Yanagi[b], T. Hinke[a,b] and J. Tate[a,b]

[a]Department of Chemistry, Oregon State University, 153 Gilbert Hall, Corvallis, Oregon USA 97331-4003

[b]Department of Physics, Oregon State University, 301 Weniger Hall, Corvallis, Oregon USA 97331-6507

Introduction

The purpose of this appendix is to describe the OSU PLD facilities and our role in their design, implementation, and development. In particular we show the results of hardware development and post-installation improvements necessary for film deposition and system reliability. The OSU PLD systems consist of a single UV laser and two independent vacuum chambers—a custom built chamber from Thermionics ("Tli"), and a much smaller "turn-key" chamber by Neocera. For the Tli chamber we describe the purpose of the major ports in addition to descriptions of pressure gauging, substrate heating, and others. A similar treatment of the Neocera system is presented. Also we show many images of the system components such as shadow masks, target holders, beam apertures, etc. designed and fabricated to improve system performance.

PLD at Oregon State University

The OSU PLD facility consists of a Lambda Physik Compex 201 KrF excimer laser (λ = 248 nm, τ = 25 ns) coupled to two independent vacuum chambers—a large volume, load-locked (LL), fully custom system built by Thermionics laboratory Inc., and a much smaller, "turn-key" system built by Neocera (Fig. 1). The laser output is directed into a given chamber using two sets of mirrors and lenses, all of which are high grade UV silica. The middle mirror is mounted on an (x,y) micrometer stage to either move the mirror into the beam path for the Neocera chamber, or remove it from the beam path for direction into the Tli chamber (Fig. 1). The key differences in the

Fig. 1 The Tate Lab PLD facility at OSU. Pulsed radiation from a KrF excimer laser is directed into one of two chambers using a moveable mirror in the middle of the optical tower. External lenses focus the laser output through a UV-grade flange on the chamber body and onto a target inside the chamber.

two PLD chambers are their respective base pressures (1×10^{-7} torr Neocera vs. 1×10^{-9} torr Tli), materials usage (chalcogenide materials in Tli. vs. oxides and nitrides in Neocera), and systems control (Tli. is fully manual, while Neocera includes software integration). In this section, we describe each system in detail with attention to the primary components like substrate and target manipulators, pumping and gauging systems, and gas systems. We also show images and descriptions of various custom designed and fabricated hardware including shadow masks, target holders, beam apertures, etc. developed to improve system functionality.

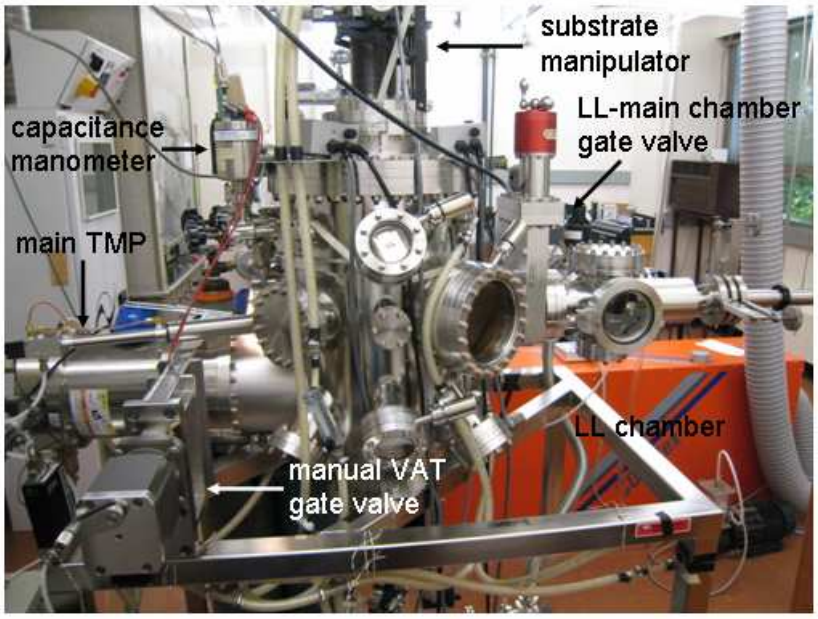

Fig. 2 Backside view of the Thermionics PLD system. Key components are labeled. The white tubing circulates cooling water from a closed cycle chiller to the main chamber body, target and substrate manipulators, and the main TMP.

Thermionics PLD System

An image of the Tli system is shown in Fig. 2. The system consists of two gate-valve coupled chambers, the smaller of the two on the right in Fig. 2 is the sample load lock chamber. Each chamber is pumped individually by TMPs backed by rotary vane mechanical pumps. In the event of a power outage, mechanical pump-to-TMP isolation valves close, safeguarding the chambers from atmosphere and oil backstreaming. The LL chamber is designed to transfer films in an out of the main chamber under vacuum using a magnetic rotary feedthrough. Only one substrate and one target may be transferred at a time. The main chamber volume is drastically

larger. During maintenance, the main chamber is vented through the LL chamber. The targets are transferred to a 6-target carousel holder, which has a manual stepper drive to move any single target into the path of the laser beam. Note that since this system is fully manual, controlled switching of the targets is not possible, making multilayer film preparation difficult. The target holder has Z-positional movement over ~10 in. The substrate holder has (*x*,*y*,*z*) displacement capability, with high resolution a (*x*,*y*) micrometer and lower resolution *z*-positioning. The *z*-positional movement is ~ 6in.

Chamber Body and Ports

The body of the chamber consists of ports ranging form 1" to 10" in diameter, some of which are unused at present. The primary ports include

- 10″ main TMP coupled to a manual VAT gate valve
- Vacuum gauging (nude ion, dual capacitance manometer)
- Dual 4.5″ laser entrance and laser energy measurement ports.
- 8″ target manipulator (TM)
- Deposition viewports with shutters (8″, 2.75″, and 4.5″)
- 8″ Substrate manipulator (SM)
- 4.5″ gas admittance port with variable leak valve

The chassis of the chamber body is water cooled. Additional unused ports include orthogonal RHEED gun and screen ports and an *in-situ* substrate laser annealing port, which requires additional external optics to direct the beam toward the substrate.

Target Manipulator (TM)

The TM (Fig. 3) consists of a 6-target carousel with protective covering to shield the other five targets during deposition. The TM has only *z*-displacement capability. The ablated target is rotated during the deposition, but not rastered, thus forming annular features on the target surface. Cone-shaped target holders are designed to fit 1″ x 0.25″ cylindrical targets, but with proper engineering various dimensions can be accommodated. In practice, a target with the stated dimensions requires of order 15 grams of powder, which can be time consuming to prepare. This is especially true for novel materials, which cannot be obtained commercially. Thus the author proposes a using much smaller targets (3/8″ x 1/8″ thick) in a modified target holder. This procedure has been demonstrated (see "Zr-doped CTS" in Chapter 5).

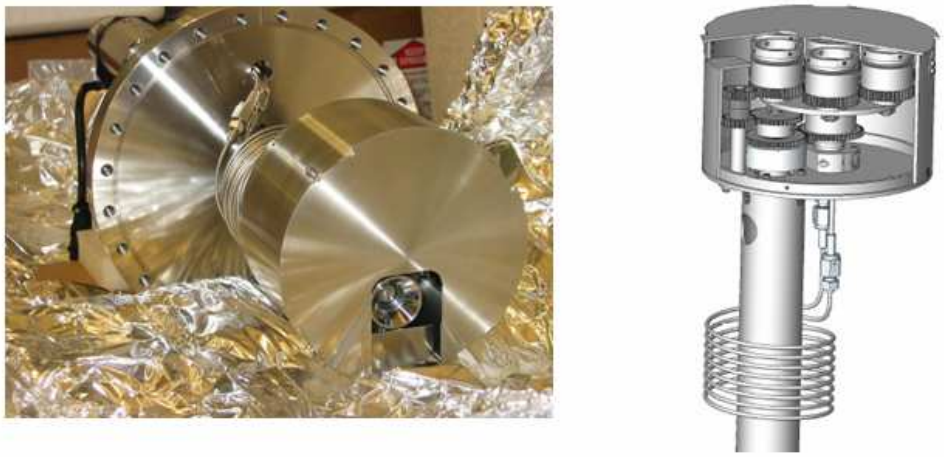

Fig. 3 The Tli target manipulator. The TM houses six targets. A motor drives the gears which rotate (but not raster) the target during the deposition. Target switching is performed manually. Water cooling lines are also shown.

Substrate Manipulator (SM)

The SM houses two 500 W max bulbs which provide radiant substrate heating (Fig. 4). K-type thermcouple, lamp power, water-cooling, and gas feedthroughs are located at the crown. An (*x*,*y*) micrometer stage provides high resolution placement of the substrate above the ablation plume for maximum uniformity or off-axis deposition. This feature allows the user to place the film directly over the plume, thus maximizing thickness uniformity, or placing the sample off-axis for specialty depositions. Z-displacement of the substrate allows for a range of target to substrate distances raging from ~1″ to ~6″. The gas feedthrough is routed down to the substrate, thus forming a shower ring of gas.

Fig. 4 The Tli Substrate manipulator. At left, the substrate holder is affixed to the manipulator, and removed at right, exposing the dual bulbs that provide radiant heating of metal to which the substrate is mounted. The gas shower ring can also be seen.

Pumping System

The pumping system for the main chamber consists of a Seiko1000 L/s (N_2) magnetic levitation TMP (35k rpm normal rotation speed) backed by a BOC Edwards rotary vane pump. The backing pump is lubricated with crytox oil, which permits the use of corrosive deposition gases like H_2S. To date, however, no such gas has been used (only Ar/H_2, Ar, and O_2) have been used. The base pressure of this system is 1×10^{-9} torr. Isolation and vent valves are affixed to the backing pump foreline, as well as an oil mist trap. A manually operated VAT gate valve is used to throttle the TMP when the deposition pressures are high ($>10^{-4}$ torr). For corrosive gas such as O_2, and H_2S, an N_2 mass flow controller (MFC) couples to a purge port on the TMP and provides inert gas purging to protect the TMP from corrosive damage. For oxygen this is not as critical to use.

Gauging

Vacuum gauging is performed using three independent manometers. A nude ion gauge is used to from base pressure to 10^{-5} torr, while a low pressure capacitance manometer (CM) is used in the range from 10^{-5}-10^{-2} torr. Another CM is used at higher pressures (10^{-3}-10^{0} torr). The gauges are affixed to elbowed ports, which preclude film deposition onto the filament or diaphragm. This is particularly important in the case of the CM, where deposition onto the diaphragm is the most common cause of failure or spurious readings. Also, the CM ports include high vacuum valves. The valves are closed before venting the chamber to keep high vacuum on the diaphragms as exposure to atmospheric pressure can offset the zero

calibration. The IG emission current must be turned off when using oxygen gas, which will combust the filament.

Gas System

Deposition background gas is delivered using a variable leak valve coupled to a 4.5″ feedthrough. Gas can be routed in two ways—through a gas shower ring around the substrate, or straight through the feedthrough. The position of a valve dictates which way the gas will be routed. The system features additional pneumatically actuated valves. The first is located on the gas shower ring line. An electronic switch controls the pneumatic actuation of this valve. In the event of a power failure during deposition, the switch opens and the valve closes. This is to prevent unsafe pressure from building up in the system when a power outage trips the pump power circuit.

Neocera System

An image of the Neocera system is shown in Fig. 5. A major difference from the Tli system is that this chamber does not include a LL and thus must be fully vented after each run. As a result this chamber has a much lower working base pressure (1×10^{-7} torr) and is used for the growth of air-insensitive materials like oxides, metals, and nitrides. The system will pump down to 2×10^{-8} torr with the gas manifold fully closed, requiring more than 24 h. No component of this system is water cooled, adding another layer of simplicity. All of the as-installed viton rubber gaskets were replaced with Cu gaskets upon arrival, substantially improving system

base pressure. The system is computer controlled, which permits the fabrication of complex multilayer structures with precise layering and thickness control.

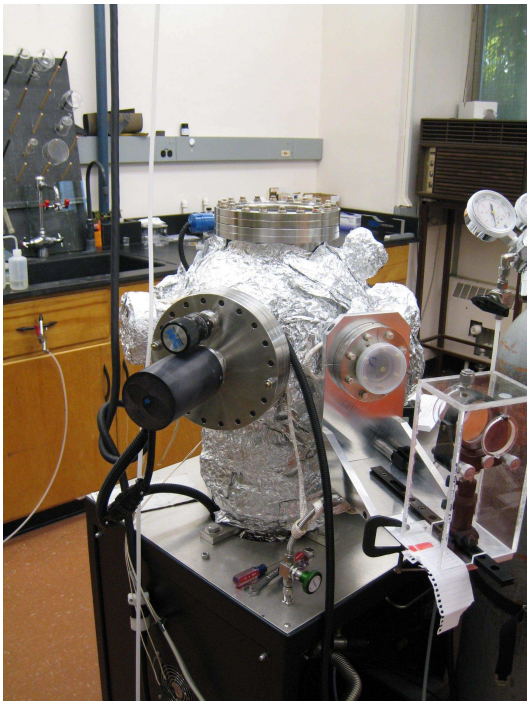

Fig. 5 The Neocera PLD chamber. The substrate manipulator flange is in the foreground. The focusing lens is located in a custom plastic housing.

Neocera Pumping

System vacuum is provided by a Pfiffer TMU 261P 210 l/s (N_2) TMP backed by a Pfiffer MVP 055-3 3.8 m^3/h diaphragm pump. A N_2 purge valve allows short, repeated pump/purge cycles to be performed after each venting, if desired. Thus the system can pump quite quickly.

Substrate Manipulator

The SM consists of a 2″ diameter inconel block with four tapped holes where substrate clips are applied. The substrate is clamped directly to the block and optical interference fringes indicate sufficient thermal contact to the block. The SM has no rotational control, so accurate plume-substrate alignment is important. However, the SM does offer a range of fixed (*x*,*y*,*z*) placements that must be set prior to pump down and cannot be modified during film deposition.

Gauging

In the range of base pressure to 10^{-5} torr, a Pfiffer PKR 251 cold cathode gauge is used. In the higher pressure regime, a convectron gauge is used from 0.1 torr-atmosphere. The convectron gauge is calibrated for N_2, and uses no gas correction factor for air, O_2, or N_2 from 0.1 torr to 760 torr. For Ar, gas correction factors must be used over the entire pressure range.

Target Manipulator

The Neocera TM holds six 1″ targets or three 2″ targets. Motors on the TM allow for computer controlled target rotation and rastering, affording near 100% target surface usage. This perhaps the most significant advantage of this system compared to the Tli system. Rotational velocity and raster speed control are also available. Custom target holders were fabricated to hold the targets, two of which are spring loaded, and the others are C-clamp type (Fig. 6). Thus, an epoxy-based bonding method is avoided, allowing for easy target switch-out. For multilayer growth, simple programs may be written using the software GUI.

Fig. 6 Upper Left: a modified adjustable parallel used to clamp down a square substrate for scoring and cleaving. The wedge can be moved along the edge and serves as a straight edge to score the glass. A few millimeters of vertical clearance was built in so the straight edge never touches the film surface. Also shown in upper left are clips made from 10 gauge wire and spot welded to a 2-34 washer. These are used to clamp down the substrate to the heater block, providing firm pressure. At upper right, a $BaBiO_3$ target clamped to the target holder using a custom designed mini c-clamp allowing for easy target switch-out. A set screw allows a range of target heights to be accommodated. At lower left, several different style shadow masks. In the lower left image, the bottom far left piece is a substrate chuck for a 10 x 15 mm substrate. The chuck includes locating holes for a mask that fits over the substrate, giving perfect alignment. All of the other mask with small locating holes in their corners are used with this chuck. Some of the masks were laser-cut, but the chuck and the cross (upper right) were custom designed and fabricated at OSU.

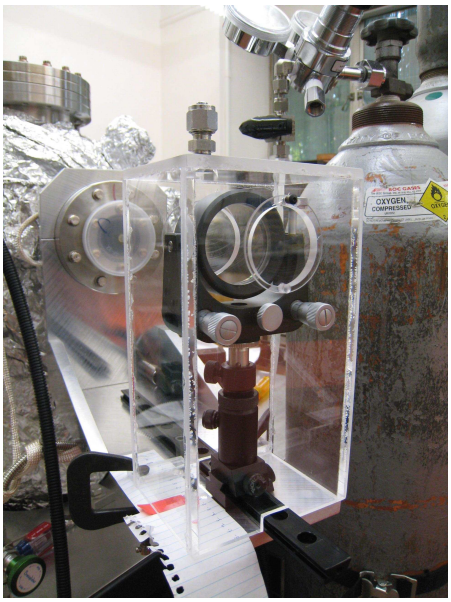

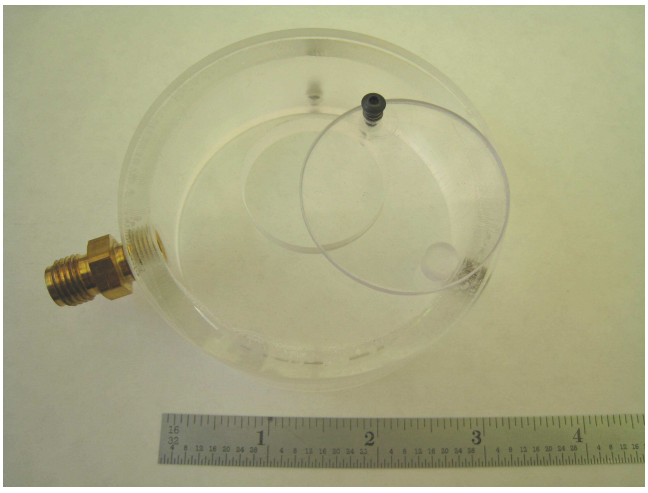

Fig. 7 (Upper image) Custom plexiglass housing for the focusing lens for the Neocera system. The housing prevents dust accumulation and absorbs diffuse UV scattering when the beam is incident on the surfaces. For added safety, this lens has a double side 248 nm antireflection coating. (Below) Custom plastic covering for the entrance port window with inert gas purge.

Fig. 8 (upper L image, from L to R) Deposition sides of masks used to deposit electrical contacts onto films patterned with the hall mask, an arbitrary four-point in-line pattern, and contacts on the surface of a pellet. The holes are countersunk to reduce shadowing. At above right, the reverse side of the masks. The square shaped mask was fabricated with a slight depression on the film side. In this way, the mask only touches the film at the site of the contacts and does not scrape the film center. This is important because film integrity is important for good electrical measurements. The bottom image is a $BaBiO_3$ film with gold PLD contacts deposited with this mask.

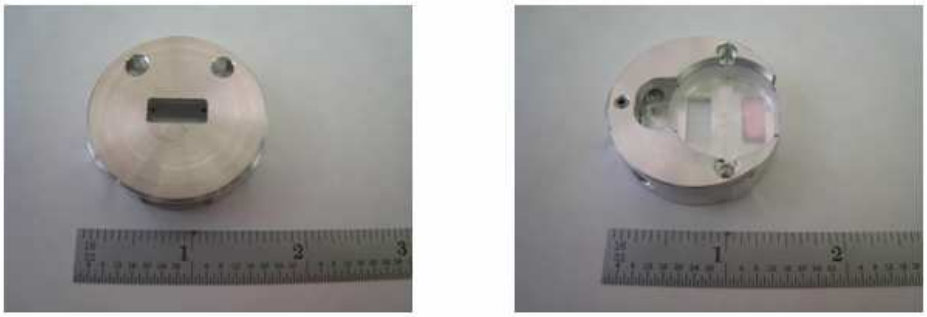

Fig. 9 An assembly used to protect the Neocera laser entrance port from becoming coated from the ablation plume. The assembly is a housing for a one side, 248 nm antireflection (AR) coated sacrificial window. The image at left is the side which faces the ablation plume. The circular holes are blind pumping ports. At right is the laser incident AR coated side. The beam traverses the rectangular cut out on its way to the target. After some time, the sacrifical window will become dirty from the plume and require cleaning (this can be seen in the image). But since we have deposited only on the sacrificial window and not the laser entrance port, all we must do is rotate the window to a new position. Thus the entrance port never "sees" the plume and must never be cleaned. In this way a safer double side AR coated entrance port may be used and will never be scratched from cleaning. The assembly fits inside the laser entrance port. Talk about a slick solution.

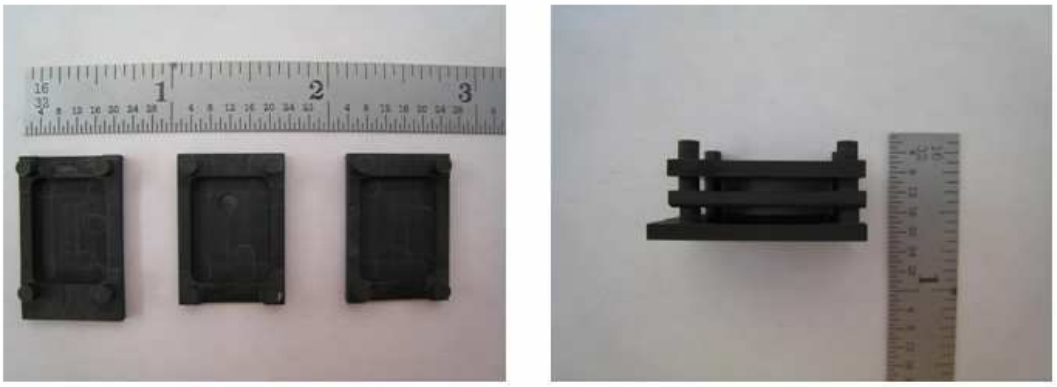

Fig. 10 Custom graphite “bunk bed” crucibles fabricated for annealing Cu-Ta metal layers in a less than 1″ inner diameter tube furnace under flowing H_2S gas. Each “bunk bed” fits several ~ 0.5 cm films. The bunks are then staked on each other with pegs. The furnace used for these anneals has a significant longitudinal temperature gradient, and this method afforded more uniform heating since there is no thermal gradient in the *z*-direction.